Coupling of single proton configurations to collective core excitations in ^{162}Yb: the nucleus ^{161}Tm.

Sandile Jongile

University of Zululand

Thesis presented in fulfillment of the requirements for the degree of Master of Science at the University of Zululand

Supervisor(s) :

Dr S.S. Ntshangase, *University of Zululand*

Co-Supervisor(s) :

Prof J.F. Sharpey-Schafer, *University of the Western Cape*

Dr T.R.S. Dinoko, *iThemba Laboratory for Accelerator-Based Science*

Dr S.N.T.M. Majola, *iThemba Laboratory for Accelerator-Based Science*

April 20, 2017

Declaration

I, the undersigned, hereby declare that the work contained in this thesis is my own original work and that I have not previously in its entirety or in part submitted it at any university for a degree.

....

Signature of the student

Date: ....

Abstract

There has been controversy over the past years as to whether deformed nuclei are subject to quadrupole vibrations (gamma and β), particularly the β vibrations. Pertaining the gamma $K = 2^+$ vibrations, experimental evidence has been more or less consistent, confirming they indeed exist. On the other hand the situation remains complex for the β vibrations which are characterized by the first low lying 0_2^+ excited state. Using a concept involving pairing it has been suggested that the $K = 0_2^+$ states are simply lowered into the pairing gap by configuration dependent pairing involving the $[505]11/2^-$ neutron orbital. In attempt to understand the true nature of the collective vibrations in relation to the "pairing theory" a suitable approach is studying nuclei in the $N = 88 - 90$ region containing the $[505]11/2^-$ orbital.

The current work seeks to get more insight on the microscopic nature of the aforementioned by studying the spectroscopy of ^{161}Tm. The nucleus of interest ^{161}Tm, was populated using the ^{152}Sm(^{14}N,5n)^{161}Tm reaction with the aid of the AFRODITE array.

The nucleus ^{161}Tm is axially symmetric and it is a relatively good assumption that its core retains the same symmetry. As such the core will behave in a manner similar to that of a neighbouring even-even deformed nucleus. Therefore in this study we were searching for high K structures where the odd proton in ^{161}Tm couples to collective excitations in ^{162}Yb (the core) which

has a very low lying K=2^+ gamma band. The known level scheme of ^{161}Tm has been extended at low spin with new transitions observed. Linear polarization measurements and Direct Correlations for Oriented states (DCO) ratios were performed to confirm the spin and parity assignments of old and new transitions.

The semi-classical model together with alignments have been used to meaningfully describe the quantum behaviour of the collective structures observed in this work. Systematic comparisons have also been used to further understand the structural behaviour of band structures observed in this study. Furthermore experimental B(M1)/B(E2) values for bands involving the [505]$11/2^-$ orbital and other observed strong coupled bands were obtained to confirm quasi-particle configurations.

Acknowledgements

Above everything I am thankful to the Lord Alimghty who has sustained me in all my endevours, and I know has better plans for me ahead. I would also like to express my sincere gratitude to the following people, whose collective efforts helped make this project a success:

- Prof John Sharpey-Schafer "the Living Legend" for introducing me to such an exciting field of physics, believing in me and all his support. Words are not enough to fully express how grateful I am.

- Dr Sifiso Senzo Ntshangase who introduced me to the MANUS programme and because of it, I am where I am today. Thank you for also being a great supervisor.

- Dr Tshepo Dinoko for his unending support, words of encouragement, patience with me and mentoring me. Despite your hectic schedule, you always made time to assist in all aspects, and for that I am very grateful.

- Dr Rudolph Nchodu for his belief in empowering students and continuously ensuring we achieve quality in the tasks at hand.

- Dr Majola for his efforts and contribution in ensuring I understood the physics concepts at hand and pushing me so I could produce good work.

- My dad for his love and support. My mom whose struggles continuously motivate me to be and do better for I wouldn't be here without you.

- My siblings (Thamsanqa, Mmeli and Vuyelwa) who offered words of encouragement and support when needed.

- My colleagues "Jobe", Nontobeko and "Zulu warriour" for working together as a team, it has been a pleasure working with you.

- Nkululeko Zenzele Ndlovu, for being a sister and person insipiring me to do my level best.

- Last but not least Dr Fhumulani Nemulodi, I cannot begin to describe your significance in terms of support and contribution. However thank you for everything.

To those I have not included thank you for your support and efforts.

Contents

List of Figures

List of Tables

Chapter 1

Introduction

1.1 Background

All matter consists of atoms which are the building blocks of all materials. The atoms, as discovered by Rutherford, have all their mass concentrated in the nucleus. The underlying physics of a nucleus can be deduced by studying its behaviour under extreme conditions.

When put under such conditions the nucleus can display a diverse range of properties associated with its elementary particles as shown in Figure 1.1. However due to the complex structure of the nucleus it is difficult to have an exact theory to adequately account for all the observed properties. As a result every nuclear model has its inadequacies due to the breakdown of assumptions that are associated with each model. Different nuclear models have been developed to give to a good approximation, an explanation for the observed properties. The shape of the nucleus is a dominant factor in determining its properties [1]. The majority of nuclei are deformed with some assuming axial symmetry and the non-deformed assuming spherical shape. The behavior of nuclei with different shapes can be described using nuclear

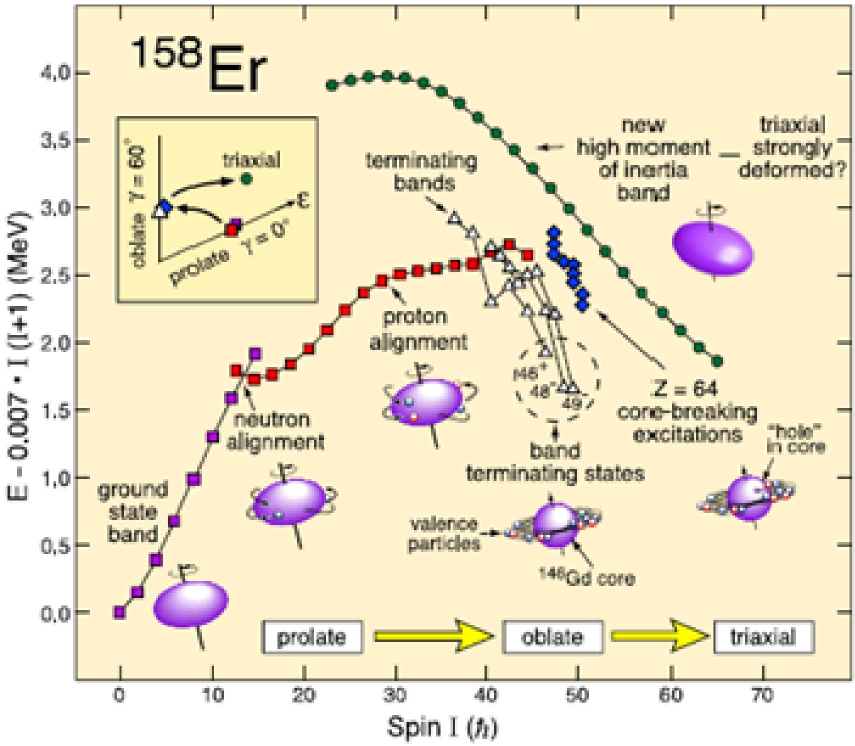

Figure 1.1: An illustration that shows the nucleus ^{158}Er as a good example displaying the phenomena associated with the response of a nucleus to rotational stress as a function of angular momentum [8].

models.

A lot can be learned about the nuclear structure by studying its response to rotational stress and high excitation energies. When nuclei absorb energy they become excited and can use the excitation energy to generate angular momentum in two ways, either collectively or non-collectively as shown in Figure 1.2.

The nucleus studied in this thesis is a rare-earth element with an odd proton groundstate in the $[404]7/2^{+}$ Nilsson orbital. Odd proton deformed nuclei in the rare earth region provide interesting insight on the coupling mechanism of odd nucleons to the even-even core [2]. In nuclei with an odd number of nucleons the total angular momentum is determined by the valence nucleons that are not coupled to zero spin. The rest of the nucleons form what is termed the “core”.

A single nucleon in the outermost shell can couple (interact) to collective excitations of the core to give rise to high K structures. In odd A nuclei it is possible to observe rotational bands built upon intrinsic states and three bands due to the coupling of an odd nucleon state with $K = \Omega$ to collective excitations of the core. The first possibility is a band with a bandhead $K = \Omega$ as a result of coupling of an odd nucleon to the first excited state 0_2^+ in the even-even core. The other two scenarios are the coupling of the odd nucleon to gamma vibrations either parallel to give $K_> =\mid K + 2 \mid$ or anti-parallel to give $K_< =\mid K - 2 \mid$. A good example is in ^{165}Hf with odd proton where both $K_<$ and $K_>$ were observed.

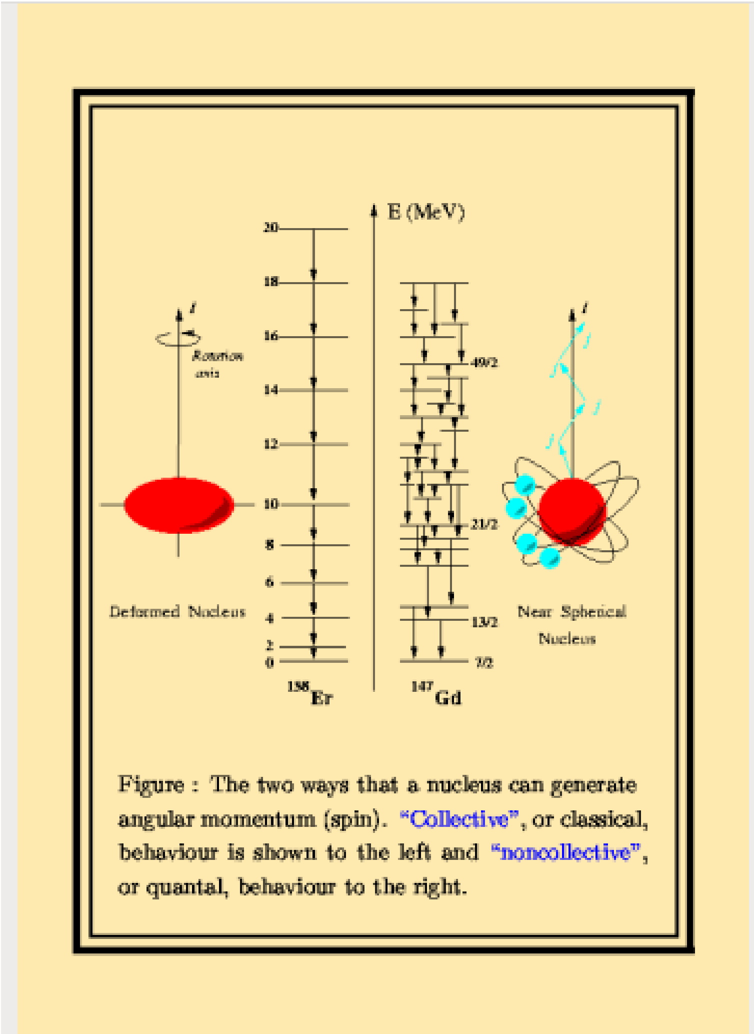

Figure 1.2: A diagram illustrating level schemes associated with collective (^{158}Er) and non-collective (^{147}Gd) behaviour of nuclei [6].

The effect of pairing forces is a dominant feature in nuclei and accounts for various experimental features that cannot be explained by the shell models. The pairing forces result in all even-even nuclei having spin 0^+ ground state which is the first 0^+ state and usually denoted as 0^+_1. In deformed nuclei the pairing forces produce a large gap ($\sim 1-2$) MeV between the ground state and the next intrinsic configuration the rotational bandhead. The states found within the pairing gap have been "traditionally" identified as collective $\beta(K^\pi = 0^+)$, gamma ($K^\pi = 2^+$) and octupole ($K^\pi = 0^-, 3^-$) vibrations. The β vibrational band has been previously assigned as being built on the lowest 0^+_2 state. However, over the past years despite the success of the Collective model proposed by Bohr and Mottleson [3] there have been some questions pertaining the collective motion of nuclei and alternative explanations to describe the β bands. It has been proposed by [4, 5] that the low 0^+_2 states could be due to quadrupole pairing effects involving a pair of neutrons in $h_{\frac{11}{2}}$ oblate orbital. The neutrons occupying the $[505]11/2^-$ orbital are inhibited from scattering into the surrounding down sloping prolate orbitals. As a result the $h_{\frac{11}{2}}$ neutrons form their own 0^+ state within the pairing gap due to being extruded to the Fermi surface by deformation. Amongst the convincing evidence contradicting the old models is that the 0^+_2 states in some nuclei do not show the enhanced E2 transition probabilities as would be expected for a β vibration [6].

Due to the accumulating evidence contradicting the identification of the 0^+_2 states it is being questioned whether the β vibrations are truly collective states. This leaves the octupole and gamma vibrations as the only collective states found within the pairing gap. Experimentally it has been proven a rather difficult task to determine the exact nature of the 0^+_2 states. The focus of this study is to observe the coupling of the odd proton to ($K^\pi = 0^+$)

and ($K^{\pi} = 2^{+}$) bands in the even-even core nucleus ^{162}Yb to give high K structures. The high K structures give information on the underlying micro-structure of ^{161}Tm and the odd proton coupling to its even-even core nucleus ^{162}Yb contributes information about the collective excitations of the core. If the quadrupole pairing is responsible for the 0_2^+ states then the band that results from the coupling of the $h_{\frac{11}{2}}$ neutrons should be absent. This phenomenon is called Pauli blocking. In addition by examining differences in the rotational spectra due to different quasi-proton states, this should give more insight on how the core nucleus is affected by the motion of the valence proton [2].

1.2 Subject of the study

This thesis concentrates on the investigation of discrete gamma-rays emitted in the de-excitation of ^{161}Tm. The electromagnetic interaction is a useful probe as information on energy levels and nuclear states can be obtained by studying the electromagnetic radiation emitted as a nucleus makes a transition from one nuclear state to another. Furthermore the electromagnetic interaction is well understood. Through studying the discrete gamma-rays a level scheme can be built to show the structures present. This thesis is structured so as to relate the findings of the experiment to theories present. Following the current chapter which is an introduction, Chapter 2 provides an overview of some nuclear models that have contributed a lot in understanding the structural behaviour of deformed nuclei such as ^{161}Tm. The experimental methods used in populating ^{161}Tm successfully and analysis techniques that have been used to analyze the data obtained are discussed in Chapter 3. Chapter 4 discusses the results by looking at the gamma-rays produced to give a comprehensive account of the level scheme constructed for ^{161}Tm and other nuclei found in the data (contaminants). Finally, Chapter 5 is a conclusion on what was deduced from the findings and a discussion of results.

Chapter 2

Nuclear Structure

2.1 Development of Nuclear Models

Nuclear models give a simplified description of the complex nuclear structure and interactions between the nucleons. A simplified view of the nuclear structure is achieved by each model making certain assumptions that account for the experimental evidence. In general the nuclear models are distinguished into two categories: the Independent particle model and the Strong interaction model. The Independent particle model assumes a weak negligible interaction between individual nucleons which can be neglected. The strong force between nucleons can be averaged by a "Mean Field". This gives rise to a potential having the shape of the nuclear density, in which the nucleons are confined, which determines the shape of the nuclear density profile. The remaining, or residual interactions between nucleons are then relatively weak and give rise to various versions of the Shell Model [9]. The Strong interaction model assumes the strong interaction between the nucleons which causes them to act coherently such that the nucleus can rotate or vibrate as a whole. An example is the liquid drop model.

All models use different potentials to describe the combined effect of nucleons. The mathematical model of nuclei gets increasingly complicated as one goes from medium mass nuclei to heavy nuclei. One of the major challenges is the mathematics involved in solving the many body problem and the extent of computing that would be needed in understanding the underlying physics becomes more complicated. The nucleus ^{161}Tm is a heavy nucleus, the Nilsson model, Liquid drop model and the Collective model are amongst the most suitable models that can be used to explain its nuclear properties.

2.1.1 Liquid Drop Model

The Liquid drop model describes the nucleus as an incompressible drop of liquid. This model assumes that there is a strong interaction between nucleons and that their movement is coherent. It provides, to a good approximation, an explanation for nuclear properties such as binding energy, mass differences in isobars, energies for β decay and the constant value of density for nuclei having radius:

$$R \propto A^{\frac{1}{3}} \tag{2.1}$$

A vibrating nucleus is analogous to a liquid drop with the volume remaining the same. The binding energies are calculated using the Weizsacker formula (Semi Empirical Mass Formula) and the total binding energy is composed of five components:

$$B_{total} = B_{volume} + B_{surface} + B_{Coulomb} + B_{asymmetry} + P \tag{2.2}$$

which translates to:

$$B(A,Z) = a_v A - a_s A^{\frac{2}{3}} - a_C Z(Z-1)A^{\frac{-1}{3}} - a_{Asy}(A-2Z) \pm \delta \tag{2.3}$$

The extent of contribution of each term to the total binding energy is illustrated in Figure 2.1. The first term is the volume energy and contributes the most to the binding energy. The structure of volume term is based on the short range nature of the nuclear force. It describes how the nucleons do not all interact with each other but only with the immediate neighbouring nuclei. The nucleons in the interior however interact with more nucleons as compared to the nucleons on the surface with fewer neighbours. This reduces the binding energy hence the second term is negative.

There is a loss in binding energy due to the Coulomb repulsion between protons in the nucleus with total nuclear charge Ze and this effect is represented by the third term. The fourth term is the asymmetry term and arises as a result of the greater number of neutrons than protons in medium to heavy nuclei. These nuclei tend to have neutron excess so as to balance the Coulomb repulsion of available protons and an example of such a nucleus is ^{116}Sn shown in Figure 2.2.

The last term is the pairing energy. It is a correction term that is included because of the observed tendency of protons and neutrons to occur in pairs. Nuclei with an even number of nuclei are more stable than odd A nuclei because it would require more energy to break a pair of nucleons than remove an unpaired nucleon from an orbit. The pairing energy is given by δ which is respectively positive, negative and 0 for even-even, odd-odd and odd A nuclei.

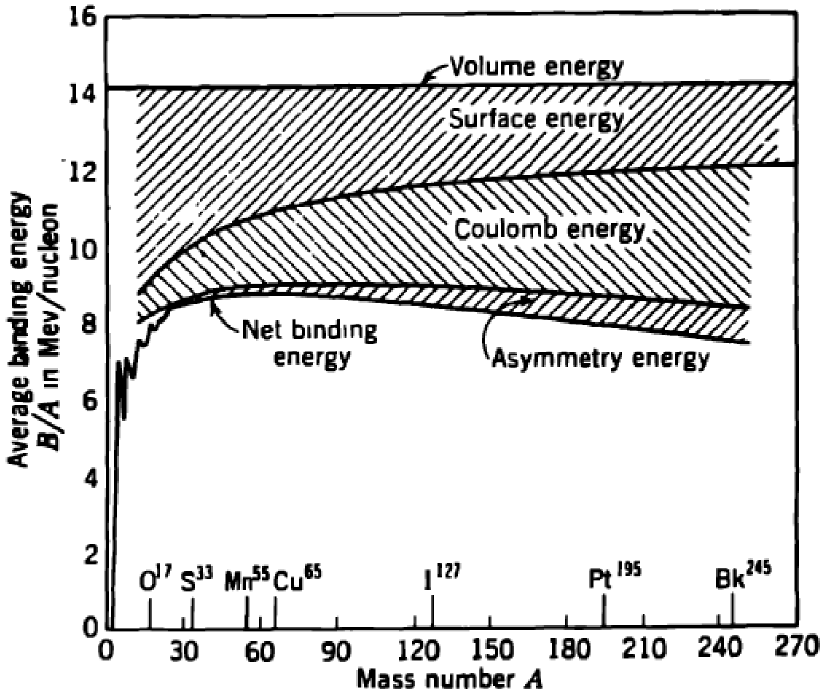

Figure 2.1: An illustration representing the contribution of each term to the total binding energy as interpreted by the Weizsacker formula (Semi Empirical Mass Formula) [9].

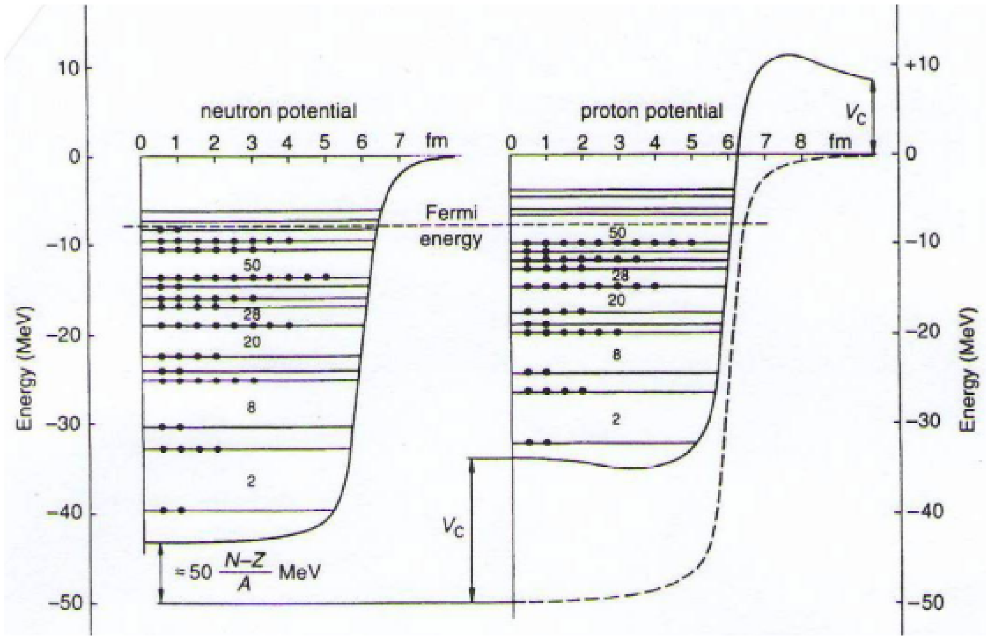

Figure 2.2: An illustration showing ^{116}Sn as an example of a nucleus with $N > Z$ where $N = 66$ and $Z = 50$. The neutron excess results in the last occupied level being higher in energy compared to the case where the number of protons is equal to neutrons for the same value of A [11].

2.1.2 The Nilsson Model

The model is useful in describing single particle levels in nearly all deformed nuclei. It provides a microscopic description of single particle states in close proximity to the nuclear surface as a function of the nuclear quadropole deformation [13].

The axially symmetric quadropole deformations break the energy degeneracy of the shell model. Each configuration (j,l) is split into $(j + \frac{1}{2})$ orbitals and part of the Nilsson orbitals for neutron and proton states are shown in Figure 2.3 and 2.4 respectively. The states associated with the model are labeled by "asymptotic" quantum numbers in the notation $[N, n_z, \Lambda]\Omega^{\pi}$. The Nilsson model is not restricted to the use of one potential but can include different forms of a deformed potential. Figure 2.5 shows the quantum numbers defining Nilsson states. The quantum number Ω is the projection of the angular momentum j of a single nucleon onto the symmetry axis. If there is a state built on more than one or more odd nucleon configurations, then K is the sum of the individual projections Ω i.e;

$$K = \Omega_1 + \Omega_2 + \Omega_3 + \Omega_4 + ... \tag{2.4}$$

Each Nilsson orbit contains only two nucleons corresponding to ±K with the unpaired nucleon defining the ground state because nucleons in either $-\Omega$ or $+\Omega$ orbit have the same energy. If nuclei assume axial symmetry with respect to the z axis and conserve this symmetry, then K becomes a good quantum number because the same value is obtained every time it is measured. The quantum number N is the principle quantum number and represents the major oscillator shells. The wave functions of the nucleons are largest in the z direction. The quantum number n_z is used to denote the maximum number possible for oscillating quanta in the z direction. The

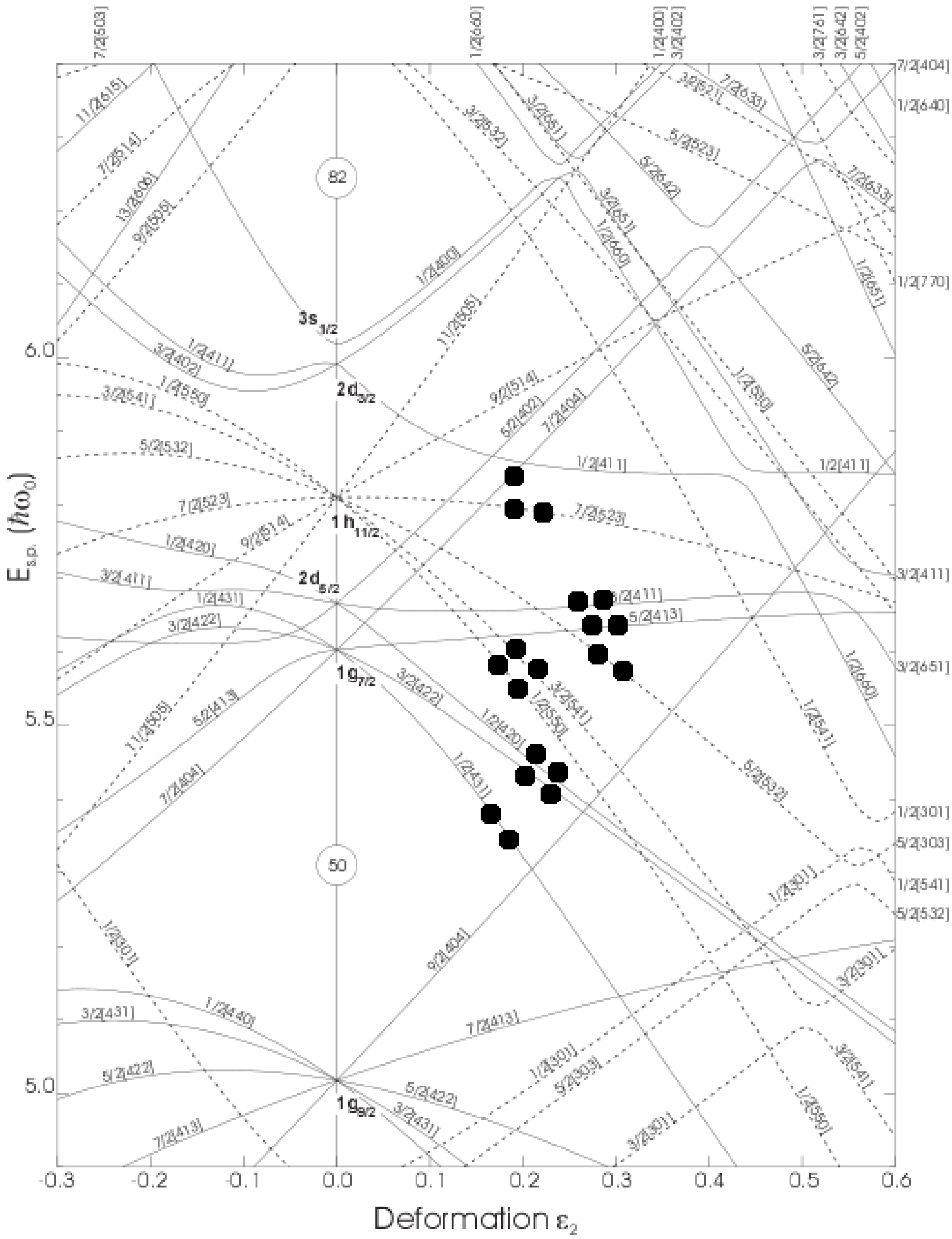

Figure 2.3: The Nilsson proton levels associated with $50 < Z < 82$ showing the single particle energies plotted against the deformation parameter ϵ_2. The dashed lines represent negative parity while the solid lines show positive parity [14]. The valence orbitals that are occupied in the ground state of $^{161}_{69}$Tm$_{92}$ are marked with black dots representing the valence protons[14].

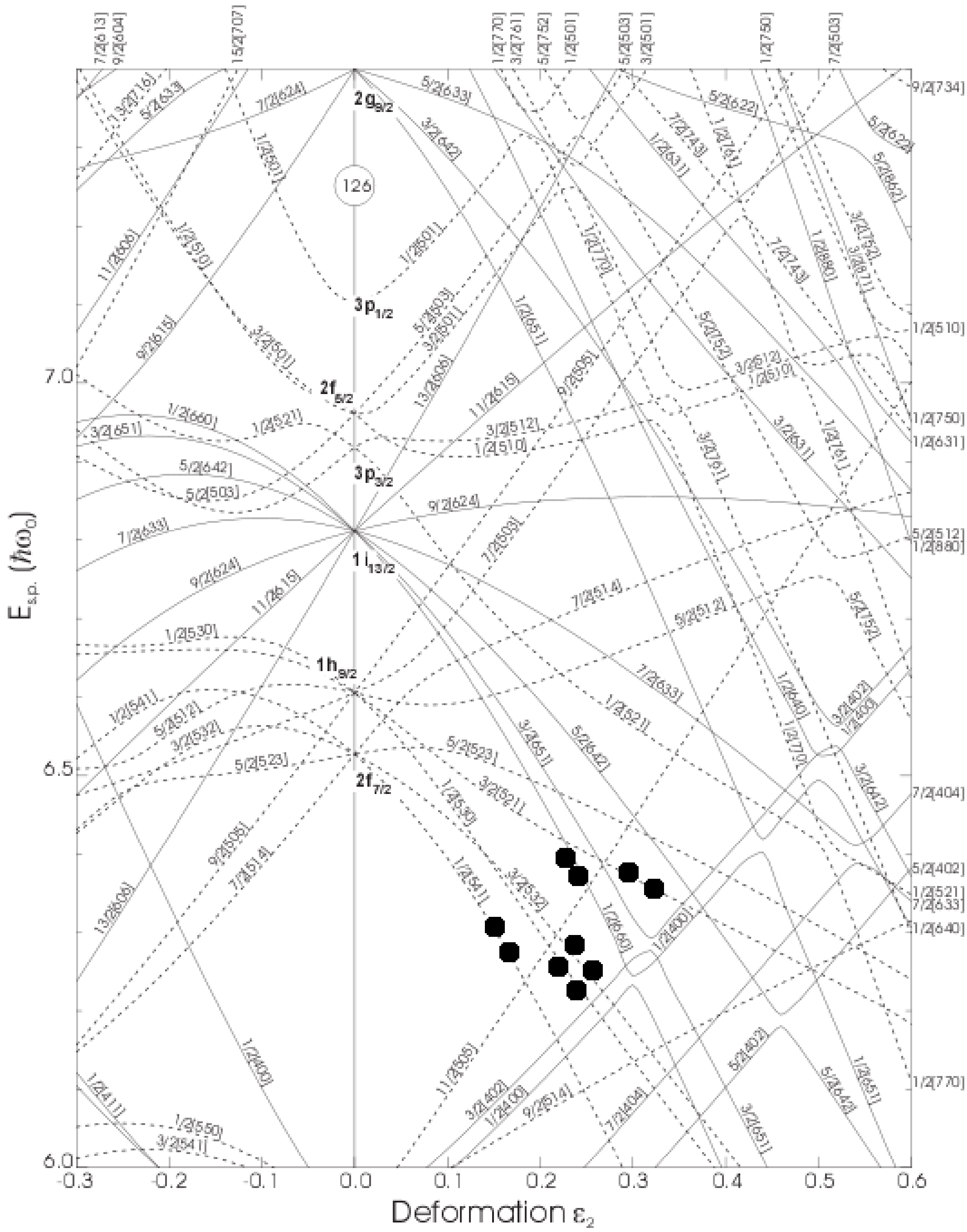

Figure 2.4: The Nilsson neutron levels associated with $80 < N < 126$ showing the single particle energies plotted against the deformation parameter ϵ_2. The dashed lines represent negative parity while the solid lines show positive parity [14]. The valence orbitals occupied by the neutrons in the ground state of $^{161}_{69}Tm_{92}$ are marked with black dots.

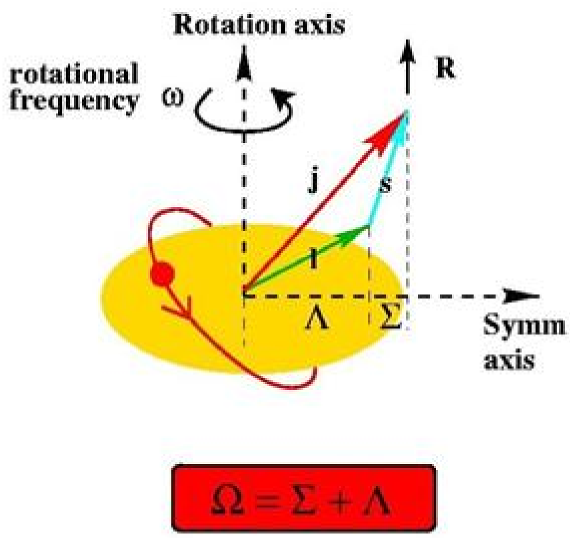

Figure 2.5: A diagram showing the “asymptotic” quantum numbers defining the Nilsson states [15].

maximum value n_z can have is N. The other quantum number used is Λ which is the projection of the orbital angular momentum along the symmetry axis. The two quantum numbers n_z and Λ are related such that their sum retains the parity of N i.e their sum is even if N has positive parity (even) and odd if N has negative parity (odd). The splitting of levels depends on the value of N, the larger the value of N the more steeper (tilted) the slopes.

Prolate and Oblate shapes

In order to describe the quadrupole deformation the model uses two parameters ϵ or β_2. The β_2 parameter describes the eccentricity of the nucleus with spherical nuclei having $\beta_2 = 0$, prolate (rugby ball shape) $\beta_2 > 0$ and oblate (disc shape) has $\beta_2 < 0$. The magnitude of β_2 and hence extent of deformation is denoted by ϵ_2. The nucleus prefers deformed shape to spherical nuclei because the deformed shape minimizes its energy. Amongst the deformed shapes it prefers prolate than oblate for the ground state (equilibrium nuclear deformation). The prolate and oblate shapes are due to the orbital shape of the intrinsic configuration of valence nucleons. Indeed it is the combined effect of these orbitals that causes the distortion of the nuclear shape. Low Ω orbitals i.e $\Omega = \frac{1}{2}, \frac{3}{2}...$ decrease in energy as prolate deformation increases but high Ω orbitals increase in energy as prolate deformation increases. For oblate shapes the behavior is opposite where high Ω orbits are affected more with increasing deformation.

The Lund Convention is a widely used form of parametrization in describing nuclear deformation. It uses the two parameters γ and β. The γ parameter also known as the triaxiality parameter and describes the deviation of nuclear shape from axial symmetry. The Lund Convention shown in Figure 2.6 displays the axis of rotation of a nucleus with varying γ parameter, giving rise to either prolate, oblate or triaxial shape. This convention demonstrates how the γ degree of freedom (axial symmetry) is an indispensable tool in describing the shapes of deformed nuclei.

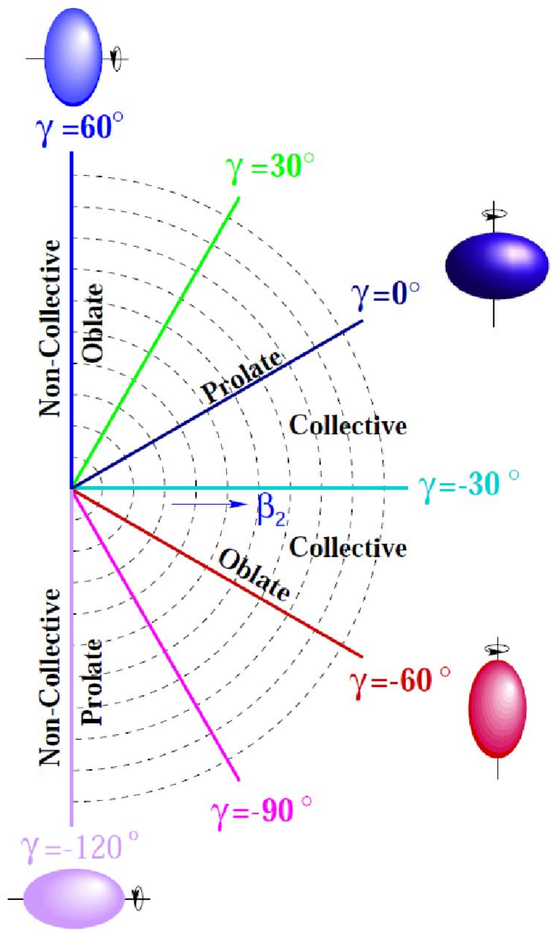

Figure 2.6: Lund Convention showing the axis of rotation of a nucleus with varying γ parameter, giving rise to either prolate, oblate or triaxial shape for quadropole deformations.

2.2 Collective Motion

Nuclei can absorb energy to become excited and thereafter use the excitation energy in different ways. One way is by generating angular momentum which can be done in two ways either by single particle states or collective motion. Single particle states involve motion of nucleons individually and this is possible by promoting nucleons to higher orbits. Collective motion involves the vibration or rotation of the nucleus as a whole as a result of the movement of nucleons together in phase. A widely used model to describe the coherent motion is the Collective model developed by Bohr and Mottleson [3]. In order to describe collective excitations the Collective model which is a macroscopic approach can be used together with the Nilsson model which provides a microscopic approach.

2.2.1 Vibrations

A vibrating nucleus is similar to a liquid drop vibrating with the volume conserved. The phonon is a quantum unit of vibrational energy. Vibrations are observed in near spherical nuclei occurring in nuclei with nucleon numbers just exceeding closed shells. The equilibrium shape is spherical but their radii change during vibration as a function of time:

$$R(t) = R[1 + \Sigma_{\lambda=2}\Sigma_{\mu=-2}a_{\lambda\mu}Y^{\mu}_{\lambda}(\theta,\phi)] \tag{2.5}$$

The equation describes the radius of a vibrating nucleus in the direction of the Euler angles (θ,ϕ). The term $a_{\lambda,\mu}$ represents the expansion coefficients and describe the amplitude of the spherical harmonics $Y^{\mu}_{\lambda}(\theta,\phi)$. It is convenient and often useful to use spherical harmonics because they form a complete orthonormal basis and any function can be represented in that basis. In order to classify the type of vibration the term λ is used to describe the multipolarity and different shapes possible for a vibrating nucleus. The parity for vibration is defined by $\pi = (-1)^{\lambda}$, where λ is even for reflection symmetric and λ is odd for reflection asymmetric. Because the volume of a nucleus is considered as constant and are dealing with stationary nuclei therefore we neglect the term $\lambda = 1$ as it indicates a shift in the center of mass and displacement of the nucleus. The next possible modes of vibration are $\lambda = 2$ representing quadrupole vibrations and $\lambda = 3$ for octupole vibrations. For the purposes of this study the focus was only the quadropole vibrations.

The quadrupole vibrations are further distinguished as either β or gamma vibrations as illustrated in Figure 2.7. The two parameters β and γ describe the nuclear shape corresponding to the vibration where β describes how deformed the nucleus is and γ describes the extent to which a nucleus assumes axial symmetry. The two parameters are related to nuclear radii to show the change in the radius $(R_{z,y,x} - R_0)$ along different axes using the equations:

$$\delta R_z = \sqrt{\frac{5}{4\pi} R_0 \beta cos\gamma} \tag{2.6}$$

$$\delta R_x = \sqrt{\frac{5}{4\pi} R_0 \beta cos(\gamma - \frac{2}{3\pi})} \tag{2.7}$$

$$\delta R_y = \sqrt{\frac{5}{4\pi} R_0 \beta cos(\gamma - \frac{4}{3\pi})} \tag{2.8}$$

The β vibrations conserve cylindrical symmetry and only the β value fluctuates along the symmetry axis. They are also referred to as one phonon states. The γ vibrations occur in the (x,y) directions and are perpendicular to the symmetry axis.

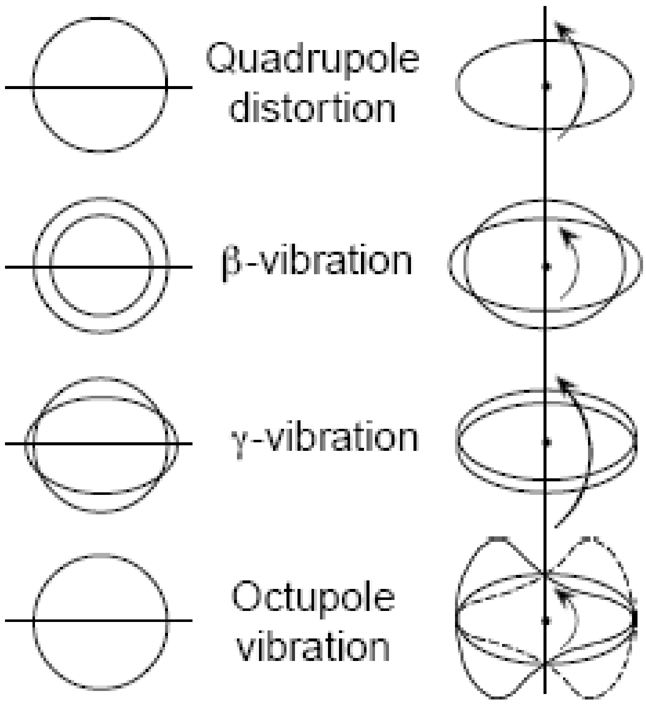

Figure 2.7: An illustration showing the different types of vibrations possible: The β are due to oscillations along the symmetry axis, the gamma vibrations are oscillations perpendicular to symmetry axis and the octupole vibrations resemble a pear deformed shape [17].

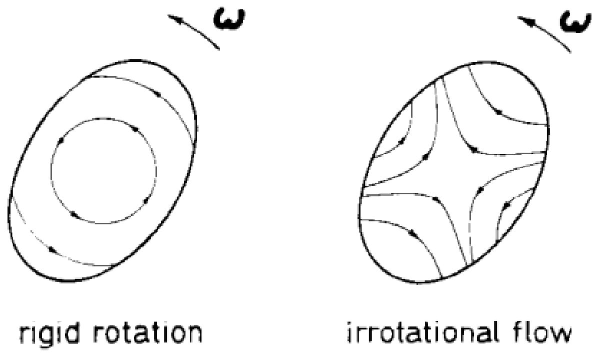

Figure 2.8: The diagram shows the two simplifying models to describe the types of rotating bodies as described by Bohr [10]. They are classified by the velocity fields where in the rigid rotor they cause motion of the whole nucleus as a solid body and in the irrotational flow the velocity fields are proportional to the deformation causing the nucleus to behave more like an incompressible liquid drop [10].

2.2.2 Rotation

Collective rotation is observed in non-spherical nuclei found in the region $150 < A < 190$. Quantum mechanically spherical nuclei are not regarded as rotating bodies because one cannot tell if they rotated as all their axes are axes of symmetry i.e it is not an observable. However deformed nuclei with axial symmetry can rotate around one axis perpendicular to their symmetry axis. In classical mechanics rotating bodies can be classified by the effective moment of inertia I_{eff} either as rigid rotors or having irrotational flow as shown in Figure 2.8.

The rigid rotor is regarded as a three dimensional solid body with a symmetric top and rotating as a whole, while irrotational flow is treated as an incompressible inviscid liquid drop. The effective moments of inertia represent how the nucleus responds to rotations.

As the nucleus rotates faster it gains energy and angular momentum. A gamma-ray is emitted by the nucleus as it makes a transition from one nuclear state to another. The sequence of nuclear states forms the rotational band. The gamma-ray spectrum of a rotational band has constant spacing between the successive gamma-ray peaks which is given by;

$$\Delta E_\gamma = E_\gamma(I) - E_\gamma(I-2) \tag{2.9}$$

$$= \frac{[(2I-1)-(2I-1-2)]\hbar^2}{\mathcal{J}} \tag{2.10}$$

$$= \frac{4\hbar^2}{\mathcal{J}} \tag{2.11}$$

The rotational energy of a nucleus is the sum of the rigid rotor energy and intrinsic energy. The equation represents energies of each excited nuclear state. For even nuclei with bandhead spin $I^\pi = 0^+$, $K = 0$, and all the angular momentum is usually assumed to be due to the rotational motion and the resulting energy states are of a rigid rotor:

$$E_{rot}(I) = \frac{\hbar^2}{2\mathcal{J}} I(I+1) \tag{2.12}$$

where only even values of I are allowed for nuclear states in a rotational band. In odd A nuclei using the Nilsson model, the nuclear states are as a result of the intrinsic states, superimposed on the rotational motion of the core.

2.3 Collective model

The Collective model proposed by Bohr and Mottleson is a geometrical model that describes the macroscopic motion and collective excitations in medium to heavy nuclei. It assumes a strong interaction in nuclei that causes them to move in phase hence giving rise to collective vibration or collective rotation. The model is successful in predicting nuclear levels that arise due the coupling of vibration to rotation. Collective excitations arising from the coupling of vibrations to rotations are given by the Bohr-Hamiltonian which is formed from the concept of summing the energy due to rotation and vibration;

$$E = E_{vibration} + E_{rotation} \tag{2.13}$$

The equation in detail is expressed as:

$$E(n_\beta, n_\gamma, I, K) = \hbar\omega_\beta(n_\beta+\frac{1}{2})+\hbar\omega_\beta(2n_\gamma+\frac{1}{2}K+1)+\frac{\hbar^2}{2\mathcal{J}}[I(I+1)-K^2] \tag{2.14}$$

Equation 2.14 shows calculated energies for quadropole vibrations that can be coupled to a rotation [16]. The first term represents a β vibration, the second a gamma vibration and the last a rotation. The number of phonons excited in a β or gamma vibration are denoted as n_β and n_γ respectively. Pairing in even-even quadropole deformed nuclei produces a gap between the ground state and next intrinsic configuration which is the rotational band. According to the model any states found within that gap are identified as collective $\beta(K^\pi = 0^+)$, gamma ($K^\pi = 2^+$) and octupole ($K^\pi = 0^-$ and 3^-) vibrations.

For $n_\beta = 1$ and $n_\gamma = 0$, a rotational band is formed with a band energy of $E_x = \hbar\omega_\beta$ with spin and parity of $I^\pi = 0^+$ corresponding to a projection on the symmetry axis of $K^\pi = 0^+$. Traditionally this band has been identified as a β vibrational band. The ground state is regarded as the first 0^+ i.e 0^+_1 and the lowest excited state for the β band is the second 0^+ i.e 0^+_2. The first excited $K^\pi = 2^+$ band is the gamma vibration band with $n_\gamma = 0$ and band head excitation $E_x = \hbar\omega_\gamma + \frac{\hbar^2}{\mathcal{J}}$.

2.3.1 Particle-core Coupling

To account for the observed interplay between single particle states and collective motion, it is necessary to consider the coupling of the valence nucleons which move more or less independently around the core. The coupling scheme can be observed in axially symmetric nuclei. There are two extremes of particle core coupling which are the Deformation aligned (strong coupling) and the Rotation aligned (weak coupling).

A rotating nucleus generates two types of inertial forces which are the centrifugal force and Coriolis force. The centrifugal force acts radially and the Coriolis force acts so as to align the angular momentum of valence nucleons along the rotation axis. The effects of the Coriolis force are more pronounced in the rotation aligned case where high j orbitals are occupied. The Coriolis force is described by;

$$F_{Coriolis} = -2m\omega \times v \tag{2.15}$$

The force acts in opposite directions for nucleons traveling in time reversed orbits. As the rotational frequency increases two nucleons in a time reversed orbit split and begin to move in a different equal but opposite orbit as shown in Figure 2.10. It is at this point that the angular momentum of each nucleon begins to align with the axis of rotation with aligned angular momentum given by;

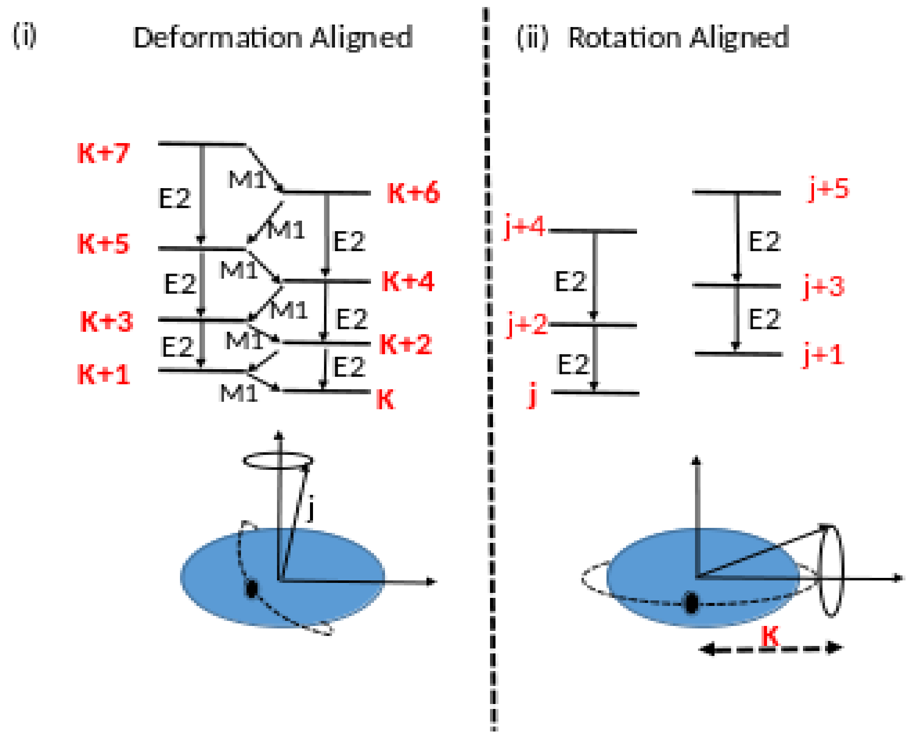

Figure 2.9: The two extremes of particle core coupling which are characterised by the type of orbit the valence nucleons assume and in turn determines the value of K (whether the projection on the symmetry is large or small) modified from [23].

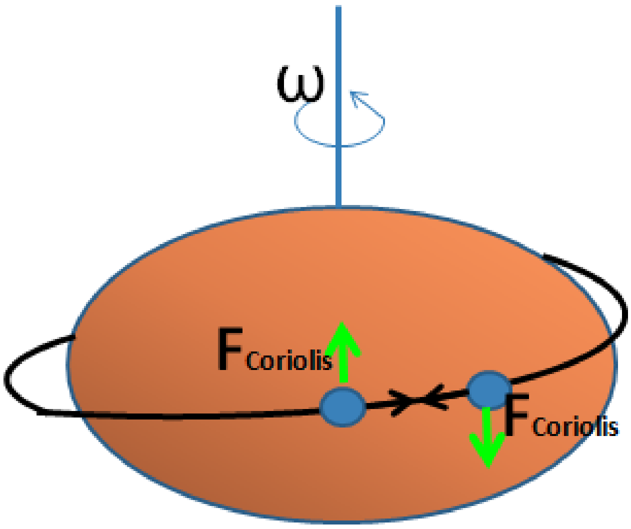

Figure 2.10: An illustration showing the direction of the Coriolis force for nucleons traveling in time reversed orbits. The force acts in opposite directions for the two nucleons.

$$i_x = \hbar\sqrt{I(I+1) - K^2} \tag{2.16}$$

In the rare earth region the high j proton $h_{\frac{11}{2}}$ and neutron $i_{\frac{13}{2}}$ orbitals are good examples that display the effects of the Coriolis force.

In the case of strong coupling the valence nucleon(s) have a large projection of angular momentum on the symmetry axis (i.e large values for K). A single nucleon in this case can couple to the core giving rise to high K structures. The deformation aligned case is characterized by bands with M1 interband transitions.

In general for any odd A nucleus if the value of J, π, μ and Q are known then one can deduce:

(i) Information on the intrinsic shape of the deformed core

(ii) The kind of potential the nucleons “feel” due to the 0^+ core and type of orbit it assumes [17].

2.4 Pairing Correlations

The pairing interaction accounts for a number of experimental features that cannot be accounted for by the Shell models. Pairing forces are the attractive component of the nucleon-nucleon force and cause nucleons to move in time reversed orbits which is the most efficient possibility without violating the Pauli Principle. The two nucleons have identical quantum numbers except for the magnetic quantum number where they have opposite signs. Pairing correlations are responsible for all the ground states of even-even nuclei with spin parity $J^\pi = 0^+$.

If two nucleons are moving in time reversed orbits there is a high probability for them to collide and scatter into another time reversed orbit as shown in Figure 2.11 part (a). This scattering can occur near the Fermi surface because of the availability of unoccupied orbits to scatter into. However further below the Fermi surface this scattering is blocked i.e forbidden by the Pauli Principle since the orbits are occupied. This type of scattering is dependent on the energy difference between the two levels (orbitals) involved and is called monopole pairing. However, there exists another type of pairing that is dependent on relative orientation of the orbitals involved accounting for the overlap of the wave functions of the respective orbitals and [1, 4, 5, 18] has described it as quadrupole pairing.

The scattering of two nucleons from one time reversed orbit to another modifies the Fermi surface whereby it is no longer sharp and defined as shown

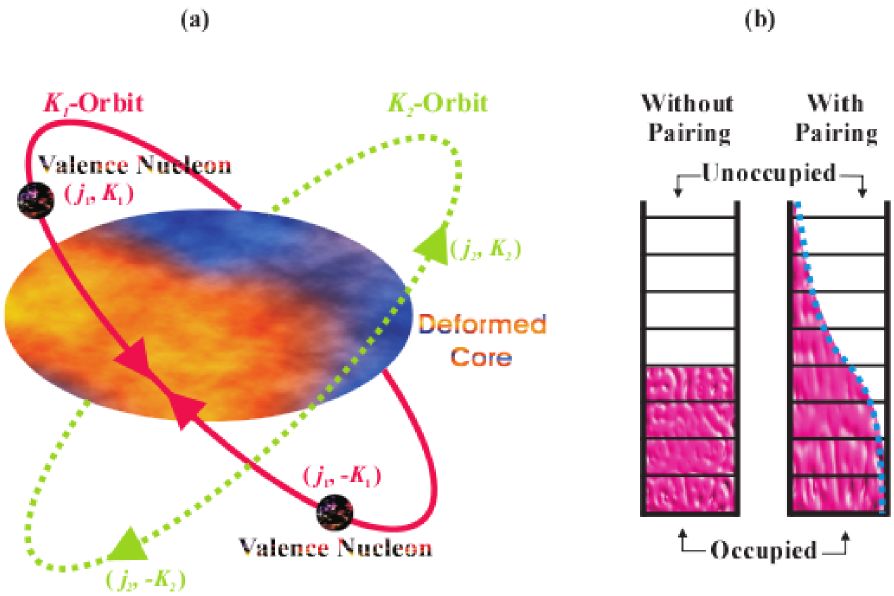

Figure 2.11: An illustration showing how the pairing results in the smearing of the Fermi surface as nucleons scatter from one time reversed orbit to another [14].

in Figure 2.11 but rather smeared introducing the concept of a quasi-particle. The quasi-particle is considered a "hybrid" type of particle and can behave as either a hole or particle.

When the Coriolis force acting in opposite directions as shown in Figure 2.10 is large enough, it forces the two nucleons to align their angular momentum to the rotation axis. This phenomenon is observed at a specific crossing frequency and is called band crossing. It usually corresponds to a change in the yrast sequence. The most alignable configurations are those with high Ω as it easier to tilt the nucleons to the rotation axis due to them being closer to it. The first band crossing corresponds to $i_{\frac{13}{2}}$ neutrons and is termed the AB crossing using a labeling convention from the Cranking Shell model [24].

Experimentally it is possible to predict on a "relative" scale the associated pairing correlations for aligning quasi-particles. This can be done by measuring AB band crossing systematics and this is an indication of how much a particular nucleus has to rotate in order to overcome the pairing force. If an odd A nucleus is considered with an unpaired quasi-neutron configuration, then it is not possible to scatter a pair of nucleons into that configuration as it is Pauli blocked thereby reducing pairing correlations. As a consequence the nucleus does not need to rotate as much to overcome the already reduced pairing correlations and hence the observed crossing frequencies are lower for nuclei with odd quasi-neutron configurations.

However there are a few exceptions where the crossing frequency is not reduced and such a case is that of a quasi-neutron occupying an oblate configuration in the vicinity of aligning prolate orbitals. The scattering from such an oblate configuration is inhibited because of the minimal overlap between the occupied oblate orbital and aligning prolate orbitals. Therefore, pairing correlations in such a case are not reduced (the scattering is unlikely to occur) and the crossing frequency will be observed at a higher value. Furthermore this is an indication that pairing correlations are also configuration dependent unlike the case of monopole pairing.

Chapter 3

Experimental Techniques

3.1 Introduction

The nucleus is a many body system with a wide range of properties associated with its elementary particles. Many of the properties are still not well understood because there is no exact theory to explain them fully. Scientists have settled on nuclear models to explain some of the properties. In order to test the validity of the nuclear models experiments are performed using nuclear reactions. The techniques and type of nuclear reactions used depend on the experimental feature that is being investigated and nucleus being studied. For most nuclei with two mass units away from stability, it is not possible to investigate their structural properties using direct nuclear reactions therefore gamma-ray spectroscopy becomes the most productive way of studying their structure.

A commonly used approach used in Nuclear physics experiments involves exposing nuclei to extreme conditions and then studying their response to such conditions. In this study the nucleus ^{161}Tm was exposed to high excitation energies using a heavy ion fusion evaporation reaction. The aim of this study is to investigate the nature of low to medium spin states formed by ^{161}Tm as it de-excited to the ground state. This chapter discusses the experimental techniques that were used to obtain data. The methods and techniques that were used to carry out the analysis are also discussed.

3.2 Reaction selection

Before performing an experiment there are a number of factors that need to be taken into consideration in order to successfully populate the nucleus of interest. Amongst these are the suitable beam energy together with the right choice of a target. In this work, calculations performed using the Projected Angular Momentum Couple Evaporation (PACE4) [19] simulation code were used to identify the optimum beam energy to maximize cross section and angular momentum input for the channel of interest. PACE4 is a computer program that uses a Monte Carlo simulation to predict the yield of producing nuclei in relation to the beam energy. Figure 3.1 shows the PACE4 simulations performed for the current experiment.

For fusion to occur a beam energy above the Coulomb barrier is needed. Increasing the beam energy will increase the maximum angular momentum input for the channel of interest. However, increasing the beam energy too high has an undesired side effect of increasing the excitation energy of the compound nucleus, which causes more particles to be evaporated resulting in more contaminants.

When deciding on the target thickness there is the option of selecting either a thick (> 1 mg.cm^{-2}) or thin target (< 0.5 mg.cm^{-2}). The advantage of using a thick target is that more events are accumulated for the experiment due to more interactions. A thick target also enables the stopping of most

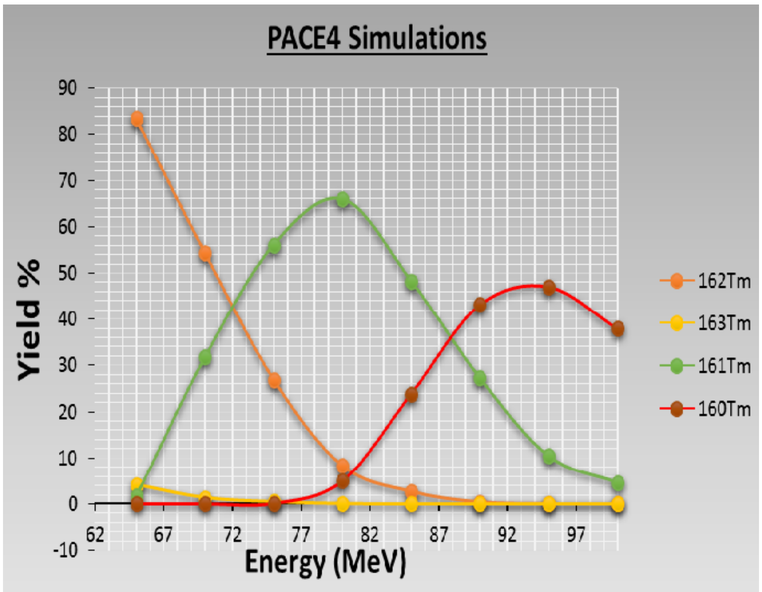

Figure 3.1: PACE4 simulations for the ^{152}Sm(^{14}N,5n)^{161}Tm reaction cross section. Also shown in the figure are possible nuclei or contaminants that can be produced from the reaction.

recoils within the target eliminating the necessity to use a backing. However the slowing down of recoils introduces Doppler broadening of peaks, from the decay of levels occurring faster than $\sim$ ps after the reaction resulting in the appearance of wide peaks with shifted centroids in the projection spectrum. With a thin target however there is better resolution because recoils are not stopped within the target. A thin target produces fewer interactions hence less accumulated events. To improve the statistics in thin targets they can be stacked together. This has the advantage of ensuring that most of the compound nuclei will decay while recoiling fully. In this experiment a thick target of 5 mg.cm^{-2} was used and it was formed from stacking together two targets of 2.5 mg.cm^{-2}. The selected thickness was motivated by the necessity to stop most of the recoils and the need to accumulate a greater number of events to improve the statistics. A ^{152}Sm target was selected because that particular isotope has a high isotopic purity of 98.3 percent thereby reducing the risk of populating contaminants due to impurities.

3.2.1 Heavy-Ion Fusion Evaporation

If two nuclei fuse at an energy above the Coulomb barrier a fusion reaction takes place. The impact parameter (vertical distance between the trajectory of the projectile and the center of the nucleus) can be used to distinguish the type of heavy ion collision that can occur. Fusion reactions occur at small values of the impact parameter. The Coulomb barrier is given by:

$$V_C = \frac{Z_1 Z_2}{4\pi\epsilon_0 R} \tag{3.1}$$

where Z_1 and Z_2 are the atomic numbers of the projectile and the target respectively, R is the distance between the two nuclei and ϵ_0 is the permittivity of free space. The distance between the two nuclei is calculated as a function of the mass numbers:

$$R = 1.36(A_1^{\frac{1}{3}} + A_2^{\frac{1}{3}}) + 0.5fm \tag{3.2}$$

where A_1 is the mass number of the projectile and A_2 of the target. Once the fusion reaction occurs, an intermediate heavy nucleus is formed which lives for approximately $10^{-15} \rightarrow 10^{-19}$ s. The amount of angular momentum transferred by the projectile to the compound nucleus is given by the cross product of the impact parameter and the linear momentum of the beam. Figure 3.2 illustrates how the heavy ion fusion reaction proceeds in time scale to form the stable ground state nucleus of ^{161}Tm. The compound nucleus formed is in an excited state and is rotating rapidly with frequency hω of ~ 0.75 MeV equivalent to $\sim 2 \times 10^{20}$ Hz. The compound nucleus can dissociate in various ways called the exit channels. Subsequent dissociation of the compound nucleus depends on the entrance channels which refer to the reactions that formed the compound nucleus. Evaporation of particles takes place first to take away most of the energy of the compound nucleus. Neutrons are preferentially evaporated first followed by charged particles like alphas and protons due to the Coulomb barrier.

The final phase of a heavy ion reaction is the emission of gamma-rays as shown in Figure 3.3. The compound nucleus then decays by statistical gamma-rays that cool the nucleus towards the yrast line and carry very little angular momentum. After the emission of statistical gamma-rays there is a decay to the ground state by discrete gamma-rays. Unlike the statistical transitions, the discrete gamma-rays remove most of the angular momentum and are represented by transitions that are more or less parallel to the yrast line. The gamma-rays of interest in the current study are the discrete gamma-rays because they allow for the analysis of gamma-ray transitions and the

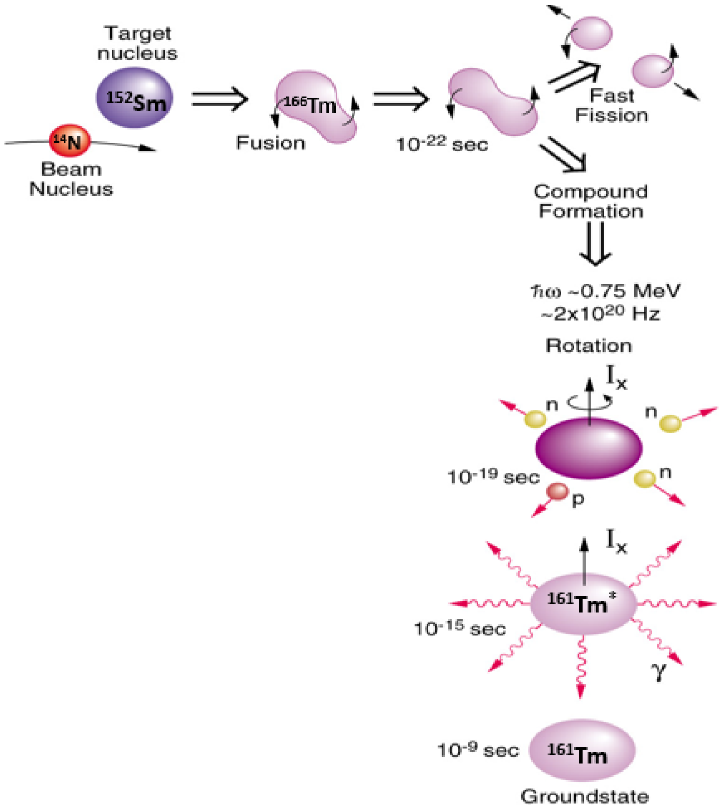

Figure 3.2: Illustration of the heavy ion fusion reaction ^{152}Sm(^{14}N,5n)^{161}Tm forming the compound nucleus ^{166}Tm and its decay to form a stable ground state nucleus.

construction of a level scheme to graphically represent the specific decay paths.

3.3 Experimental gamma-ray Spectroscopy

3.3.1 Interaction of gamma-rays with matter

Gamma-rays are electromagnetic waves and do not have intrinsic charge, hence they cannot be directly detected. However they gamma-rays are detected by the ionization they produce along one of the three main processes as they interact with matter. In this work we focus on only three types of interaction of gamma-rays with matter: Photoelectric absorption, Compton scattering and Pair production. The mode of interaction depends on the energy of the photon and atomic number of the target nucleus. Photons will interact with the whole atom to give photoelectric absorption, or with the electric field of the nucleus in pair production or with only one electron in the Compton Effect. Figure 3.4 shows the competing mechanisms that become dominant depending on the photon energy and atomic number.

3.3.2 Photoelectric absorption

The photoelectric process is dominant at energies less than < 0.1 MeV and in nuclei with medium to high values of the atomic number. Free electrons cannot absorb photons completely, however, it is possible for electrons that are tightly bound such as those in the K-shell. The photon ejects an electron from the K or L shell of the atom. This leaves the atom in an excited state. In attempt to achieve stability after being excited, the atom de-excites in two ways either through emission of X-rays or electrons. The incident photon

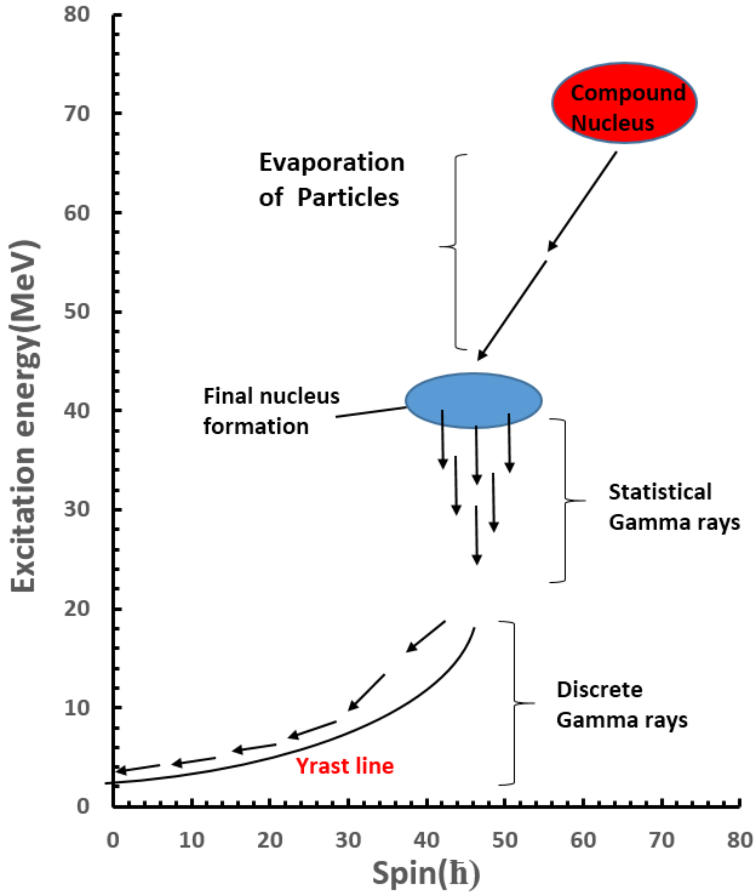

Figure 3.3: Two types of gamma-rays are emitted by the nucleus formed after particle evaporation: the statistical gamma-rays cool the nucleus towards the yrast line and carry little angular momentum while the discrete gamma-rays remove most of the angular momentum.

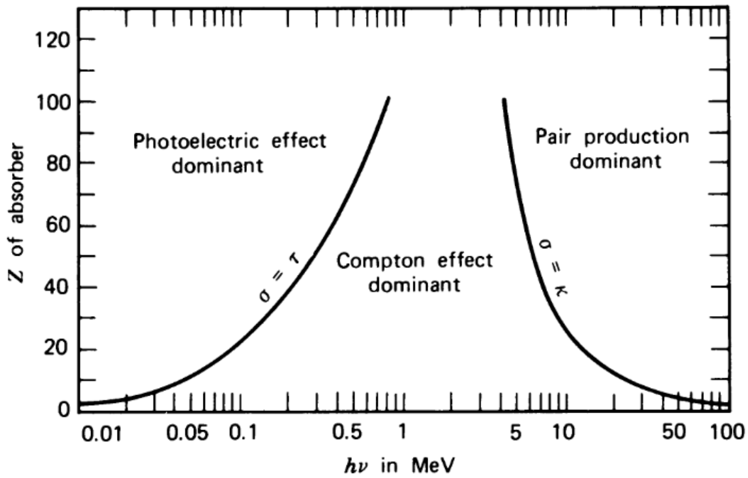

Figure 3.4: The diagram illustrates the dependence of the type of gamma-ray interaction on the gamma-ray energy and atomic number Z of the material [25].

will eject an electron only if the photon energy $h\nu$ is greater than the energy needed to free an electron (binding energy). The kinetic energy of the ejected electron is given by the difference between the energy of the incoming photon and the binding energy of the rest electron:

$$E_e = E_\gamma - E_B \tag{3.3}$$

where E_e, E_γ and E_B represent the energy of the ejected electron, incident photon and the binding energy of the rest electron respectively.

3.3.3 Compton Scattering

The most dominant interaction of gamma-rays with matter is Compton scattering. It affects the quality of the spectra obtained by contributing a large background. This process proves to be quite problematic when dealing with germanium detectors due to the large proportion of gamma-rays entering the detector and Compton scattering out of the detector. The Compton effect is almost independent of the atomic number but however depends strongly on the number of electrons and hence on the density of the material [26]. In this process the photon is deflected by an electron inside the target material as shown in Figure 3.5.

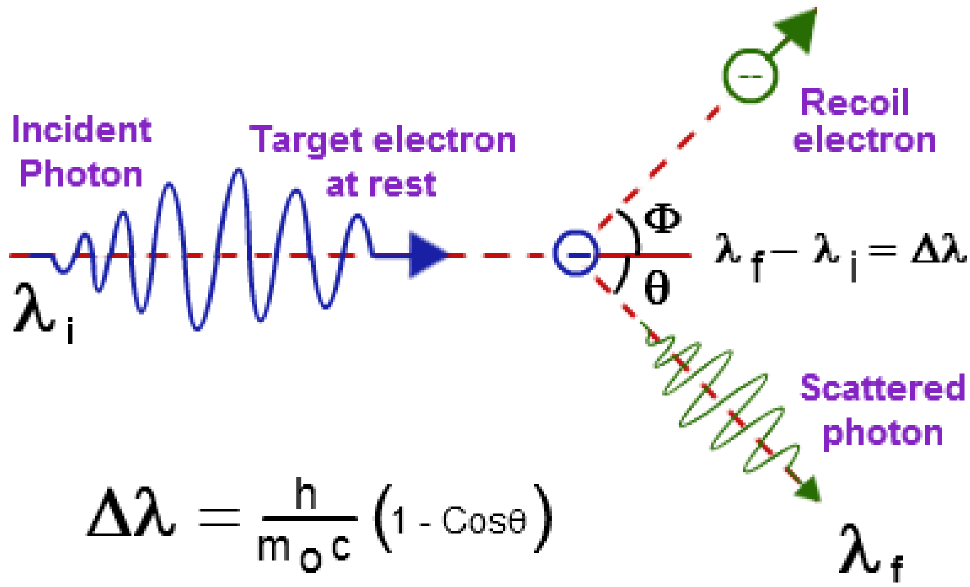

Figure 3.5: A diagram showing the process of Compton Scattering where an incident photon collides with an electron at rest in the medium, causing it to scatter off at an angle [27].

During the collision the incident photon transfers some momentum and energy to the loosely bound electrons considered to be at rest. The scattered photon has less energy hence longer wavelength. It is necessary to use a relativistic approach in the theory of Compton scattering because photons are considered to be massless and the energy transferred during the collision is comparable to the electron rest mass energy. Using the conservation of energy and momentum the energy of the scattered photon E_f is related to the energy of the incident photon E_i and the scattering angle θ by the equation:

$$\frac{1}{E_f} - \frac{1}{E_i} = \frac{1}{E_0}(1 - cos(\theta)) \tag{3.4}$$

where $E_0 = m_e c^2$ is the rest mass energy of an electron.

3.3.4 Pair Production (Annihilation Peaks).

Pair production only takes place if the photon energy is more than twice the rest mass of an electron (2×0.511) which is 1.022 MeV. The interaction occurs mainly in the range of the Coulomb field of the nucleus where a photon is converted into an electron-positron pair. The electron-positron pair will have total energy equal to the incident photon:

$$hf = (E_+ + m_0 c^2) + (E_- + m_0 c^2) \tag{3.5}$$

where E_+ is the kinetic energy of the positron, E_- is the kinetic energy of the electron and $m_0 c^2$ is the rest mass energy of an electron. If the photon has energy greater that 1.022 MeV then the excess energy is converted into kinetic energy of the electron-positron pair. The electron-positron pair will lose the kinetic energy to the absorbing medium as they slow down due to the stopping power of the medium. When the positron has sufficiently low energy, it will combine with an electron in the absorbing medium. The energy resulting from pair annihilation is in the form of back to back photons of 0.511 MeV. Corresponding to one photon escape, a peak of 0.511 MeV below the full energy peak will be recorded by the detector. Also double peaks at 1.022 MeV below the full energy peak will be observed due to two photons escaping.

3.3.5 Semi-conductors

In this experiment the gamma-ray detectors were HPGe (High Purity Germanium) semi-conductor detectors, which are efficient for gamma-ray detection. Semi-conductors are widely used because the band gap is small and deep depletion layers can be achieved. Their conductivity is highly sensitive to the presence of impurities.

In semi-conductors the atoms are arranged to form specific energy levels with the highest occupied energy band being the valence band followed by a conduction band with a region separating the two. Figure 3.6 illustrates the band structure in insulators, conductors and semi-conductors.

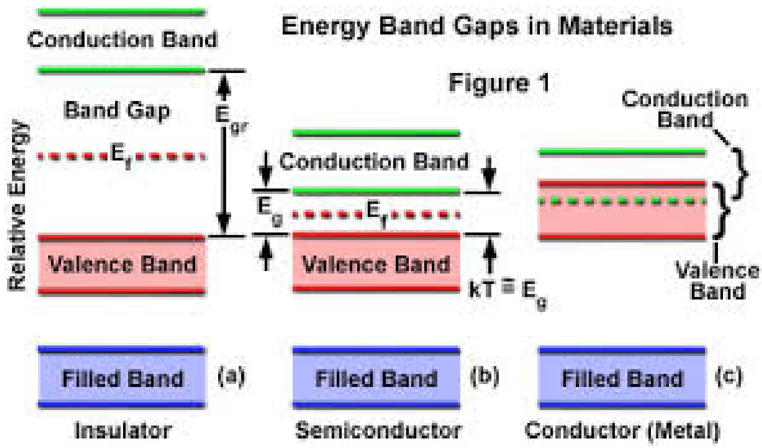

Figure 3.6: The band gap of different types of materials vary as shown above. In a semi-conductor, the band gap is small enough that electrons can be moved from the orbitals in the valence band to the orbitals in the conduction band [28], while in insulators the band gap is significantly larger. In conductors either the band gap is small or there is no band gap separating the conduction band and valence band.

There are two types of semi-conductors namely, intrinsic and extrinsic semi-conductors. In intrinsic semi-conductors the number of electrons present in the conduction band is equal to the number of holes. Electrons can move from the valence band to the conduction band through thermal electric excitation or by applying an external field. An electron hole pair is then formed by which it is possible for the electron to move into the conduction band and for the hole to move into the valence band.

As opposed to intrinsic semi-conductor devices, a small amount of impurity can be added to a semi-conductor to form extrinsic semi-conductors. The extrinsic semi-conductors are further classified into either p-type (acceptor impurities) or n-type (donor impurities). Impurities lower the energy needed to form an electron hole pair and this tends to create noise. Figure 3.7 shows the different electronic band structure in n- and p-type semi-conductors.

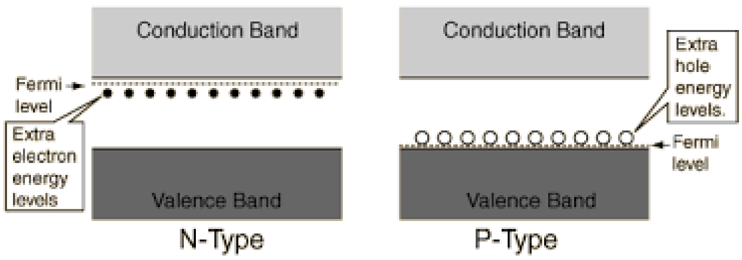

Figure 3.7: The diagram shows the different charge carriers that make up the n and p type semi-conductors [29]. The p-type have a deficiency of electrons hence holes are the majority carriers, while the n-type have an excess of electrons which become the majority carriers.

An important parameter for semi-conductors is the depletion depth given by:

$$d = \sqrt{\frac{2\epsilon V_0}{eN}} \tag{3.6}$$

where ϵ is the permittivity of the material, V is the reverse bias voltage, e is the elementary charge of an electron and N is the net impurity of the semi-conductor. The net impurity of the semi-conductor should be kept at a minimum to increase the depth of the depletion region. There are two ways of minimizing the impurity concentration. One way is compensating the present residual impurities by adding an opposite type impurity. In Si and Ge this approach can be employed by adding a p-type impurity such as Li in a process called Lithium ion drifting. Another way of improving the impurity concentration is by purifying the crystal further by a refining process called the zero refining technique. The HPGe detectors are purified using this technique. There are two types of configurations possible for the geometry of the HPGe detectors and they are the planar and coaxial. The detectors used in this experiment were of n-type coaxial configuration. The n-type coaxial geometry consists of a cylindrical germanium crystal where the outer contact is a p^+ contact formed by doping with p-type impurities. The inner surface is a n^+ contact.

3.4 Experimental Apparatus

An accelerator is used to deliver the beam of projectile particles to the target. In this experiment the iThemba LABS Separated Sector Cyclotron (SSC) was used to produce the ^{14}N beam at an energy of 82 MeV. The SSC is a circular accelerator consisting of four separate magnet sectors each with mass of 350×10^3 kg , diameter of 13 m and are separated by a sector angle of 34° [31].

A cyclotron is a device used to accelerate positively charged particles by using a magnetic field to focus or bend particles and an electric field to accelerate charged particles. The main characteristic of a cyclotron is that it uses a constant field and constant Radio Frequency (RF). The cyclotron accelerates charged particles by means of hollow metallic chambers which are called "dees". The dees have a D shape and are connected to an RF power source which provides an alternating electric field between the diametrical faces of the dees [30]. The dees lie between two electromagnets and are mounted inside a vacuum chamber. They are installed between the two poles of the magnets and are made up of copper. They serve as electrodes which accelerate ions in the gap separating the two. A voltage is applied to the dees to manipulate the movement of charged particles. If the right hand side dee is at a negative potential, then a positively charged particle is attracted to it and accelerated towards the dee gaining energy. There exists no electric field inside the hollow part of the dees and in that region only a magnetic field acts on the charged particle.

The charged particle moves in a circular path with a corresponding radius r and returns to the diametrical gap where it is under the influence of an electric field. At this point the polarities of the dees are reversed so that the right hand side dee is now positive and the left is being negative. The particle is then accelerated towards the left hand side dee traversing a semi-circular path. This process is repeated until the particle gains the required energy for a particular experiment. The main advantage of circular accelerators over linear accelerators is that charged particles can pass the acceleration gap many times. This enables the charged particles to acquire more kinetic energy within a shorter time and with a relatively low gap voltage as opposed to that of linear accelerators.

3.4.1 AFRODITE (African Omni-purpose Detector for Innovative Techniques)

The photons emitted from the fusion reaction were detected using the AFRODITE spectrometer. It is a medium sized array detector that is able to measure high and low energy photons with good energy resolution, better than 3 keV at 1.33 MeV (see Figure 3.8). The AFRODITE array consists of two types of HPGe (High Purity Germanium) detectors namely the LEPS (Low Energy Photon Spectrometer) and clover detectors. However the current experiment was conducted using only the clover detectors. The AFRODITE spectrometer had 9 clover detectors in this experiment.

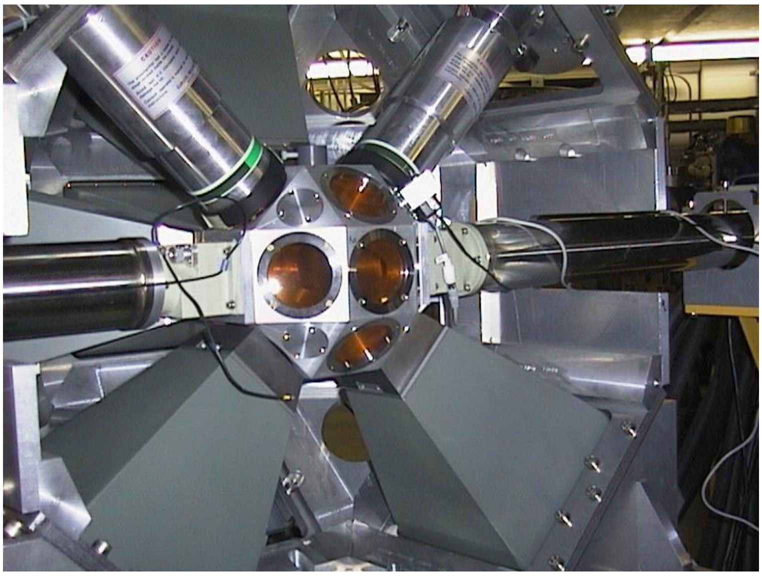

Figure 3.8: AFRODITE array showing some of the LEPS and Clover detectors surrounded by BGOs.

The detectors are mounted on an aluminium frame that has 18 detector positions (18 square and 8 triangular facets)[33]. The detectors are mounted around the target chamber in order to maximize the solid angle subtended at the target. The target chamber houses the target ladder that is used to mount targets. The target ladder can mount a maximum of three targets. In order to select a specific target position, the ladder can remotely be moved vertically. In the present study mounted on the target ladder was a Sm target used for reaction of interest, an empty slot for the background check, and a ruby which was used for focusing the beam. The clover detectors are surrounded by BGO (Bismuth Germanate) shields to factor out Compton scattered events.

3.4.2 Clover Detectors

A clover detector consists of four intrinsic 50×70 mm HPGe crystals closely packed with an arrangement similar to a clover leaf. Once the fusion evaporation reaction occurs, the radiation emitted interacts with the germanium crystals thus exciting the electrons from the valence band into the conduction band. This leaves a hole in the valence band creating an electron-hole pair. The charge produced is collected through reverse biasing the germanium crystal where a positive voltage is applied across the crystal. A gamma-ray may deposit all its energy into one Ge crystal through the process of photoelectric absorption. In Compton scattering the gamma-ray will interact with one crystal and scatter into another adjacent neighbouring crystal thus depositing the remaining energy into the crystal. In this situation an addback is performed whereby charge is collected from both crystals, added and thereafter used to compute the energy of the incident gamma-ray. Each germanium crystal has a pre-amplifier which serves to allow gamma-rays detected by more than one element of the clovers to be added in the addback process.

The Ge crystals have a small band gap of 0.7 eV and because of this it is easy at room temperature to thermally excite electrons across the band gap. The thermal excitation of electrons contributes a leakage current which degrades the energy resolution of the detectors. In order to reduce the noise associated with the leakage current the clover detectors have to be operated at low temperatures ($\sim$ 77 K) by constantly applying liquid nitrogen. The detectors are also housed in a vacuum tight cryostat to further maintain the low temperatures.

3.4.3 BGO (Bismuth Germanate Shields) detector

The BGO shields are scintillator detectors and they are usually placed around the clover detectors to detect the Compton scattered events. Figure 3.9 shows a BGO detector surrounding a clover detector.

The electrons produced by the gamma-rays interact with the BGOs causing them to scintillate. The light flash is detected by a photomultiplier that provides the detector signal. In the photomultiplier electrons are attracted towards a cathode which is a photosensitive surface. The electrons strike the cathode causing it to release photo-electrons. The photoelectrons are then accelerated and multiplied by a series of electrodes called the dynodes. Each dynode is at a higher potential than the previous and causing the electrons to be multiplied every time they hit the subsequent dynode. These electrons arriving at the anode at the final stage form the signal.

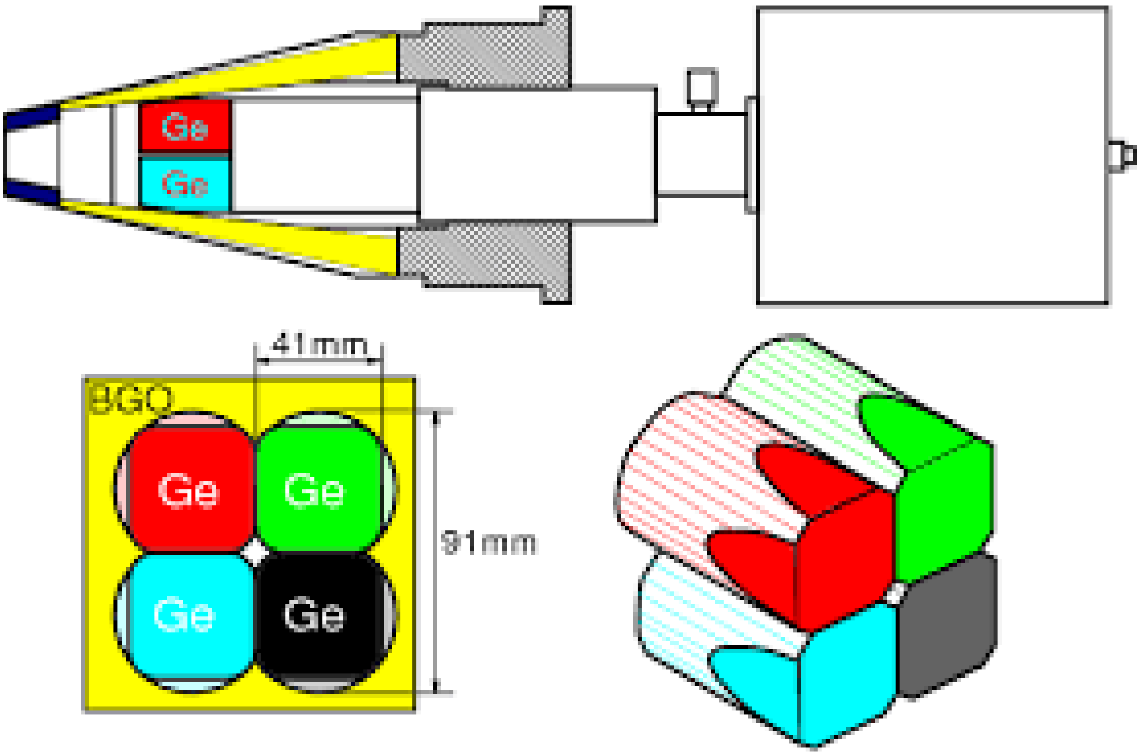

Figure 3.9: Typical assembly of BGO scintillator shield (in yellow) surrounding the clover detectors [22].

3.5 Data Analysis Techniques

3.5.1 Introduction

Data was collected and stored on hard drives. A total of approximately 10^9 gamma-gamma coincidence events were accumulated for the AFRODITE experiment. The MTSort software package from MIDAS (Multi Instance Data Acquisition System) generates spectra from data collected from the AFRODITE array. The MIDAS software is a user oriented digital interface system for data acquisition and experiment control [20]. Functions performed by MIDAS during the running of an experiment are based on the commands contained in an online C++ based sorting code.

The data collected by the MIDAS software has to be further sorted and converted into a format compatible with RADWARE. The RADWARE package developed by David Radford [21] is a gamma analysis package. It can be used to perform energy and efficiency calibration, generate spectra from clovers, construct and analyze gamma-gamma coincidence matrices through which the level scheme for the nucleus of interest is created. It consists of various programs including GF3 which is a least squares peak-fitting program used for analyzing spectra from the detectors. It also contains ESCL8R ("escalator") which is used mainly for analysing matrices and construction of a level scheme.

3.5.2 Energy Calibration

The data stored in the hard drives consists of energy measurements in ADC (Analogue Digital Converter) channels. However we are interested in obtaining the actual gamma-ray energies detected by the clovers. It is therefore necessary to convert the ADC channels to energy in units of keV. This is done by performing an energy calibration. The energy calibration has to be done for the gamma-ray energies of interest, in this case the range $\sim$ 100 keV to $\sim$ 2 MeV. The ^{152}Eu radioactive source was used to calibrate energies in this region. An energy calibration (.cal) file for the data can be obtained using the RADWARE program ENCAL. It performs a calibration by using a linear, quadratic or higher order polynomial fit represented by the equation:

$$E = a_0 + a_1 x + a_2 x^2 \tag{3.7}$$

where:
E- Energy of gamma-ray detected by the clover detector
a_0 - represents the offset in keV and is the intercept on the energy axis
a_1 - is the dispersion keV/Channel which represents rate in change of energy with change in channel number
a_2 - represents non-linearity

ENCAL has the option of performing an auto-calibration using the command (ca) which provides a more accurate calibration. It requires a source (.sou) file containing energies and intensities of gamma-rays produced by the calibration source ^{152}Eu.

3.5.3 Efficiency Calibration

It is necessary to perform an efficiency calibration because the detector efficiency is dependent on the energy of the gamma-rays detected. It is therefore needed for the proper analysis of the data. Detector efficiency is usually determined by measuring the count rates from a known gamma-ray source such as ^{152}Eu. The information describing the efficiency is represented in an efficiency curve relating the efficiency value to the gamma-ray energy. The

RADWARE program EFFIT was used in plotting a relative efficiency curve, which was stored in a (.aef) file and is shown in Figure 3.10.

The curve gives the summed relative peak efficiency as a function of gamma-ray energy for the detectors [35]. In order to use the program one needs a Source Input (.sin) file and Source (.sou) file. The .sou files are data files kept in RADWARE and store energies and relative efficiencies for different radioactive sources. The EFFIT program uses different parametrization for low and high energies:

Efficiency at low energies:

$$lnEff = A + Bln\frac{E_\gamma}{E_1} + C(ln\frac{E_\gamma}{E_1})^2 \tag{3.8}$$

Efficiency at high energies:

$$lnEff = D + Eln\frac{E_\gamma}{E_2} + F(ln\frac{E_\gamma}{E_2})^2 \tag{3.9}$$

The constants E_1 and E_2 are of values 100 keV and 1 MeV respectively. The parameters A, B and C represent the efficiency at low energies while D, C and F at high energies. The combined efficiency function is therefore:

$$Eff = exp(A + Bx + Cx^2)^{-G} + (D + Ey + Fy^2)^{-G})^{\frac{-1}{G}} \tag{3.10}$$

where:

G - is the interaction parameter between low efficiency and high efficiency. The variables x and y are defined as follows:

$$x = ln\frac{E_\gamma}{E_1} \tag{3.11}$$

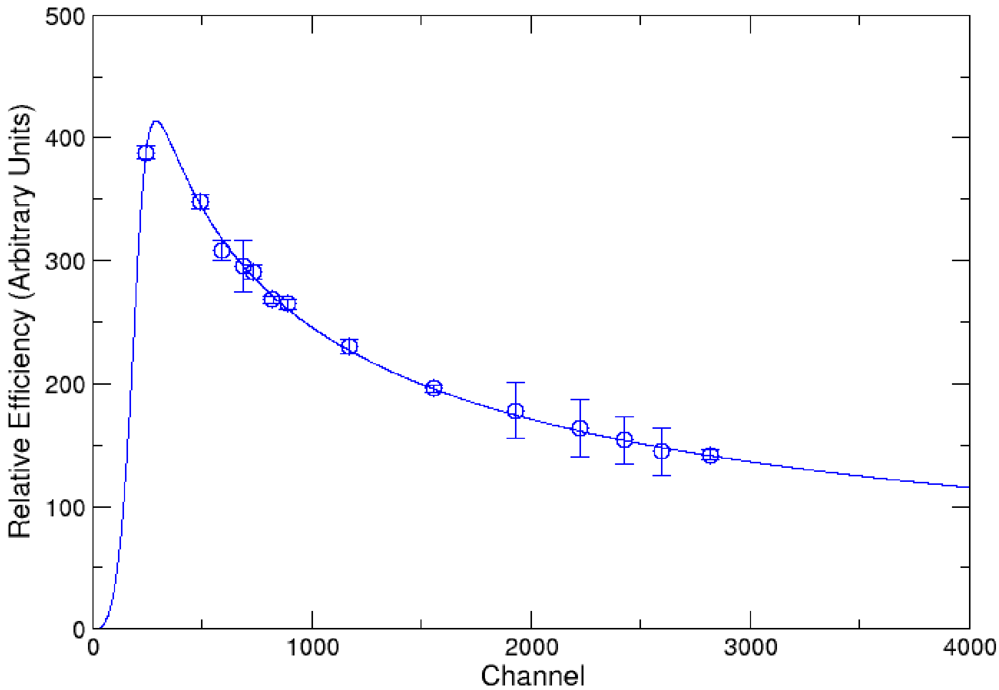

Figure 3.10: Plotted curve for the relative efficiency of Ge using energies emitted by a ^{152}Eu source. The efficiency reaches a maximum for lower energy gamma-rays in the range 70−400 keV. This is evident in the projection spectrum as these gamma-rays have higher intensities.

$$y = ln\frac{E_\gamma}{E_2} \tag{3.12}$$

3.6 Analysis of $\gamma\gamma$ coincidences

During the data sorting process it is necessary to gain match the detectors. This is a process of ensuring that peaks corresponding to a specific energy are at the same position for all detectors. This is done by using the gain coefficients from the online C++ based sorting code and putting them in a linear function used to fit energy peaks. The process is repeated until the energies correspond to literature values for both the calibration source and inbeam data.

3.6.1 The Matrix

Once the data is gain matched the sorting code generates four RADWARE compatible matrices, a random-subtracted symmetric matrix for building the level scheme, two asymmetric matrices for DCO measurements and one matrix for Polarization anisotropy measurements. The matrices store energies detected by the clovers in a two-dimensional histogram with 4096$\times$4096 channels. The random-subtracted symmetric matrix contains prompt gamma-gamma coincidences. The DCO matrix is restricted to containing gamma-gamma coincidences between detectors at different angles in the beam line. In this case it is the 90° clovers (one axis) and 135° clovers on the other axis. The DCO matrix is used to assign spins to nuclear states. The remaining matrices are used in polarization measurements which gives information about the electric or magnetic nature of the gamma-rays connecting nuclear states.

Gating is the process of applying or selecting a narrow window to define a specific decay path or transition. It is important in constructing a level scheme where multiple gates are examined to obtain more explicit information about the order of transitions. The process of gating however does not assign spin, parities and multipolarities to nuclear states hence DCO ratios, polarization measurements and angular distributions are performed. The width of a gate is determined by the equation:

$$FWHM = \sqrt{f^2 + (g^2 \times E_\gamma)} \tag{3.13}$$

where E_γ= gamma-ray energy

f- Represents factors independent of the gamma-ray energy, for example noise

y- Represents statistical fluctuations of electron-hole pairs in the clovers for a certain energy E_γ

In the coincidence spectra produced from gating, the peaks corresponding to discrete transitions will appear on top of a continuum background. The background is due to escape photoelectrons from the clovers, Compton scattering of photons into the detector and unresolved weak transitions. It is important to factor out background to obtain better quality spectra. This can be done either manually or automatically in RADWARE using ESCL8R . However it is more suitable to manually set limits for the background in cases where the spectra is a complicated as in the case of an odd proton nucleus, to avoid over-subtraction of background. Gating to obtain coincidence spectra also helps to reduce background significantly as it shows only transitions in a particular decay path.

3.6.2 Construction of Level Scheme

A singles spectrum is obtained from using the gamma-rays detected by one detector. Coincidence spectra obtained from using events recorded by at least two detectors were used in constructing a level scheme. The coincidence relations between transitions are deduced by applying a software gate on a certain energy to show only a specific decay path. The gamma-rays that are regarded to be in coincidence are those that are detected almost simultaneously by the clover detectors arriving within a certain time interval called the coincidence time window.

Examining multiple gates from gamma-rays enables one to obtain the position of the excited nuclear states in a level scheme. The intensities of the gamma-rays are also useful in showing which gamma-rays precede each other. The timespec for this data is shown in Figure 3.11, the “good” events occur in the gate $982-1016$ ns. These are the events with minimum randoms and arrive within the coincidence time window.

To schematically illustrate the use of coincidence principles to construct a level scheme, Figure 3.12 shows a partial level scheme constructed from examining multiple gates. The lower levels within the same band are fed from entry channels that are higher in excitation energy and because of this feeding they tend to have higher intensities (thicker arrow. Furthermore the energy levels lower in excitation energies usually appear with high intensities in the spectra because this is the region of high efficiency for the Ge detectors. A gate on E_3 should produce a spectrum with energy peaks corresponding to the transitions E_2, E_1 and E_{10} to E_{12}.

The intensity of an energy peak on a gated spectrum should reveal information about how close it is to a particular transition in a level scheme. For instance if a gate is placed on E_3 then the gated spectra should show E_2, E_1

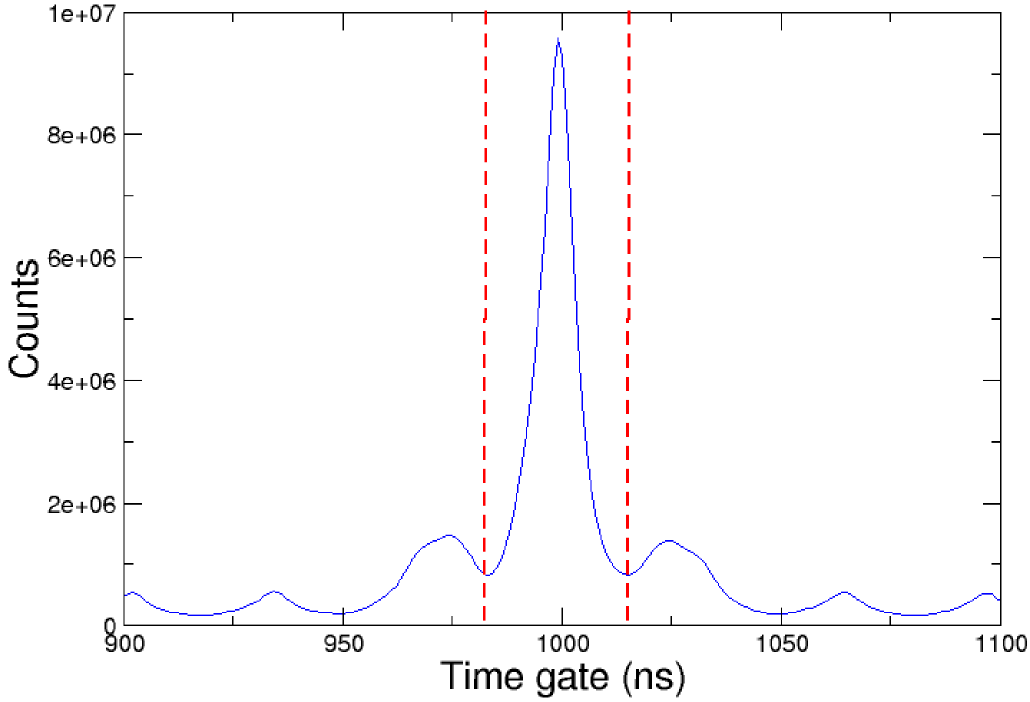

Figure 3.11: A time (x-axis) spectrum for coincidences between two gamma-ray detectors obtained for the data collected in the experiment. The "good" events occur in the gate $982 - 1016$ ns.

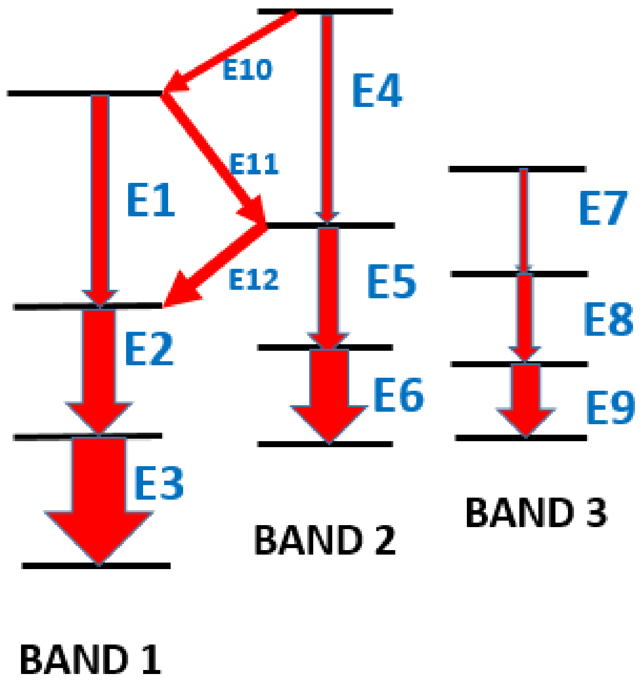

Figure 3.12: Partial level scheme illustrating the coincidence concept in constructing a decay path.

and E_{12} energy peaks with highest amplitude corresponding to high intensities. The closer an observed transition is to the gated transition in the same decay path, the higher its intensity in the resulting projected spectrum. If a gamma-ray belonging to the same nucleus does not appear in a coincidence spectra then it means it is parallel to the gated transition. An example of this is considering the transition E_3 in band 1 which is parallel to E_7 in band 3 because there is no transition that connects the two bands. The in-band transitions are usually E2 in nature with the out of band transitions usually being M1s.

There are a number of assumptions made when constructing a level scheme. The first assumption was that all levels belonging to the same band should have the same parity. Another assumption was that the examination of multiple gates from gamma-rays enables one to obtain the position of the excited nuclear states in a level scheme. The intensities of the gamma-rays are also useful in showing which gamma-rays precede each other. The spin values of levels increases monotonically with increasing energy for all bands. Furthermore it was assumed that the population (intensity) of a level increases with decreasing excitation energy due to feeding from entry channels higher in excitation energy.

3.6.3 Angular Correlations

After the construction of a level scheme using coincidence spectra, the spin and parity assignment of the excited nuclear states can be confirmed by measuring the angular distributions of the gamma-ray transitions. The multipole order of the gamma radiation can also be inferred by measuring the angular distribution and polarisation of the gamma-rays. In a fusion reaction the angular momentum vector l×b is approximately perpendicular to the beam direction. The states produced will be aligned to the reaction planes as shown in Figure 3.13 and will have an anisotropic distribution.

It is important to observe an anisotropic distribution because it helps to distinguish gamma radiation of different multiple orders. The ability to observe an anisotropic distribution measurement entirely relies on the ability to obtain a non-uniform population of magnetic sub-states. Mathematically the sub-states are described using analytical functions such as the Legendre polynomials which are widely used. The general formula used for the angular correlation function that relates the intensity of the gamma radiation to the direction θ it is produced in, is given by:

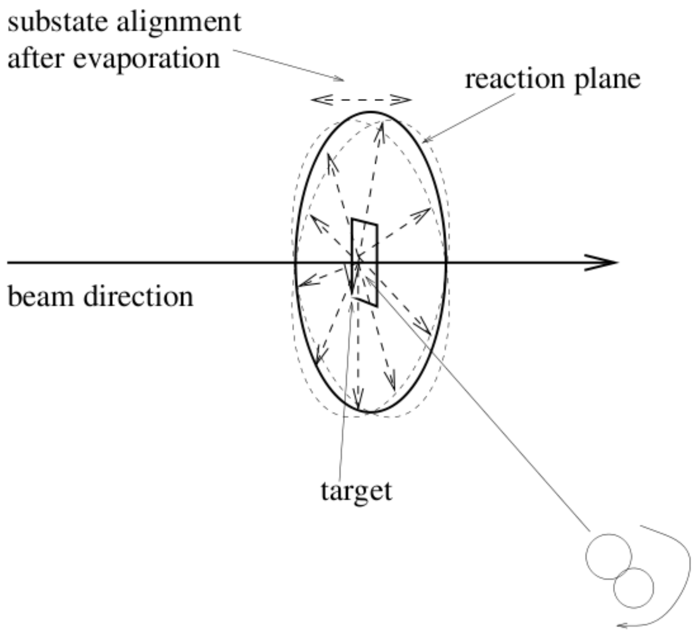

Figure 3.13: In order to observe an anisotropic distribution the states populated have to be aligned to the reaction plane [23].

$$W(\theta) = \Sigma A_{2l} P_{2l}(cos\theta)d\Omega \tag{3.14}$$

where W(θ) is the intensity of the gamma radiation, θ is the angle between the successive gamma-rays, dΩ is the solid angle in which the gamma-ray is emitted in, A_{2l} are the correlation coefficients depending on only the angular momentum of the subsequent radiation and P_{2l} are the even Legendre polynomials. The gamma radiation is emitted with different intensities in different directions depending on the multipole order, yielding the anisotropic distribution.

In this experiment we were considering only the lower order terms in the expansion corresponding to transitions. These are mainly the transitions that carry angular momentum not greater than two units (i.e. E1, M1 and E2). If the angular correlation function is expanded considering only the terms up to l= 2, then a power series is formed in even powers of cos(θ) as follows:

$$W(\theta) = (1 + A_0(cos^2\theta) + A_2(cos^4\theta))d\Omega \tag{3.15}$$

An anisotropy is then obtained by taking the ratio of the angular distribution at two angles θ_1 and θ_2. If the data collected contain a large number of excited states from different nuclei as is the case of this experiment, then one cannot solely rely on angular distribution measurements, because they are only useful in the case of a finite number of excited states produced by a single nucleus.

3.6.4 The DCO (Directional Correlation of Oriented states) measurements

The DCO measurements can be used to factor out the limitation posed by angular distributions. The measurements are obtained by using coincidence spectra which reduce the background significantly. Two gamma-rays are chosen, one which is the gamma-ray (γ_1) of interest and γ_2 being the one in coincidence with γ_1. A minimum of two detectors that can record the events γ_1 and γ_2 are needed. A software gate is applied on γ_1 with reference to a chosen axis (e.g. y-axis). The coincidence spectra obtained from the gate on γ_1 is projected on the other axis which will be the x-axis if the gate was placed on the y-axis. The procedure is repeated with the axis reversed where the x-axis is now chosen for placing the gate and the y-axis used for the projection. The ratio of the counts in the coincidence spectra for a given transition and angles θ_1 and θ_2 is recorded. This is called the DCO ratio, given by:

$$DCO = \frac{I(\gamma_1, \theta_1; \gamma_2, \theta_2)}{I(\gamma_1, \theta_2; \gamma_2, \theta_1)} \tag{3.16}$$

The uncertainties in the DCO measurements were computed as follows:

$$\Delta DCO = DCO_{ratio}\sqrt{(\frac{\Delta I(135°, 90°)}{I(135°, 90°)})^2 + (\frac{\Delta I(90°, 135°)}{I(90°, 135°)})^2} \tag{3.17}$$

where:

$\Delta I(135°, 90°)$ and $\Delta I(90°, 135°)$ refer to the uncertainties in the numerator and denominator respectively.

The angles θ_1 and θ_2 for this experiment were 135° and 90° respectively with 4 clovers at 135° and 90° respectively. Equation 3.16 represents the

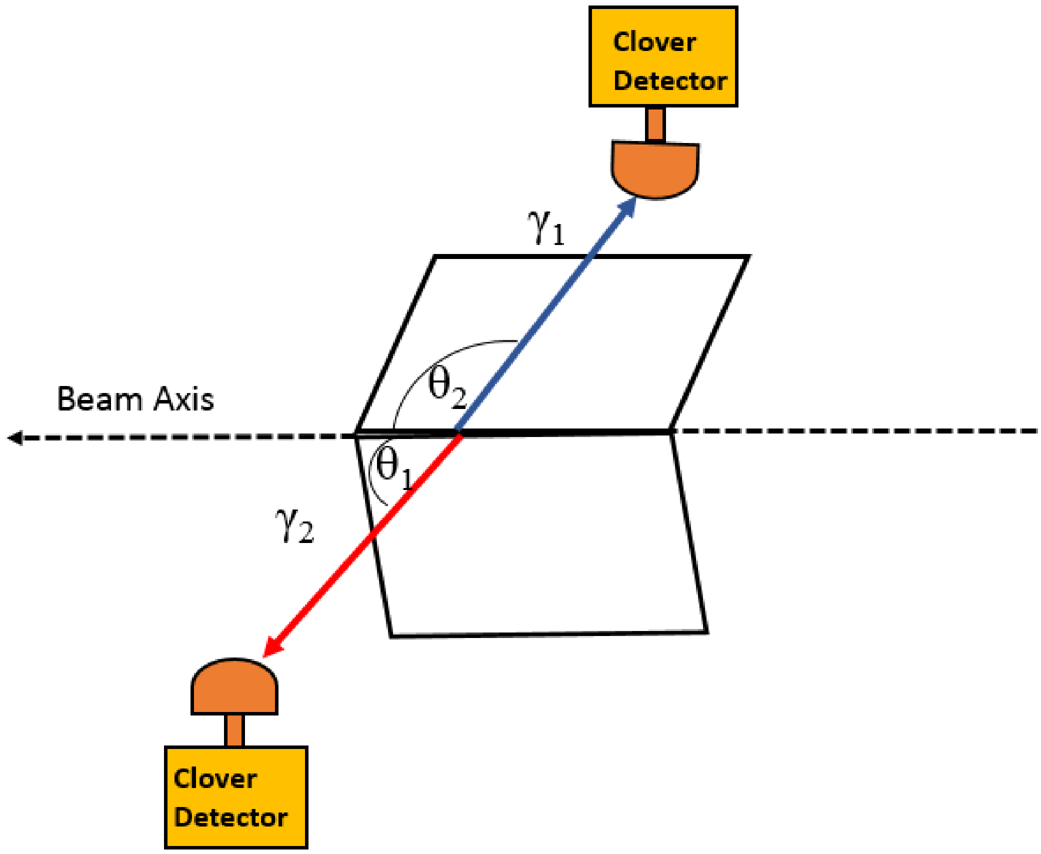

Figure 3.14: A typical arrangement for the detectors showing the two different angles where the detectors are placed to allow the events to be recorded in an angle dependent asymmetric matrix which is used in computing the DCO ratios.

ratio of the intensity of γ_1 at θ_1 in a spectra gated with γ_2 at θ_2, to the intensity of γ_1 at θ_2 and the gate applied at using γ_2 at θ_1. A pure stretched quadrupole transition has a value of ~ 1 while a pure dipole has a value around 0.5. However, it should be noted that the arrangement of the array could affect the average value expected for a typical dipole or quadrupole. The type of gate applied (i.e using an E2 or M1 transition) will also affect the ratio. If the gate is applied on a pure dipole the values expected for dipole and quadrupole transitions are ~ 1.1 and ~ 1.8 respectively.

3.6.5 Polarization measurements

If the magnetic and electric transitions have the same multipole order then the angular distribution will be identical. This is because the angular correlation coefficients depend only on the multipole order of the transition. To distinguish between electric and magnetic transitions of the same multipole order polarization measurements are performed. The Ge crystals can be arranged such that they can allow electric and magnetic transitions to scatter in different directions as shown in Figure 3.15. Transitions having the same multipole order will differ in parity and hence in their orientation with respect to the polarization plane when they scatter. The emitted radiation following a fusion reaction has a vector $\overrightarrow{r}$ related to the radiation propagation. The plane of polarization if formed by $\overrightarrow{r}$ and $\overrightarrow{E}$ (electric field produced by the radiation).

The experimental linear polarization measurements were determined by the formula:

$$A_p = \frac{aN_v - N_h}{aN_v + N_h} \tag{3.18}$$

where the constant a is defined as $\frac{N_h}{N_v}$

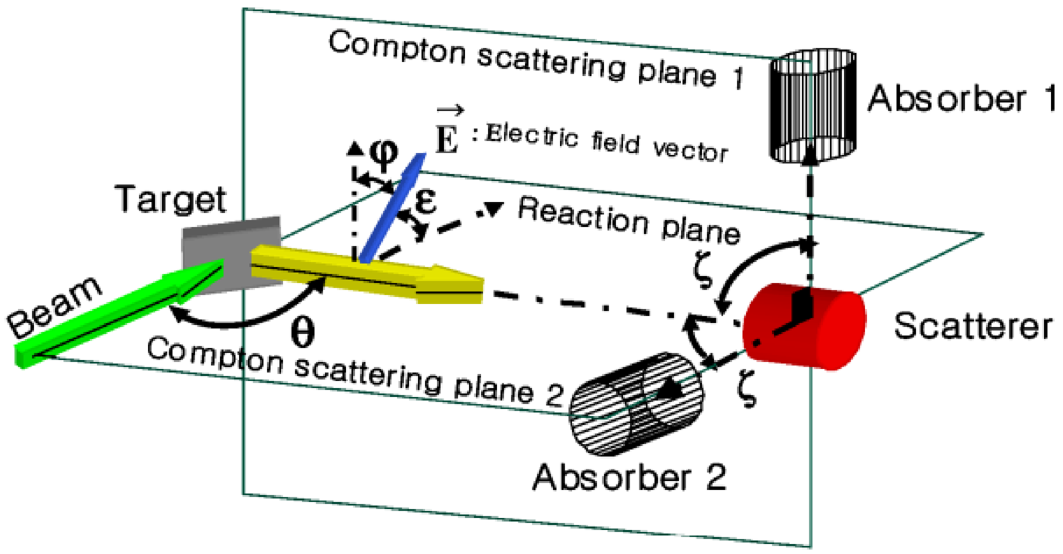

Figure 3.15: Ge crystals can be used as a scatterer and absorber where in Compton scattering gamma-rays scattered perpendicular to the direction of the electric field will most likely propagate in a vertical direction [34].

and is obtained using an unpolarized event. The value obtained for "a" in this work was 0.94. The other two parameters are N_h and N_v where :

N_h - represents the counts in the horizontal plane (i.e the gamma-rays that are scattered parallel to the beam-detector plane)
N_v - represents the counts in the vertical plane which are the gamma-rays scattered perpendicular to the beam-detector plane.

The uncertainties in the linear polarization anisotropy measurements were computed as follows:

$$\Delta A_p = \frac{2}{(N_V + N_H)^2}\sqrt{(N_H\sigma_V)^2 + (N_V\sigma_H)^2} \tag{3.19}$$

where:
σ_V and σ_H refer to the errors in the gamma-rays scattered vertically and horizontally respectively.

In the case of the configuration of the HPGe crystals in a clover detector, two of the four crystals act as the scatterer while the two neighbouring crystals act as absorbers. An incident gamma-ray will scatter into one crystal and is then absorbed in the adjacent crystal. By measuring the relative intensities of the gamma-rays scattered parallel and perpendicular, a linear polarization measurement can be obtained.

Chapter 4

Experimental Results

The level scheme of ^{161}Tm is well known from the study of the nucleus at high spin two decades ago in previous work by Smith *et al.* [2], Foin *et al.* [37] and by Adam *et al.* [38] from the β decay of ^{161}Yb. A recent study of ^{161}Tm by Teal *et al.* [36] revealed some discrepancies particularly pertaining the ground state band based on the [404]$7/2^+$ proton configuration. Rotational bands were assigned [523]$7/2^-$, [404]$7/2^+$, [541]$1/2^-$, [402]$5/2^+$ and [411]$1/2^+$ Nilsson configurations from lifetime measurements in the previous work [37]. The level scheme built from this work is shown in Figure 4.1. Transitions in the level scheme were placed using intensity arguments and coincidence relationships from examining multiple gates.

There are DCO calculations performed from previous work by Maliage *et al.* [39] for the AFRODITE array. The values suggest that if a gate is placed on a stretched quadrupole transition then the $\mid \Delta I \mid= 2$ transitions are expected to have a value of ~ 1, while the $\mid \Delta I \mid= 1$ will have a value of ~ 0.6. The study performed indicated a strong dependence of the DCO value on the mixing ratio and this is represented in the plot in Figure 4.2. The DCO calculations obtained by Maliage *et al.* [39] have been used as a reference for

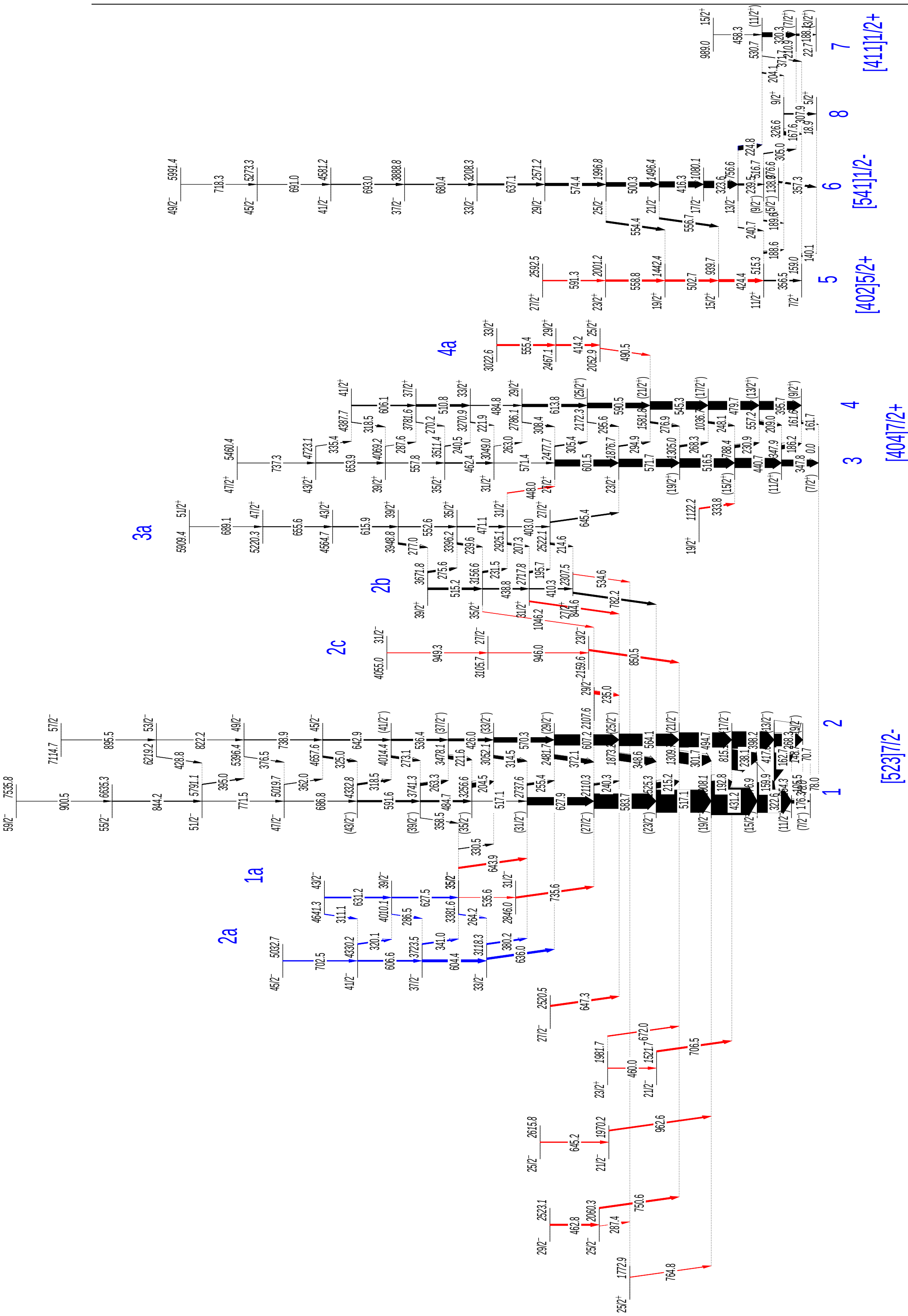

Figure 4.1: Level Scheme built in this work for ^{161}Tm. The new transitions are marked in red, the gamma-rays that have been re-arranged are in blue and all energy levels of the nuclear states are in units of keV.

comparison with values obtained in this work. In this study all the computed DCO values were obtained from gating on a known E2 transition (e.g see spectra in Figure 4.3). The deduced DCO ratios are presented in Figure 4.4. It is observed that the quadrupole transitions cluster around a value of ~ 1 and the dipole transitions around a value of ~ 0.6.

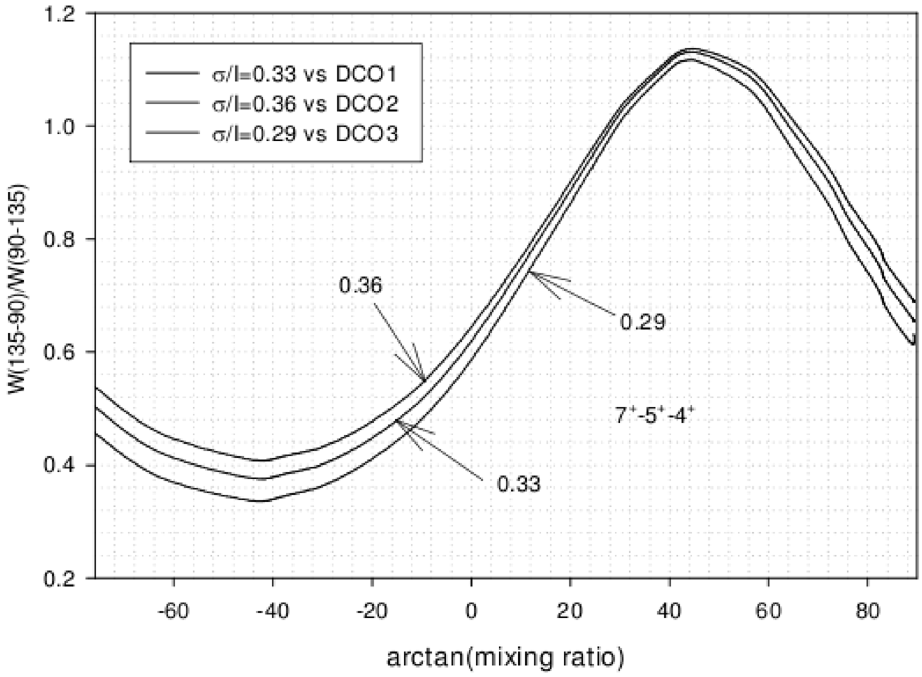

Figure 4.2: A plot illustrating the dependence of DCO ratios on the mixing ratio for the AFRODITE array in a previous study from [39].

In order to obtain the linear polarization anisotropy measurements, the vertical and horizontal coincidence spectra were used. However the quality of these spectra is poor due to low statistics (see Figure 4.5). It was observed that subtracting the horizontal spectra from the vertical spectra gave resulting negative counts for the magnetic transitions and positive counts for electric transitions. The results of the linear polarization anisotropy measure-

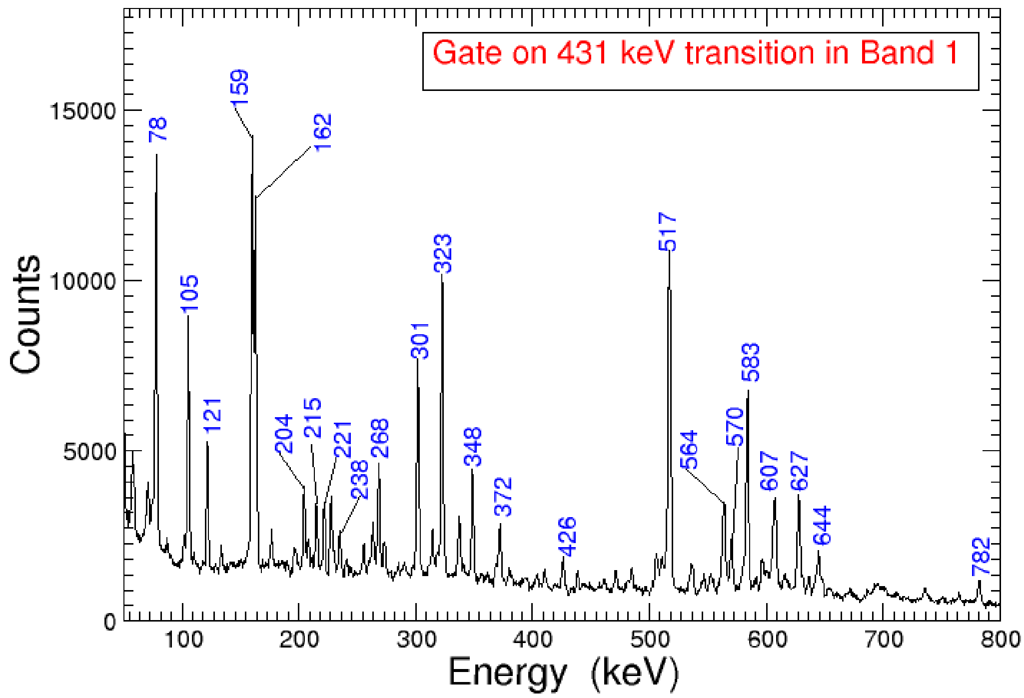

Figure 4.3: The spectrum used for DCO measurements representing events detected at 135° obtained from gating the angle dependent asymmetric matrix.

,

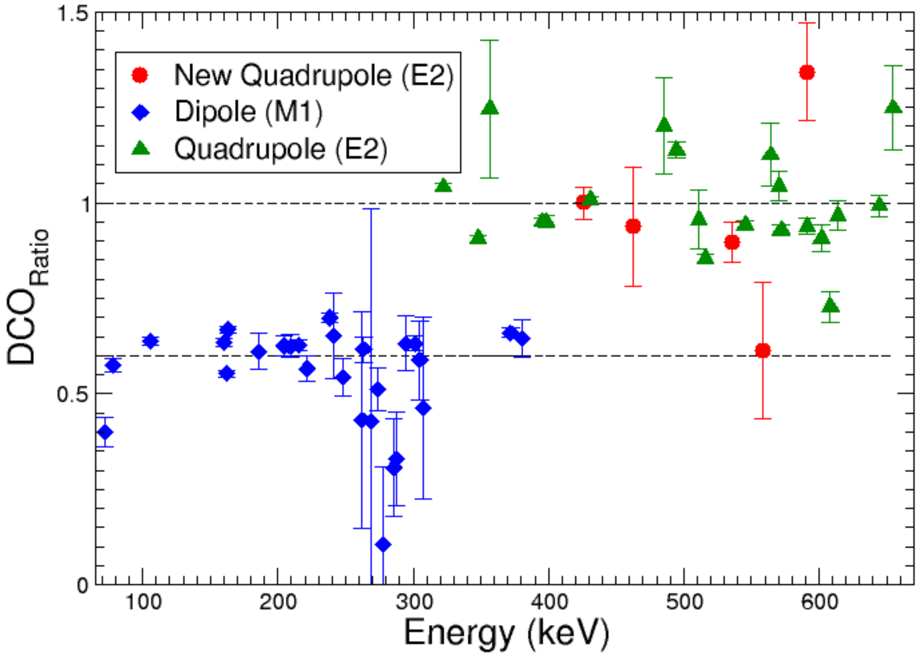

Figure 4.4: A plot representing the DCO ratios for the observed gamma-ray transitions. The dashed lines correspond to the average values expected for typical pure dipole and quadrupole stretched transitions gated on E2 transitions.

ments consistent with this observation are presented in Figure 4.6. It must be noted that the polarization anisotropy values obtained are independent of the type of gated spectrum used (i.e electric or magnetic). Together the linear polarization anisotropy and DCO measurements were used to determine or confirm the assignment of spins and parities where applicable.

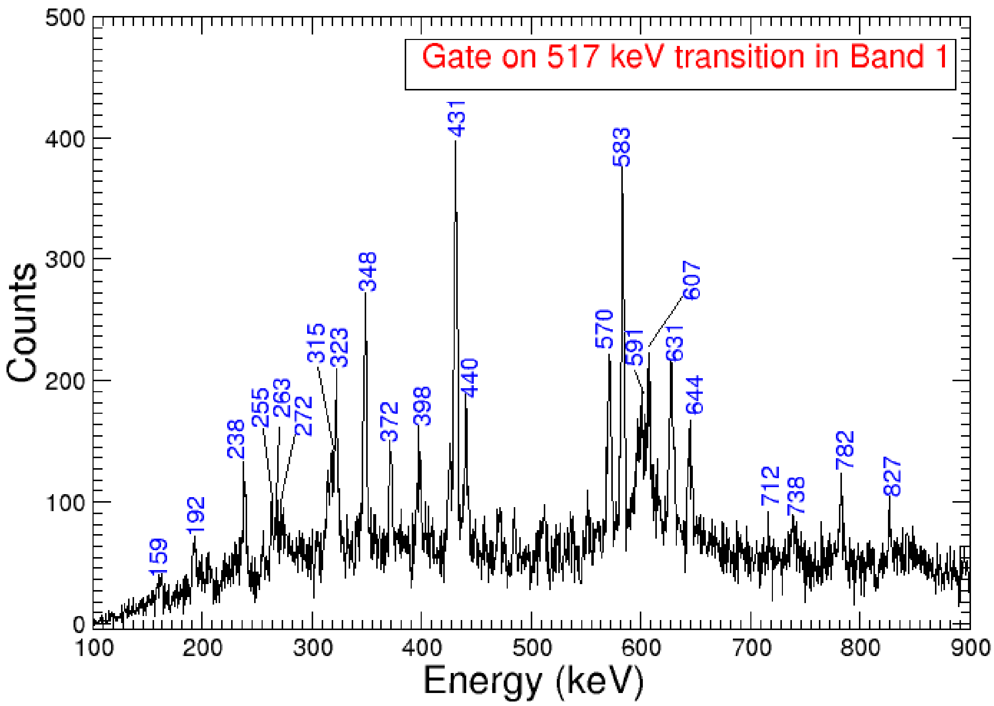

Figure 4.5: A spectrum used for the Polarization measurements. The polarization spectrum displays events detected only at an angle of 90° in coincidence with the 517 keV transition.

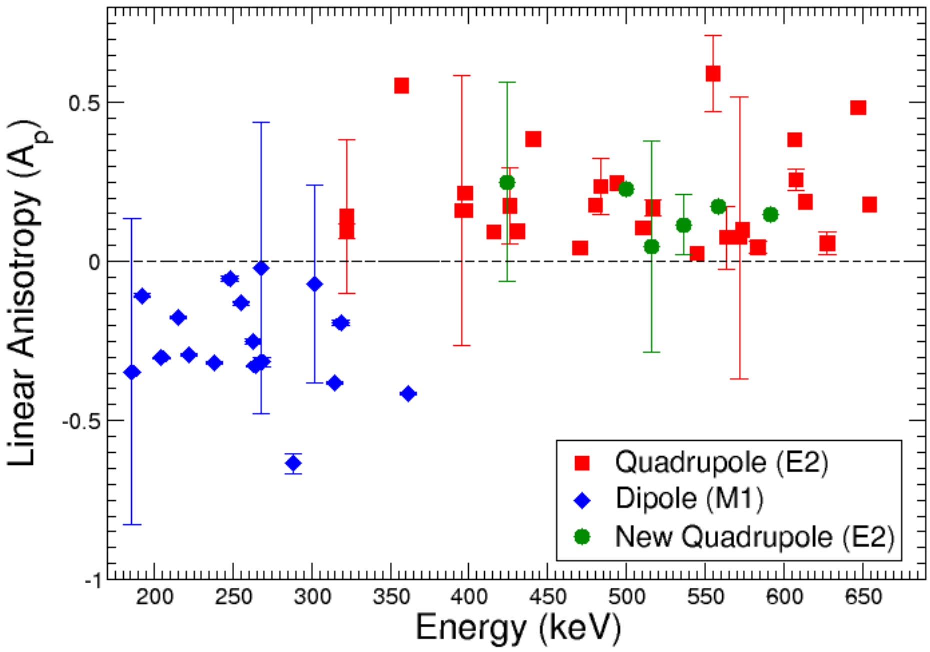

Figure 4.6: The linear polarization measurements obtained for this work. Negative values were obtained for the dipole M1 transitions and positive values for the E2 quadrupoles. It is observed that quite a number of transitions had a value near zero which is characteristic of a mixed transition.

4.1 The [523]$7/2^-$ Yrast band

Band 1 and Band 2

The two bands are observed as signature partner bands previously established with Band 1 as the $(-, -\frac{1}{2})$ signature and Band 2 as the $(-, +\frac{1}{2})$ signature of the [523]$7/2^-$ proton configuration. A spectrum gated on the 322 keV $(\frac{15}{2}^- \rightarrow \frac{11}{2}^-)$ transition is shown in Figure 4.7. It is observed that Band 1 is lower in energy at an excitation energy of 78 keV as expected, being the favored band. The two bands with both negative parity are connected by strong M1 transitions. The strong M1 transitions are due to the odd proton occupying the $h_{\frac{11}{2}}$ high-j intruder orbital associated with a high value for the magnetic moment.

In this study the nuclear states for Band 1 and Band 2 have been confirmed up to spin $\frac{59}{2}^-$ and $\frac{57}{2}^-$ respectively. A major challenge encountered was performing the DCO ratios and polarization measurements at spin above $\frac{43}{2}^-$ due to having to select a higher gate in energy and hence compromising statistics. Another difficulty was the presence of energy peaks being very close in energy to other peaks in a different band such that when a gate is applied, it will produce transitions corresponding to more than one band making it challenging to place transitions to specific bands. A good example of such peaks are the $(517, 516)$ keV as well as the $(570, 571)$ keV transitions. A representative spectrum of this nature is displayed in Figure 4.8

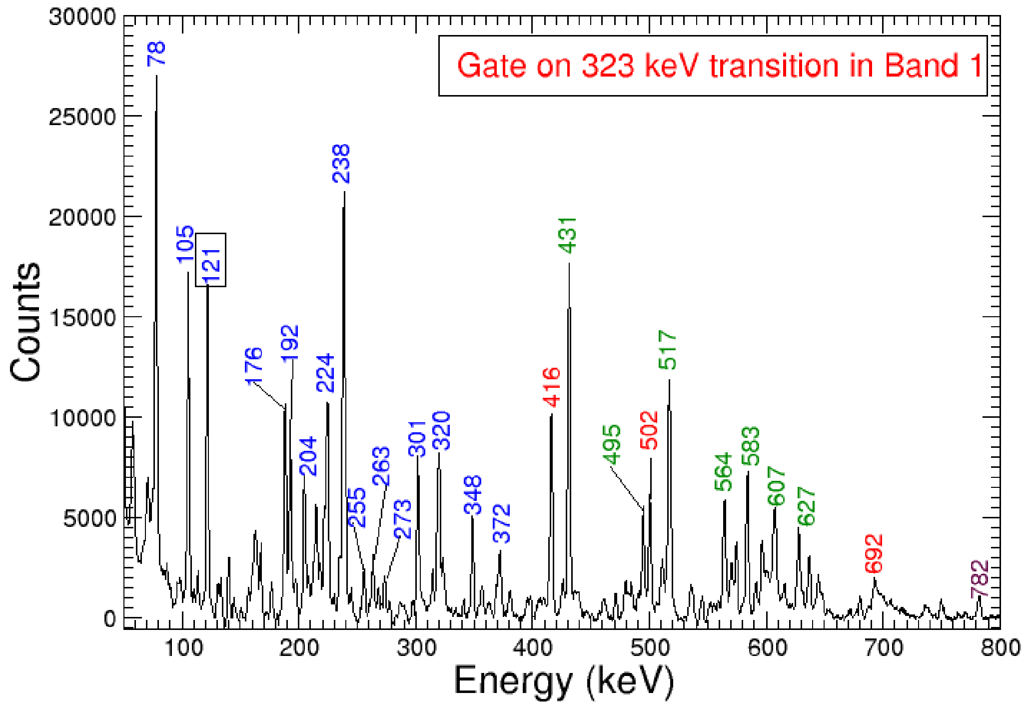

Figure 4.7: Spectrum corresponding to gate placed at the 322 keV E2 transition showing a representative rotational spectrum for the yrast states in Band 1. The transitions in blue are the in-band transitions, while the E2 transitions are in green, the gamma-rays in red belong to Band 6 which also has a 322 keV E2 transition and the 782 keV belongs to Band 2b.

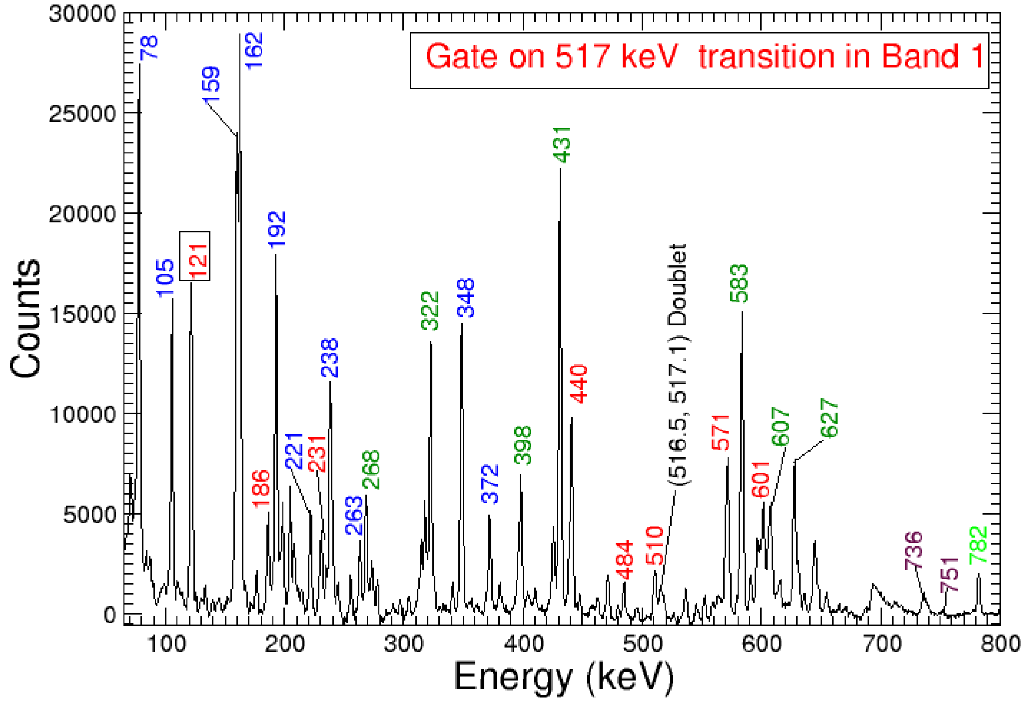

Figure 4.8: Spectrum illustrating the results from gating on a transition that is close in energy to another. In this case a gate applied on 517 keV in Band 1 is close to the 516 keV in Band 3. As a result some transitions (in red) are observed belonging to Band 3, the M1s in Band 1 are in blue, the E2s in green, the new transitions 736 keV and 751 keV are in purple, the 782 keV from Band 2b in light green. The 121 keV transition is a contaminant and appears in all spectra irregardless of the gate applied.

4.2 The Ground state Band

Band 3 and Band 4

Band 3 and 4 were initially assigned as the $[404]7/2^{+}$ intrinsic state by Adam *et al.* [38] using an atomic beam technique and further confirmed by Smith *et al.* [2]. As mentioned earlier the recent study of ^{161}Tm by Teal *et al.* [36] has made significant changes more especially above spin $\frac{31}{2}^{+}$. In fact Teal [36] placed transitions that showed the backbending phenomena initially not observed by Adam *et al.* [38] and Foin *et al.* [37]. In this work bands 3 and 4 have been built up to spin $\frac{47}{2}^{+}$ and $\frac{41}{2}^{+}$ respectively, with the DCO and polarization measurements confirming the states shown in Appendix B. The rotational spectra representing the transitions in Band 3 and 4 are shown in Figure 4.9 and 4.10 with the gate at 440 keV and 480 keV respectively. Band 3 and 4 have been built consistent with Teal *et al.*, [36].

Band 5

Band 5 is a rotational band built on the $[402]5/2^{+}$ configuration. The previous studies on ^{161}Tm by Foin *et al.*, [37] had only reported one transition, connecting the $\frac{5}{2}^{+} \rightarrow \frac{9}{2}^{+}$ levels of this band. In the current study this band has been extended significantly to spin $\frac{27}{2}^{+}$ by transitions marked in red for Band 5, shown in the level scheme built in this work.

The new transitions were confirmed by DCO ratios and linear polarization measurements. Band 5 is fed by E1 transitions from the $[541]1/2^{-}$ band and connected to Band 8 by M1 transitions. Figure 4.11 displays the spectrum associated with transitions in this band.

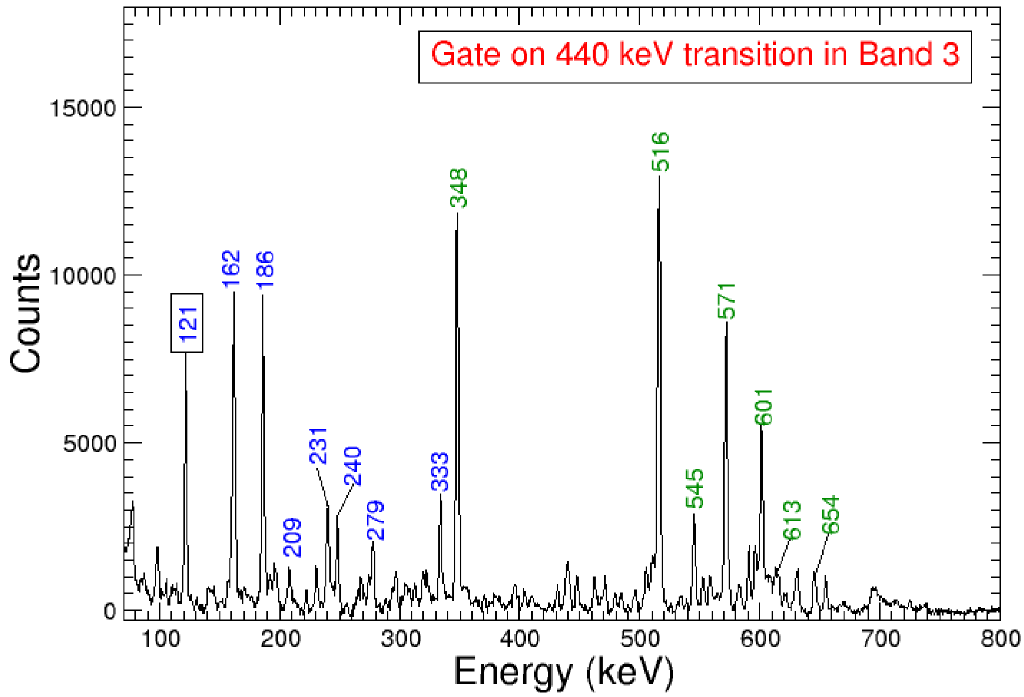

Figure 4.9: Spectrum corresponding to gate at the 440 keV E2 transition showing a representative rotational spectrum for the states in Band 3. The gamma-rays in green are E2s, the gamma-rays denoted in blue are M1s and the contaminant gamma-ray 121 keV showing up in every spectrum is encased in a black rectangle.

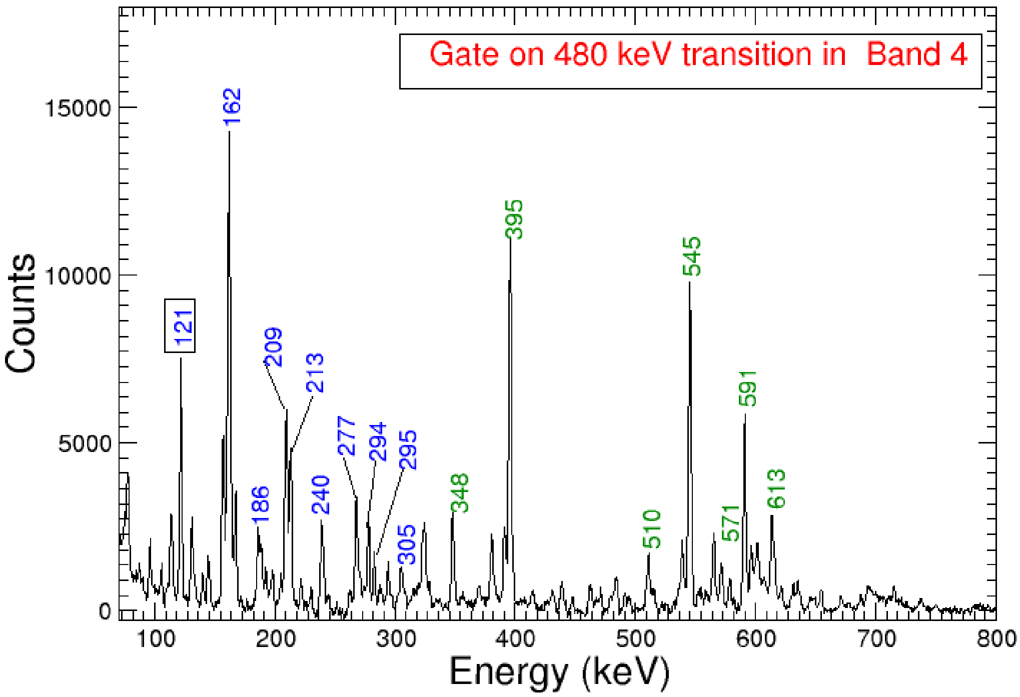

Figure 4.10: Spectrum corresponding to gate at the 480 keV E2 transition showing a representative rotational spectrum for the states in Band 4. The gamma-rays in green are E2s, the gamma-rays denoted in blue are M1s and the contaminant gamma-ray 121 keV showing up in every spectrum is encased in a black rectangle.

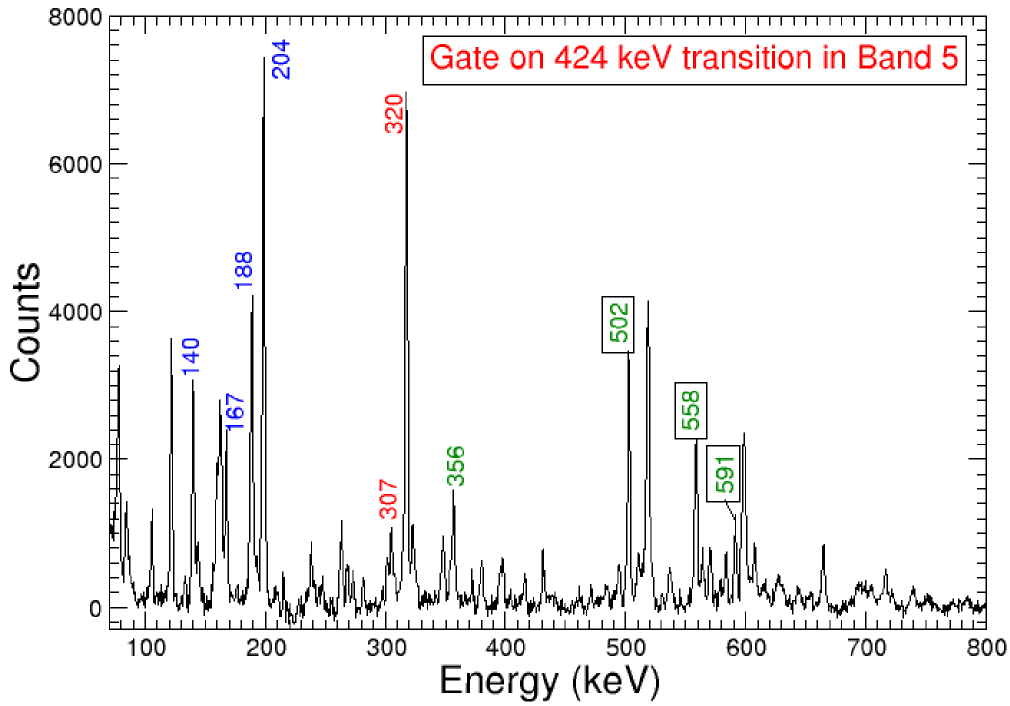

Figure 4.11: A rotational spectrum for a gate applied at the 424 keV transition showing the new E2 transitions above the 356 keV (encased in black boxes) transition which are labeled in green, while the 140 keV, 204 keV, 167 keV and 188 keV M1s in blue are in coincidence with the 424 keV transition. The transitions in red are E2s in coincidence with the 424 keV transition but not belonging to Band 5.

Bands 6, 7 and 8

Band 6 is the $[541]1/2^-$ configuration and decays through E1 transitions to Band 7 and 5 which respectively correspond to the $[411]1/2^+$ and $[402]5/2^+$ configurations. In Band 6, the 554 keV and 557 keV transitions have $\mid \Delta I \mid = 3$ which is highly unlikely. However when gating on the 424 keV and 502 keV new transitions together with the 356 keV the two transitions appear in the coincidence spectra (see Figure 4.12). We propose that the large $\mid \Delta I \mid = 3$ could then be due to a wrong assignment of spin at the bandhead of Band 6 affecting the spins of the states above it. Therefore the assigned Nilsson configuration to Band 6 could possibly be incorrect. Furthermore in [43] there are a couple of unresolved gamma-rays observed at low spin feeding Band 6 shown in Figure 4.13 and need further investigation as they could contribute to the spin assignments of the band at low spin.

A comprehensive analysis of both bands was not feasible because the states were weakly populated yielding poorer statistics and also due to some transitions being close in energy, such as $(240, 239)$ keV and $(188, 189)$ keV. The results presented by Foin *et al.* [37] proposed one particle excitations at 7.3 keV, 337.4 keV and 367.2 keV, corresponding to Nilsson orbitals $[411]1/2^+$, $[411]3/2^+$ and $[541]1/2^-$ respectively. There is a $\mid \Delta K \mid = 2$ forbidden transition observed from $[541]1/2^-$ to the $[402]5/2^+$ corresponding to a 240 keV transition and other $\mid \Delta K \mid = 2$ transitions which are 204 keV and 372 keV to the low lying intrinsic states. A spectrum that is obtained by gating on the 500 keV transition in Band 6 is shown in Figure 4.14 with the gamma-rays in blue representing out of band transitions connecting Band 6, Band 5 and Band 8. The gamma-rays in red are in coincidence with the 500 keV transition but belong to Band 8 and Band 7 while the gamma-rays in green are in the same band with the 500 keV transition. The 557 keV

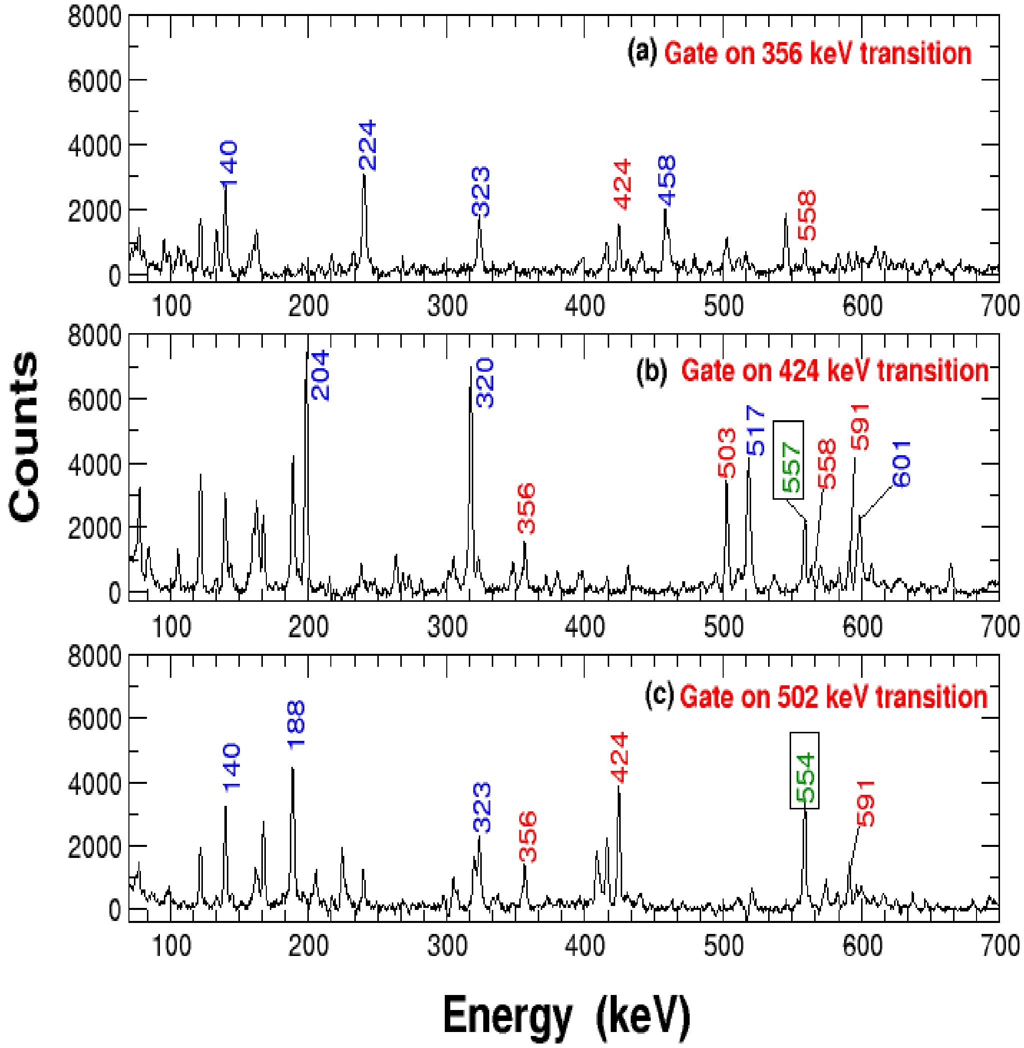

Figure 4.12: An illustration of the multiple gates examined for transitions in Band 5 that are in coincidence with the $|\Delta I| = 3$ the 554 keV and 557 keV transitions. The spectra were also used to place the new transitions in Band 5.

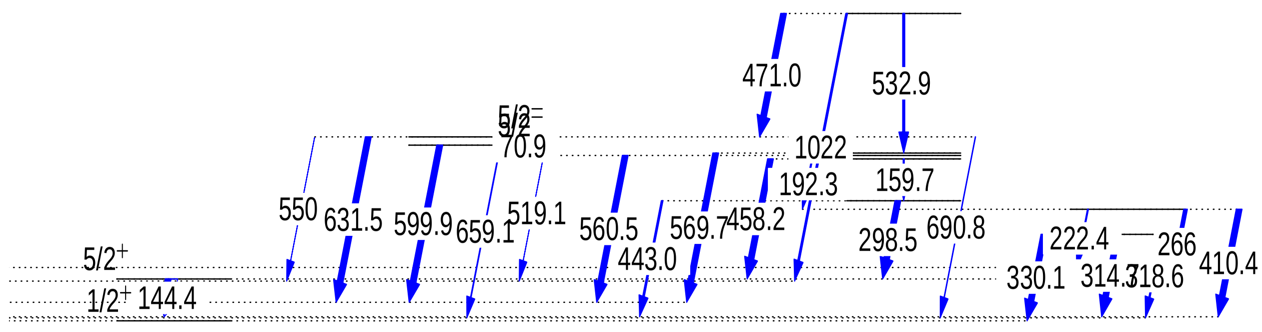

Figure 4.13: Unresolved gamma-rays at low spin from [43] all feeding Band 6.

$|\ \Delta I\ | = 3$ gamma-ray is shown in Figure 4.14 in light blue together with other E2 transitions in coincidence with the 500 keV transition. The transitions in red are in coincidence with the 500 keV transition but do not belong to Band 6.

4.3 Bands Feeding the Intrinsic states

Band 1a, 2a, 2b, 3a, 2c and 4a

The two bands Band 1a and Band 2a are partners with $(-, +\frac{1}{2})$ and $(-, -\frac{1}{2})$ signatures respectively. Both bands are feeding the yrast band through E2 transitions. The two bands have been altered by adding a 536 keV and 735 keV transitions feeding Band 1. The order of the gamma-rays in these bands has also been re-arranged. No bandcrossings were observed in this work for these bands. Band 2b $(+, \frac{1}{2})$ feeding Band 2 is the observed signature partner to Band 3a with $(+, -\frac{1}{2})$ signature. The new transitions are shown in red connecting Band 2b to Band 1 and those connecting Band 3a to Band 3. The new tentatively placed Bands 2c and 4a are observed feeding the yrast and ground state bands respectively.

4.4 Contaminants

In the total projection there were energy peaks belonging to other nuclei "contaminants" populated from other reaction channels. The two odd-odd isotopes ^{160}Tm and ^{162}Tm were observed with the highest abundance hence the level schemes built for these were to higher excitation energies with multiple bands as shown in Figure 4.15. They arise as a result of evaporation of 6 and 4 neutrons respectively from the compound nucleus ^{166}Tm. Despite the

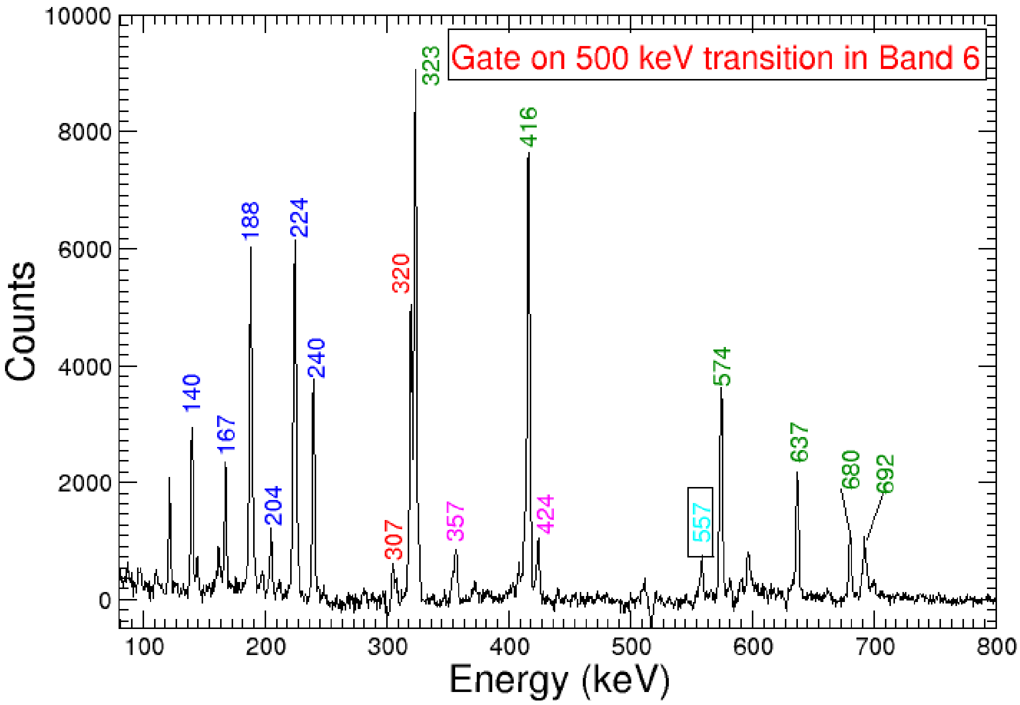

Figure 4.14: Spectrum corresponding to gate placed at the 500 keV E2 transition showing a representative rotational spectrum for the excited states in Band 6. The M1s in coincidence with the 500 keV transition are in blue. The red transitions are also in coincidence with the 500 keV transition but belong to Band 6 and 8. The E2 transitions belonging to Band 6 in green and the 557 keV $\mid \Delta I \mid = 3$ transition is shown in light blue.

relatively high yield of these two contaminants in the data no new gamma-rays were observed for either of the two nuclei. Figure 4.16 shows the other contaminants observed in the current study and these include ^{162}Er, ^{160}Er, ^{157}Ho and ^{158}Ho due to the β decay of ^{161}Tm as well as ^{152}Sm as a result of Coulomb excitation of the target.

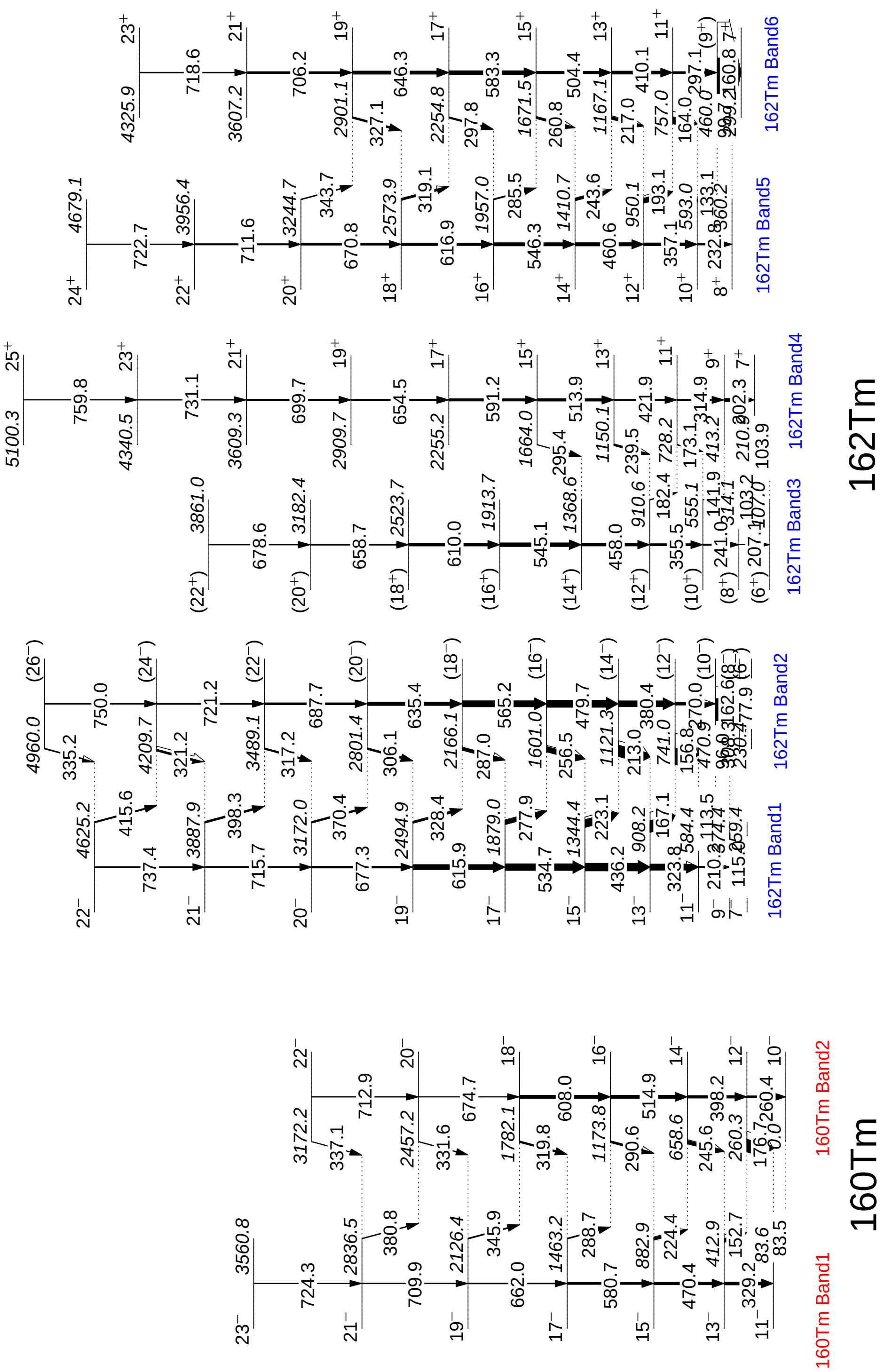

Figure 4.15: The ^{160}Tm and ^{162}Tm isotopes observed in the collected data.

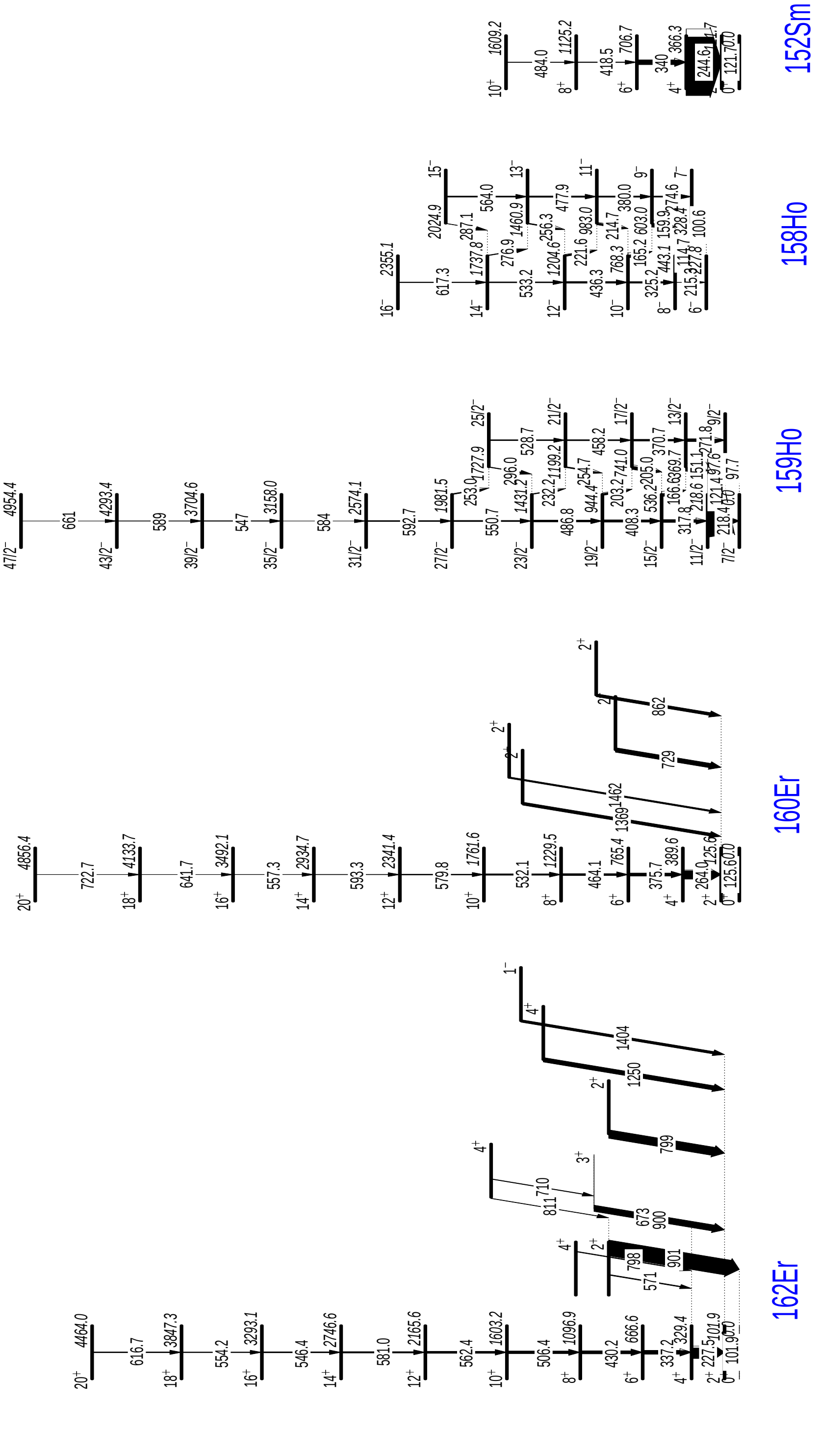

Figure 4.16: The ^{162}Er, ^{160}Er, ^{157}Ho and ^{158}Ho nuclei as a result of β decay of ^{161}Tm together with ^{152}Sm as mentioned due to the Coulomb excitation of the target.

Non-assigned Transitions

From the constructed level scheme, the couplings to the gamma bands that were expected were not observed. These couplings in the core would be $(\frac{7}{2}+2)=\frac{11}{2}^{+}$ and $(\frac{7}{2}-2)=\frac{3}{2}^{+}$ bandhead spins at an excitation energy in the range of $700-800$ keV. The new unassigned transitions do not occur at the expected spin hence we cannot firmly conclude that they are the coupling gamma-rays. However the new unassigned transitions shown in Figure 4.17 are suspected to be possible candidates of the couplings and this has to be further investigated.

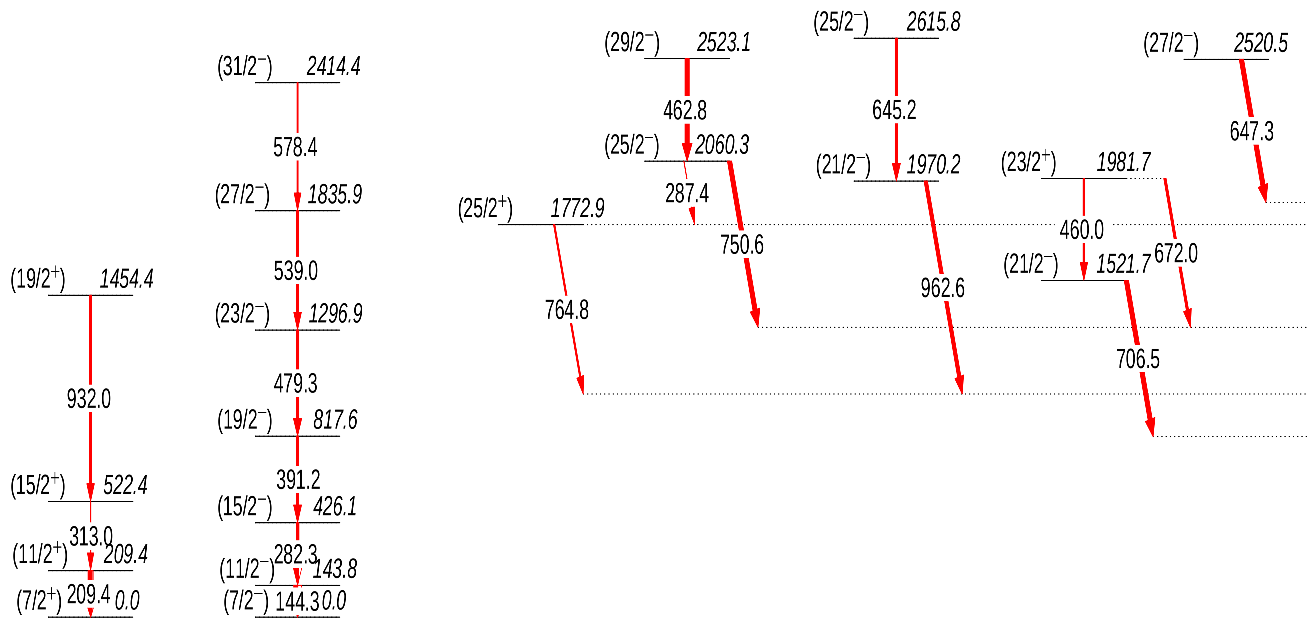

Figure 4.17: Some partial decay schemes corresponding to transitions that are possible candidates for high K structures. None of the spins in the partial level scheme are firmly assigned.

Chapter 5

Discussion

This chapter presents the interpretation of data based on alignments, band crossings and quasi-particle energies for different quasi-neutron and quasi-proton pairs. The backbending effects have been treated as a direct manifestation of bandcrossing because both phenomena are due to a change in the intrinsic configuration of the yrast sequence. The electromagnetic properties, specifically the experimental B(M1)/B(E2) ratios for the strong coupled bands in ^{161}Tm, were deduced in this work. Data has also been interpreted by comparing values obtained with available literature on alignments, bandcrossing frequencies and B(M1)/B(E2) values in neighbouring nuclei. The Cranked Shell model [24] has been used in assigning nucleon configurations to crossing bands.

5.1 Rotational alignments and Bandcrossings

The parameters taken from the Cranking Shell Model are defined as follows:

The total angular momentum along the rotation axis as a function of the total angular momentum I and rotational frequency ω:

$$I_x(I) = \sqrt{(I - \frac{1}{2})^2 - K^2} \tag{5.1}$$

$$I_x(\omega) = i_x(\omega) + R(\omega) \tag{5.2}$$

respectively, where i_x is the aligned angular momentum of the quasi-particles. The rotational frequency is given by‘:

$$\omega(I_x) = \frac{E(I+1) - E(I-1)}{2} \tag{5.3}$$

where $E(I+1)$ and $E(I-1)$ are the energies of the rotational states between which the transitions occured producing the two gamma-rays. To compute the collective angular momentum, the Harris parameters are needed. In this work the values used were from Smith *et al.* [2] where $J_0 = 30\hbar^2$ MeV^{-1} and $J_1 = 32\hbar^4$ MeV^{-3}. Therefore R(ω) is :

$$R(\omega) = J_0\omega + J_1\omega \tag{5.4}$$

and it follows that $i_x\omega$ is:

$$i_x\omega = I_x(\omega) - J_0\omega - J_1\omega \tag{5.5}$$

A plot of quasi-particle energies e’ (Routhian) as a function of rotational frequency in the rotating frame is presented in Figure 5.1. The Routhian plots were performed for the [523]7/2$^-$ (Band 1 and 2), [404]7/2$^+$ (Band 3 and 4) and [541]1/2$^-$ (Band 6) configurations. According to Figure 5.1 the AB crossing corresponding to the $i_{\frac{13}{2}}$ neutrons in the yrast band is firmly established at $\sim$ 0.280(5) MeV. This is a typical value for AB crossings in the mass region Z= $50 - 70$ associated with the $i_{\frac{13}{2}}$ neutrons. Signature splitting is observed for the signature partner bands: Band 1 and Band 2 which disappears after the AB crossing.

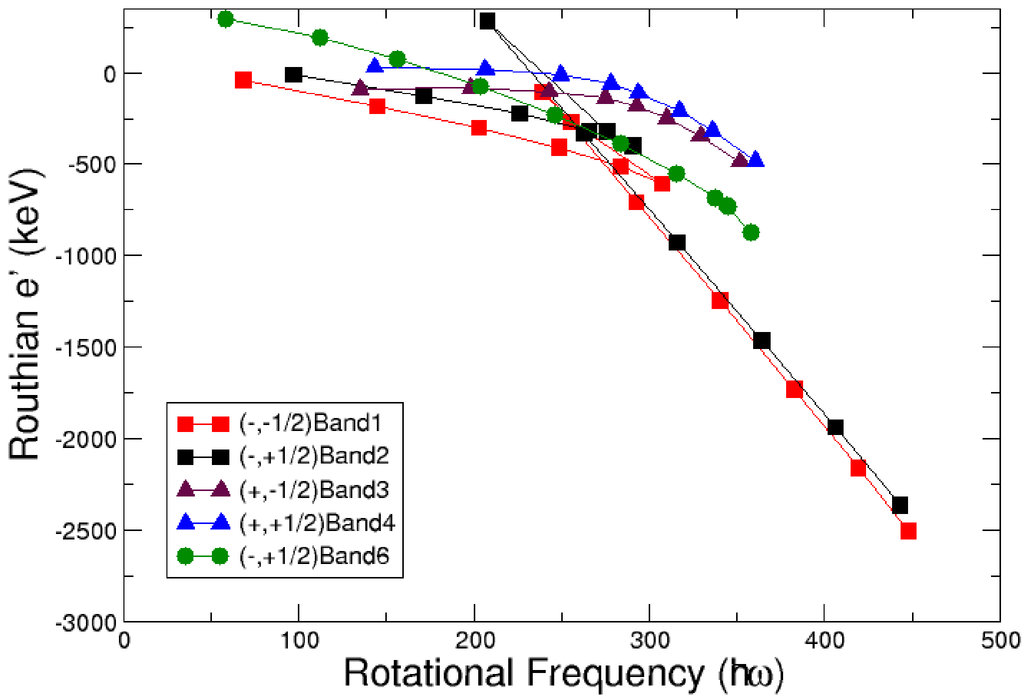

Figure 5.1: A plot of the Experimental Routhians versus the rotational frequency for bands built on the states: $[523]7/2^-$ (Band 1 and Band 2), $[404]7/2^+$ (Band 3 and Band 4) and $[541]1/2^-$ (Band 6).

A backbend should be observed in all bands since the odd quasi-proton does not block it. Figure 5.2 supports the observed crossing frequency corresponding to the AB neutron crossing in the $[523]7/2^-$ and $[404]7/2^+$ configurations which all backbend at $\sim 0.28(5)$ MeV. However the $[541]1/2^-$ band shows a striking behaviour as it upbends in the plot presented in Figure 5.2. The AB neutron crossing systematics involving the $[541]1/2^-$ for ^{163}Tm, ^{177}Re and ^{157}Ho are well documented in [42, 44, 45], and indicate a delay in the observed crossing frequency at a value of ~ 0.34 MeV. A slight upbend at ~ 0.43 MeV for Band 1 and Band 2 in this plot is attributed to the alignment of A_pB_p protons from the $h_{\frac{11}{2}}$ shell. However this upbend is not clearly observed as the data do not extend to higher spin.

The $[541]1/2^-$ (Band 6) has a moment of inertia greater than the $[523]7/2^-$ yrast ($\mathcal{J} > \mathcal{J}_{yrast}$) and is therefore probably more deformed (e.g like ^{156}Dy) and could therefore perhaps have a very strong interaction causing i_x to increase slowly from low spins. Then the AB crossing would be blocked and hence the upbend due to CD crossing. The corresponding alignment gains are:

$$\Delta i_x(AB) = \frac{13}{2} + \frac{11}{2} \tag{5.6}$$

$$\Delta i_x(CD) = \frac{9}{2} + \frac{7}{2} \tag{5.7}$$

The plot presented in Figure 5.3 is the excitation energy minus rigid rotor energy against the frequency for bands in this work. The couplings we were searching for give a plot similar to the one presented in Figure 5.4, however comparing with the plots for the bands in this work the $K_>$ and $K_<$ were not observed.

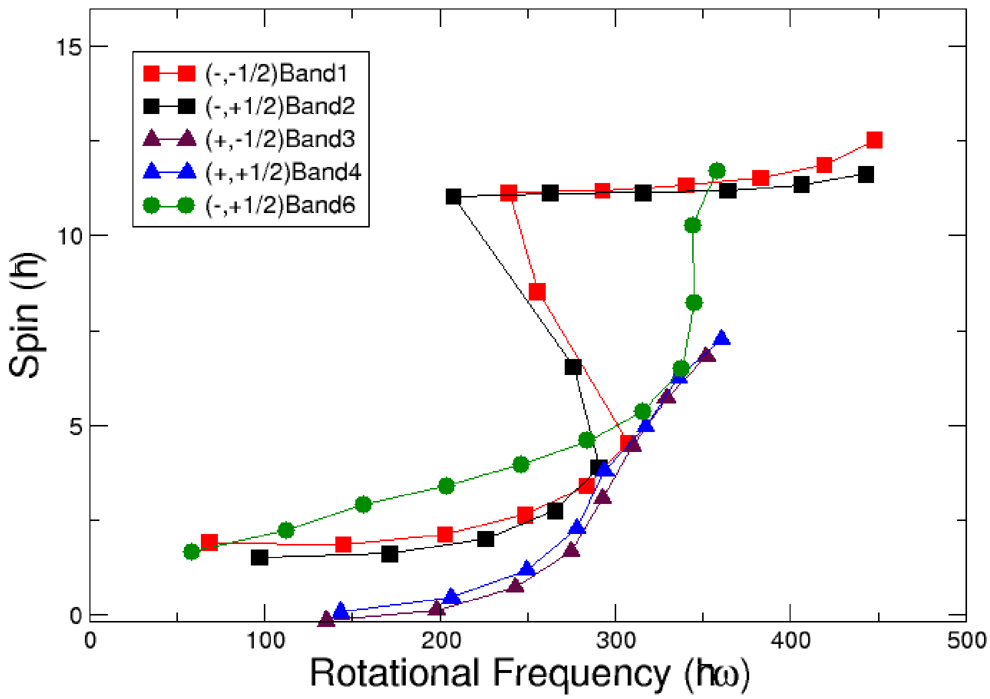

Figure 5.2: An alignment plot showing the alignment i_x for the two $[523]7/2^-$ yrast signatures (Band 1 and Band 2), the two ground state $[404]7/2^+$ signatures (Band 3 and Band 4) and the $[541]1/2^-$ configuration (Band 6).

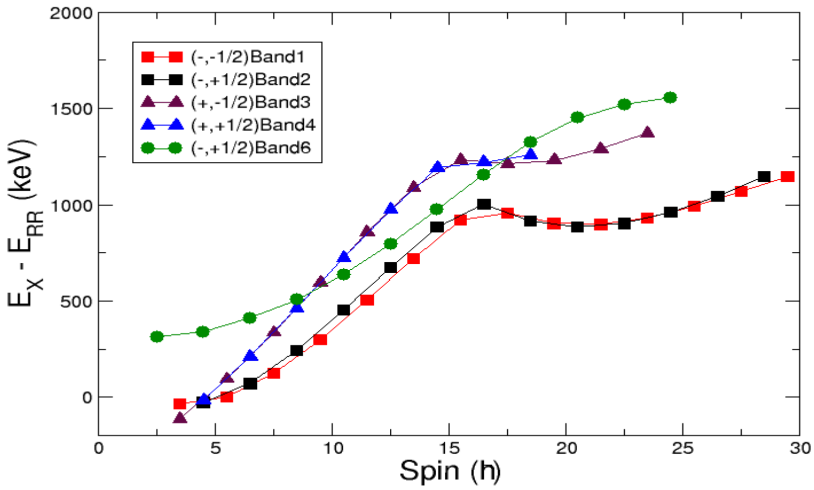

Figure 5.3: A plot of Excitation energies factoring out the Rigid rotor energies, against the frequency to show the crossing frequencies between the rotational bands built on the different intrinsic configurations in this work.

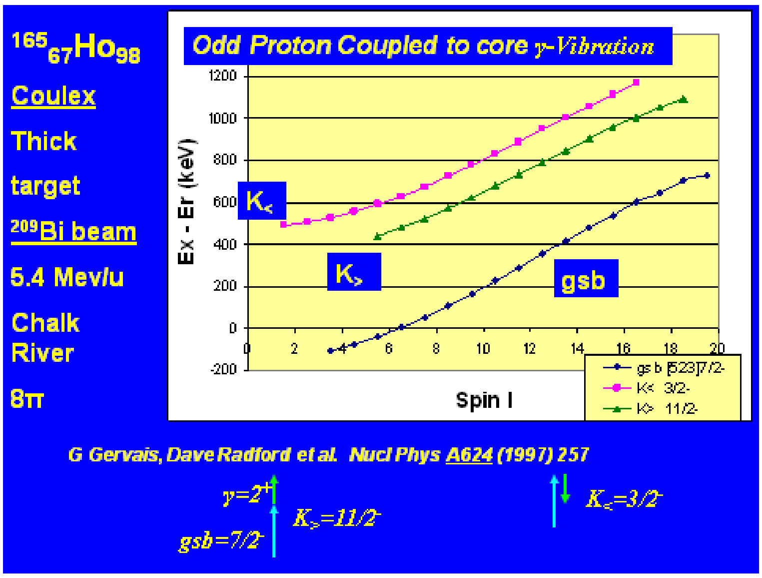

Figure 5.4: The only example known where both couplings $K_>$ and $K_<$ were observed [54].

Table 5.1: A table showing the crossing frequencies obtained in this work corresponding to the plots performed for the bands using Figure 5.2 for the backbends.

$(\pi, \alpha)_n$	AB crossing frequency (keV)	Band
(-,+1/2)	~0.27(5)	Band 2
(-,-1/2)	~0.27(5)	Band 1
(+,+1/2)	~0.28(5)	Band 4
(+,-1/2)	~ 0.28(5)	Band 3
(+,-1/2)	~ 0.34(5)	Band 6

Table 5.2: Nomenclature used to define participating quasi-particle trajectories taken from the Cranked Shell Model [53]

$(\pi, \alpha)_n$	Letter Symbol	Subshell	Nilsson quantum number
Quasi-neutron			
$(+, +1/2)_1$	A	$i_{\frac{13}{2}}$	[651]3/2+
$(+, -1/2)_1$	B	$i_{\frac{13}{2}}$	[651]3/2+
$(+, +1/2)_2$	C	$i_{\frac{13}{2}}$	[660]3/2+
$(+, -1/2)_2$	D	$i_{\frac{13}{2}}$	[660]3/2+
$(-, +1/2)_1$	E	$h_{\frac{9}{2}}$	[541]3/2-
$(-, -1/2)_1$	F	$h_{\frac{9}{2}}$	[541]3/2-
$(-, +1/2)_1$	G	$h_{\frac{13}{2}}$	[505]11/2-
$(-, -1/2)_1$	H	$h_{\frac{13}{2}}$	[505]11/2-
Quasi-proton			
$(-, -1/2)_1$	A_p	$h_{\frac{11}{2}}$	[523]7/2-
$(-+, +1/2)_1$	B_p	$h_{\frac{11}{2}}$	[523]7/2-
$(-, -1/2)_2$	C_p	$h_{\frac{11}{2}}$	[532]5/2+
$(-, +1/2)_2$	D_p	$h_{\frac{11}{2}}$	[532]5/2+
$(+, -1/2)_1$	E_f	$g_{\frac{11}{2}}$	[404]7/2+
$(+, +1/2)_1$	f_p	$g_{\frac{11}{2}}$	[404]7/2+

5.2 Systematics of Bandcrossings

Systematics were performed for the alignment plots and excitation energy minus rigid rotor energy in odd Z nuclei with neutron number N around

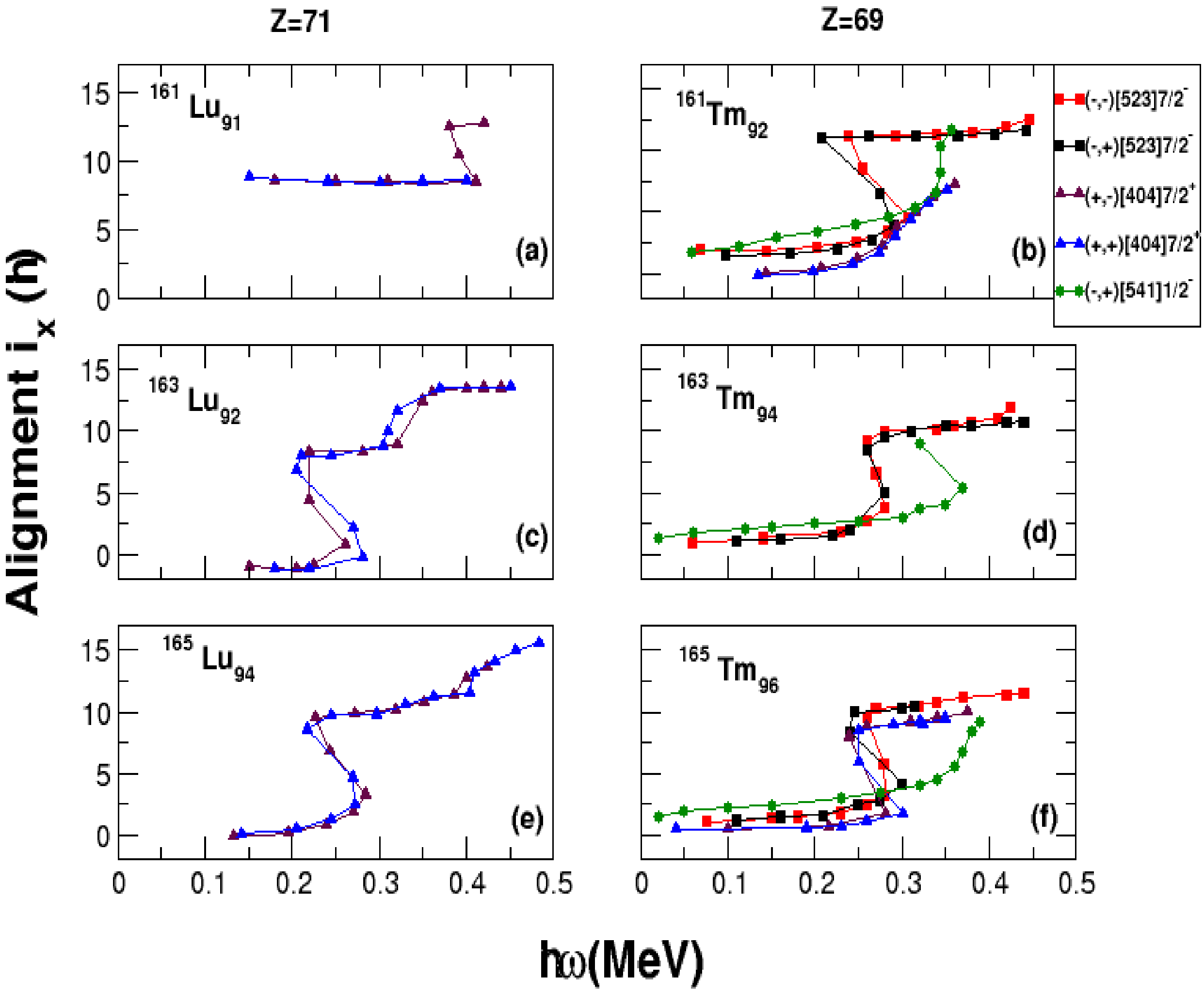

Figure 5.5: An alignment plot versus rotational frequency for odd Z nuclei containing the $[523]7/2^{-}$ and $[404]7/2^{+}$ configurations.

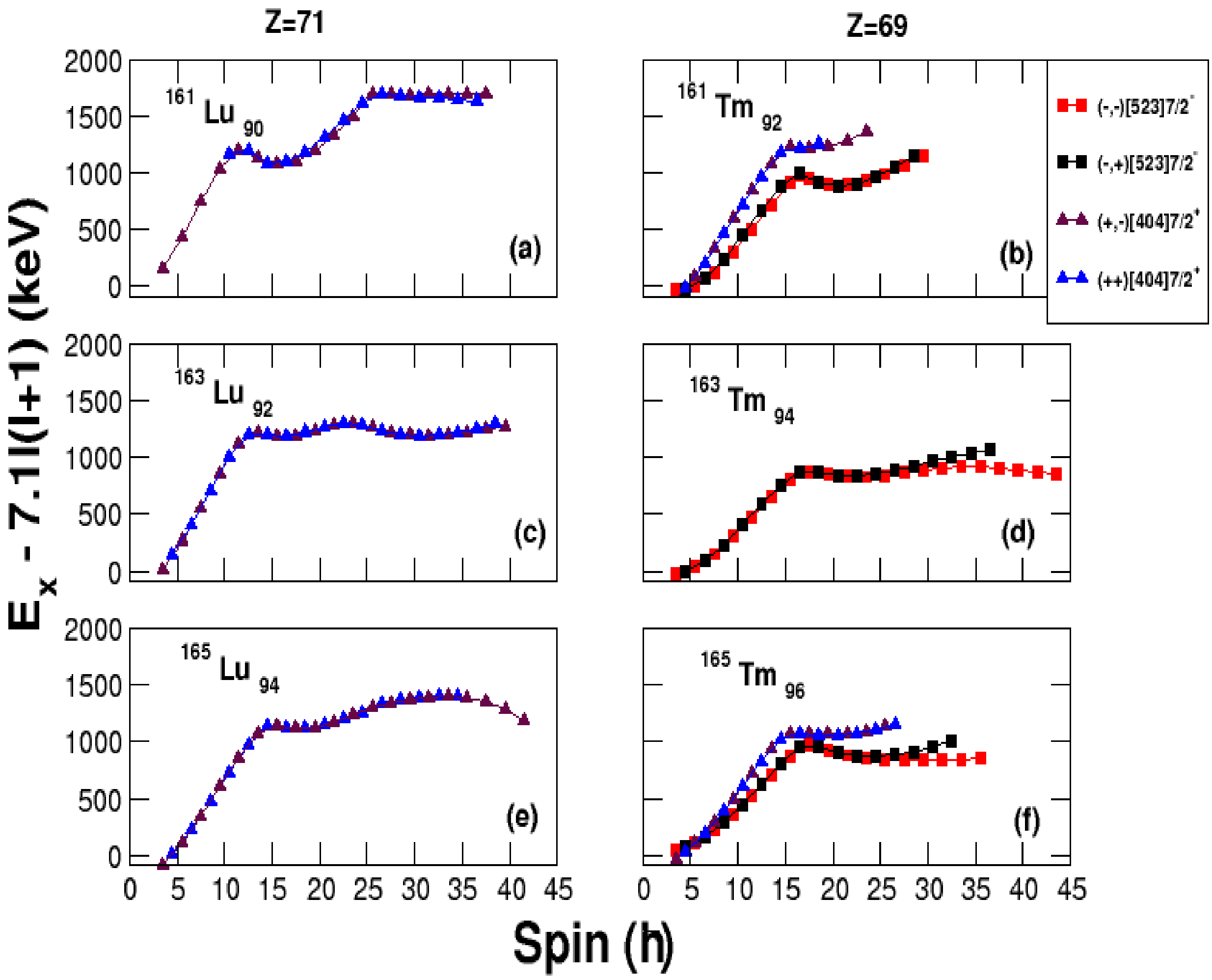

Figure 5.6: A plot for excitation energy minus rigid rotor energy, versus rotational frequency for odd Z nuclei with $[523]7/2^{-}$ and $[404]7/2^{+}$ configurations.

90. The plots containing systematic data are useful in observing a similar behavior or any anomalies in this case for rotational bands involving the $[523]7/2^{-}$ and/or $[404]7/2^{+}$ orbitals. The data used to plot Figures 5.5 and 5.6 were deduced from the level schemes obtained in [47, 48, 49] for the ^{161,163,165}Lu isotopes, while for the ^{161,165}Tm isotopes it was obtained from [50, 51] respectively. Regarding the alignment plots in Figure 5.6 we see that the Z=69 isotopes ^{161,163,165}Tm, the $[523]7/2^{-}$ bands all backbend at approximately the same frequency of $\sim$ 0.28(5) MeV. A comparison was also made with the neighbouring Z=71 isotopes ^{161,163,165}Lu which all have the $[404]7/2^{+}$ bands in common with ^{161,165}Tm isotopes. Both the ^{163,165}Lu nuclei have a first and second backbend at 0.20(5) MeV and 0.42(5) MeV respectively. The second backbending of the $[404]7/2^{+}$ bands is not observed in ^{161,165}Tm as they are predicted to occur only at a frequency above 0.45(5) MeV.

The ^{161}Lu nucleus is observed to only have one backbend which occurs at a delayed frequency of 0.40(5) MeV and only involving the $(+,-)$ signature. The plots for the excitation energies minus rigid rotor energy in Figure 5.6 show a consistency in the behaviour of the $[404]7/2^{+}$ bands in ^{161,163,165}Lu isotopes and in ^{161,163,165}Tm. Looking at the column with the Tm isotopes in part (b, d, f) a similar behaviour is observed for the yrast $[523]7/2^{-}$ bands.

Using an approach based on Pauli blocking arguments, bandcrossing in the even-even nucleus ^{156}Er has been interpreted by comparing with observed band crossings in neighbouring odd Z and odd N nuclei. Following such an approach Figure 5.7 shows typical values for the crossing frequency: part (a) shows the odd-neutron nucleus ^{159}Er alignments. It is observed that the $[505]11/2^{-}$ signatures have a higher critical alignment frequency as compared to the signatures of the neutron $[521]3/2^{-}$ ground state band.

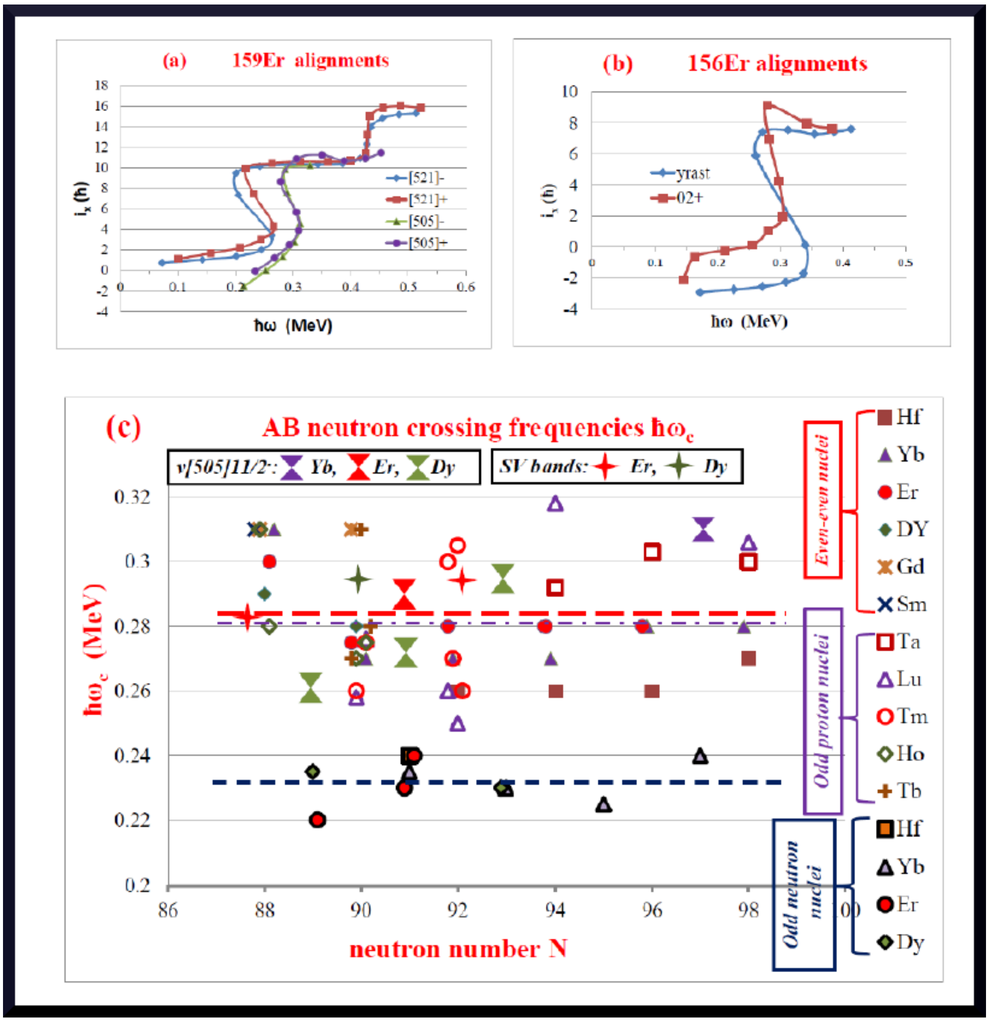

Figure 5.7: Part (a) shows an alignment plot for the ground states signatures together with the [505]11/2$^-$ signature in the odd-N nucleus ^{159}Er. Part (b) is a similar plot but for the 0_2^+ and yrast band in the even-even ^{156}Er nucleus and part (c) of the figure shows AB neutron crossing systematics in neighbouring, odd proton, odd neutron and even-even nuclei [46].

In the even-even ^{156}Er nucleus in part (b) of Figure 5.7 the alignment frequencies for both the yrast and 0_2^+ bands align at the same frequency showing a lack of blocking. For part (c) of Figure 5.7 the AB neutron crossing systematics in nuclei with N= $88 - 98$, the plot of neutron number against critical frequencies for different configurations shows the average values as would be expected for odd-proton (purple line), odd-neutron (red line) and even-even (dark blue line) nuclei. There is a significant reduction in critical frequency displayed for the odd-neutron configurations which is consistent with a degree of blocking as mentioned earlier in the chapter. The exception for the odd-neutron configurations is the $[505]11/2^-$ orbital shown with an hour glass symbol which appears at a much higher frequency.

The critical frequency for the odd-proton configurations is generally higher than that of the odd-neutrons because the occupation of an odd proton configuration does not block any of the neutron pairing, hence does not affect the frequency of aligning neutrons.

5.3 Electromagnetic properties (B(M1)/B(E2) Ratios)

The experimental B(M1)/B(E2) values and branching ratios in Table B.2 for the $[523]7/2^-$ bands are generally higher than for the $[404]7/2^+$ bands, due to the larger magnetic moment of the $h_{\frac{11}{2}}$ orbital for the yrast bands as compared to the $g_{\frac{7}{2}}$ orbital for the ground state.

There are no B(M1)/B(E2) experimental measurements performed in previous works for the coupled bands feeding the yrast and ground state bands. This study has performed such calculations for Band 1a, 2a, 2b and 3a shown in Figure 5.10 and 5.11. After the AB crossings in both the $[523]7/2^-$ and

[404]7/2$^+$ configurations, the B(M1)/B(E2) values increase. Such an effect is due to the excited $i_{\frac{13}{2}}$ neutrons having a greater contribution because the aligned angular momentum at such a frequency is high ($\sim 8\hbar$). The aligning neutrons have a larger contribution to the magnetic dipole moment component perpendicular to the symmetry axis. The M1 magnitude is proportional to this component, hence a larger B(M1) is expected, increasing the overall B(M1)/B(E2) value.

In support of the observed B(M1)/B(E2) experimental values, a comparison was performed with neighbouring nuclei containing the [523]7/2$^-$ and/or [404]7/2$^+$ strong coupled bands and where data was available for the ratios. Such systematics were performed in Figure 5.8 and Figure 5.9 and it is observed that the data for B(M1)/B(E2) experimental values for ^{161}Tm in the current work is of the same magnitude as that of neighbouring nuclei.

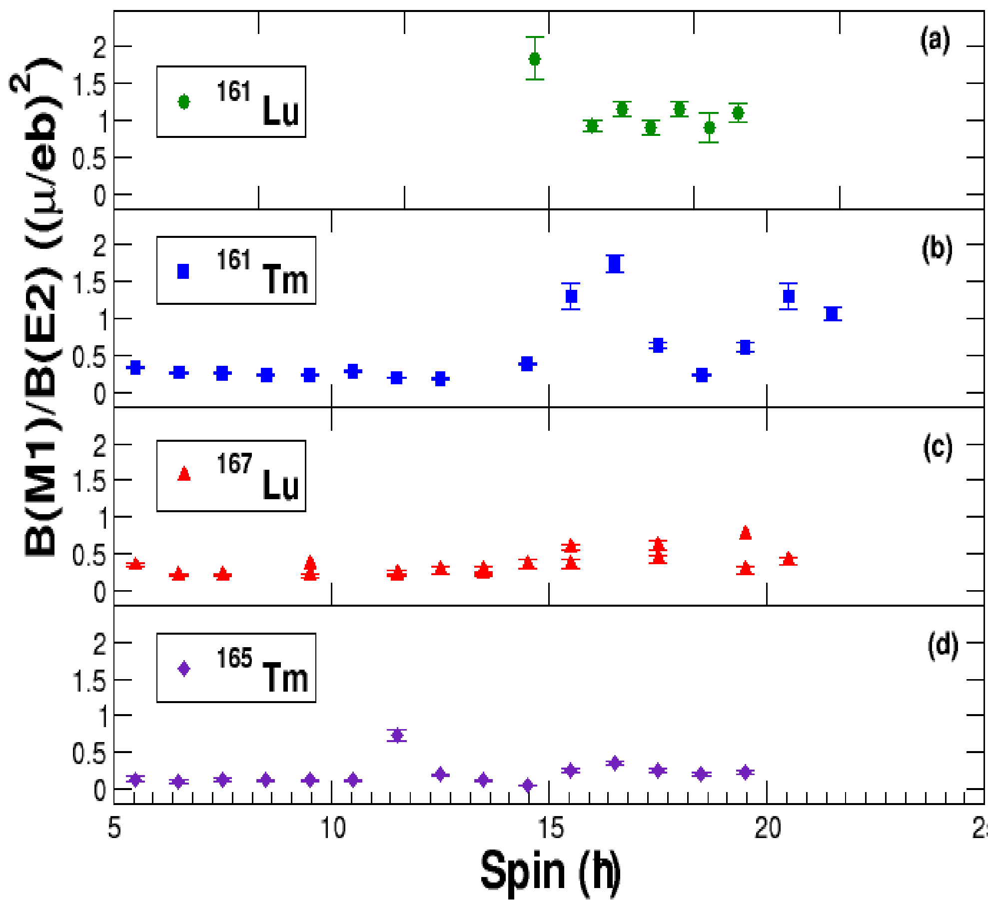

Figure 5.8: Experimental B(M1)/B(E2) systematics for [404]7/2^{+} in neighbouring nuclei in comparison with values for ^{161}Tm part (b) (in blue) obtained in this work.

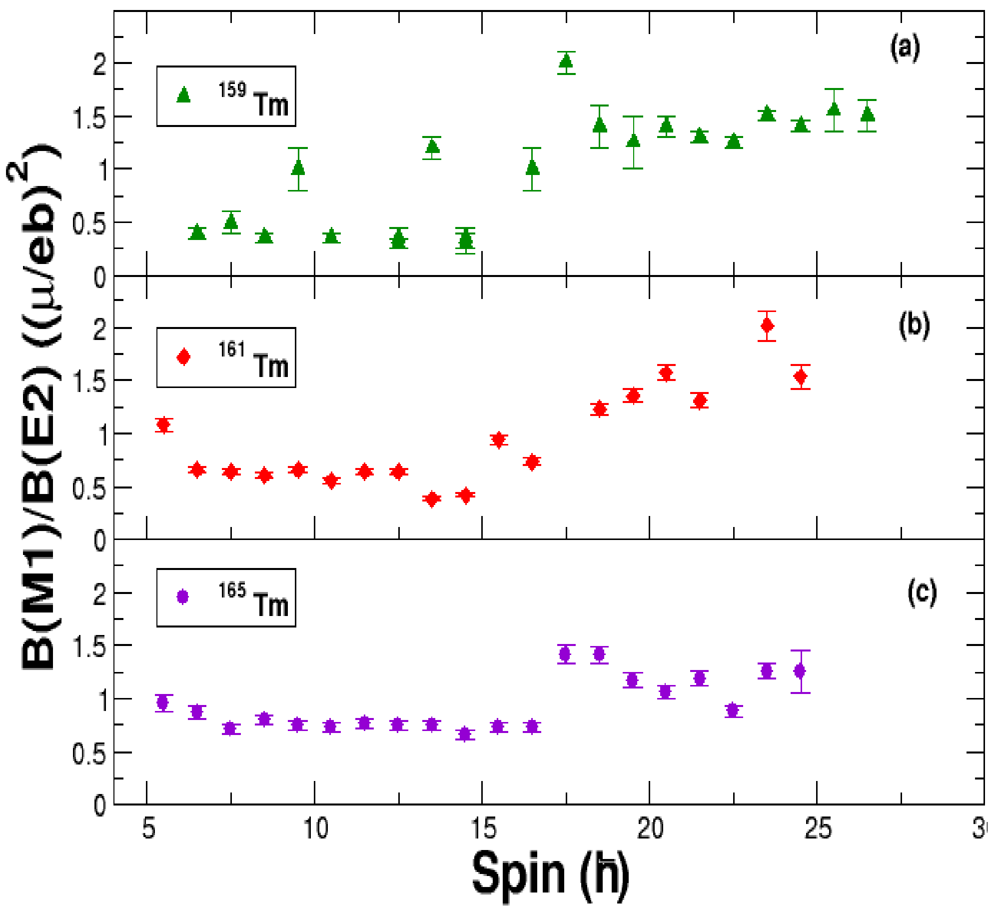

Figure 5.9: Experimental B(M1)/B(E2) systematics for [523]7/2$^-$ in neighbouring nuclei in comparison with values for ^{161}Tm part (b) (in red) obtained in this work.

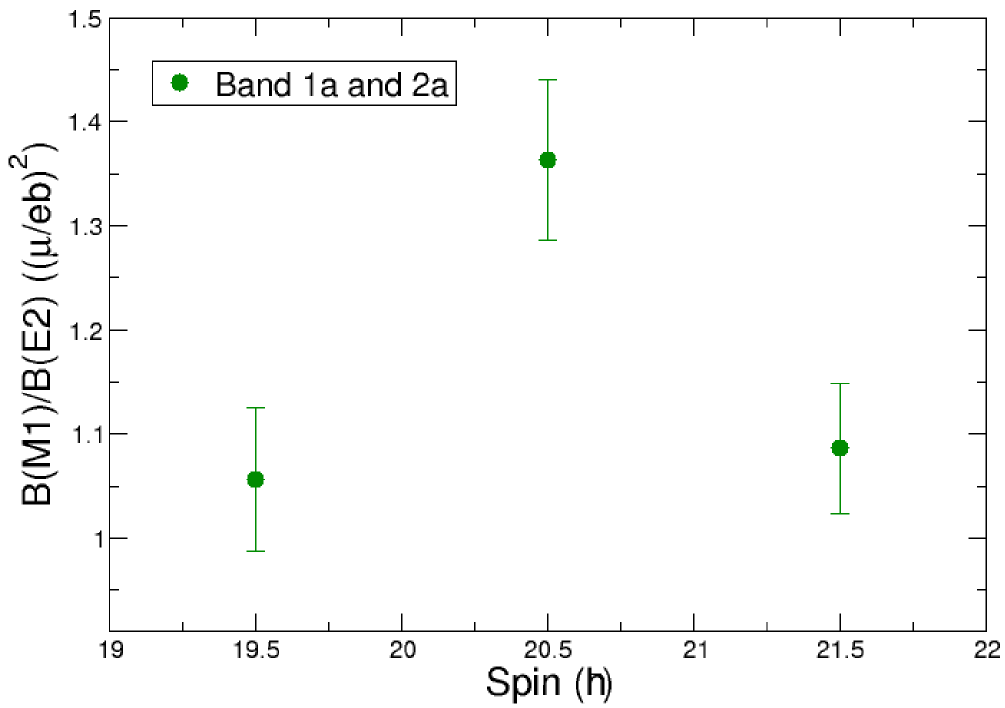

Figure 5.10: The B(M1)/B(E2) for the coupled Band 1a and Band 2a.

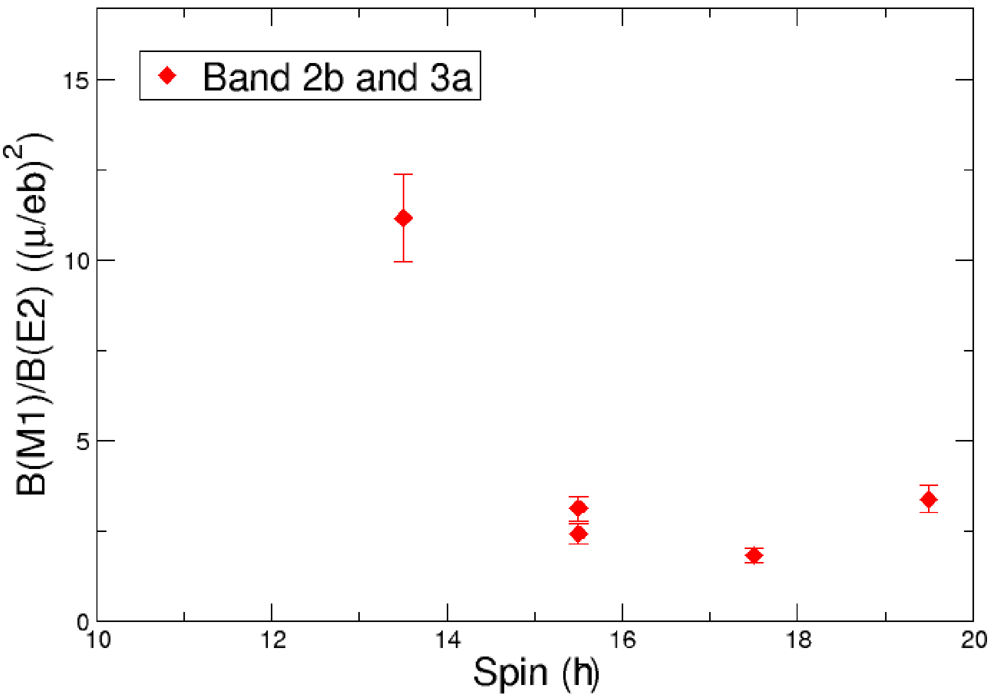

Figure 5.11: The B(M1)/B(E2) for the coupled Band 2b and Band 3a.

Chapter 6

Conclusion

This study has contributed to the known level scheme of ^{161}Tm by extending the $[402]5/2^{+}$ rotational band. This band has been extended by 4 more transitions extending to spin and parity $\frac{27}{2}^{+}$. In addition it is suspected that there is a wrong assignment of Nilsson number $[541]1/2^{-}$ to Band 6. Unfortunately there is no firm evidence supporting the coupling to the gamma bands (collective vibrations) hence [54] remains the only example where both couplings were fully established in one nucleus. The presence of these bands would have shed light on the mechanism of particle-excited core interaction. However there are possible candidates that were observed and this would need to be further investigated. Despite the absence of the coupled bands the computed experimental ratios B(M1)/B(E2) performed in this study reveal that at the respective crossing frequencies for the ground state and yrast band the B(M1)/B(E2) values increase, meaning that there is an interplay between the quasi-neutrons and the core because the angular momentum is partitioned between the two. There have been no B(M1)/B(E2) values determined for the coupled bands (Band 1a, Band 2a) and (Band 2b, Band 3a) in previous work, while this study obtained the experimental values.

The upbend in Band 6 observed in this work has been attributed to the CD neutrons while the crossings in the ground state [404]$7/2^+$ and yrast [523]$7/2^-$ configurations were attributed to be due to the AB. Some transitions were confirmed with DCO and/or polarization anisotropy measurements. However the rest remain tentatively placed in the level scheme due to the challenge of low statistics from the two matrices (DCO angle dependent matrix, polarization matrix) used to analyse the gamma-rays. Despite the complexity of an odd-proton nucleus, a detailed analysis of different rotational structures was possible in ^{161}Tm in the process of building a detailed level scheme.

Appendices

Appendix A

Branching Ratios

A.1 Branching ratios

An important quantity to determine in studying the nuclear electromagnetic properties is the branching ratio λ which represents the fraction of nuclei that will decay via one mode over the total number of nuclei that decay from the same state. Considering the level scheme of ^{161}Tm, the branching ratio would be the ratio of the intensity of the E2 stretched transition ($I \rightarrow I-2$), to the intensity of the mixed M1/E2 ($I \rightarrow I-1$). The equation used in determining the values for the branching ratios in this work is:

$$\lambda = \frac{I_\lambda(E2 : I \rightarrow I-2)}{I_\lambda(M1/E2 : I \rightarrow I-1)} \tag{A.1}$$

The experimentally determined branching ratios deduced in this study are for the [523]7/2$^-$ yrast, [404]7/2$^+$ ground state, Band (1a and 2a) and Band (2b and 3a) configurations. The values obtained are shown in table B.2. One can also deduce the B(M1)/B(E2) ratio (i.e the ratio of the reduced transition probabilities for magnetic transitions B(Mλ) to the electric transitions B(Eλ)) to obtain information on nuclear wave functions. The reduced transition probabilities give insight on nuclear wave functions and nuclear deformation. The branching ratios provide information on how the nuclear angular momentum can be attributed to core and to that of the quasiparticles. [2]. Using the rotational model [52] the $B(E2 : I \rightarrow I-2)$ is:

$$B(E2 : I \rightarrow I-2) = \frac{5}{16\pi} e^2 Q_0 (I_i Q_0^2 \langle I_i 2KO | I_f K \rangle) \tag{A.2}$$

where:

K - is the projection of the total angular momentum on the symmetry axis

Q_0 - represents the intrinsic quadrupole moment.

A suitable equation to compute the $B(M1 : I \rightarrow I-1)$ values is derived from [41] and is given by:

$$B(M1 : I \rightarrow I-1) = \frac{3K^2}{8\pi I}[(g_p - g_R)(\sqrt{I^2 - K^2} - i_p) - (g_n - g_R)i_n]^2 (\mu_n)^2 \tag{A.3}$$

where:

g_p, g_R, g_n are the gyromagnetic ratios for the proton , neutron and collective rotation respectively

and i_n, i_p represent the aligned angular momentum along the rotation axis of the neutron and proton respectively.

The B(M1)/B(E2) can then be deduced using the extracted branching ratios λ in the equation:

$$\frac{B(M1 : I \rightarrow I-1)}{B(E2 : I \rightarrow I-2)} = 0.693 \frac{(E_\lambda(I \rightarrow I-2))^5}{(E_\lambda(I \rightarrow I-1))^3} \times \frac{1}{\lambda + \delta^2} \tag{A.4}$$

Appendix B

List of gamma-rays and Assignments

The terms used in table B.1 are explained as follows:

- E_i is the excitation energy of the initial level of the gamma-ray
- J_i^π is the spin and parity of the initial level
- J_f^π is the spin and parity of the final level
- E_γ represents the energy of the gamma-ray
- I_γ represents the intensity of the gamma-ray
- MultiP is the multipolarity of the gamma-ray
- DCO_{ratio} refers to the direct ratios from analysis of the angle dependent matrix used to confirm multipolarity
- DCO Uncer is the calculated uncertainty in the DCO ratio

- A_p refers to the polarization anisotropy measurement to confirm the parities
- A_p Uncert is the calculated uncertainty in the polarization anisotropy measurement
- - represents values that could not be obtained due to insufficient statistics

Table B.1: List of gamma rays detected with spin and parity assignments

$E_i(keV)$	J_i^π	$\rightarrow$	J_f^π	E_γ	I_γ	MultP	DCO_{ratio}	DCO Uncert	A_p	A_p Uncert
Band 1 $[523]7/2^-(-,-\frac{1}{2})$										
78	$7/2^-$	$\rightarrow$	$7/2^+$	78.00(10)	10.0(10)	E1	0.576	0.018	-	-
254	$11/2^-$	$\rightarrow$	$9/2^-$	105.48(3)	209(7)	M1	0.639	0.011	-	-
254	$11/2^-$	$\rightarrow$	$7/2^-$	176.33(4)	19.5(8)	E2	1.148	0.085	-	-
577	$15/2^-$	$\rightarrow$	$13/2^-$	159.90(3)	141(4)	M1	0.635	0.011	-0.481	0.633
577	$15/2^-$	$\rightarrow$	$11/2^-$	322.61(3)	130(4)	E2	1.042	0.008	0.142	0.241
1008	$19/2^-$	$\rightarrow$	$17/2^-$	192.76(3)	73.0(22)	M1	-	-	-0.107	0.005
1008	$19/2^-$	$\rightarrow$	$15/2^-$	431.19(3)	161(5)	E2	1.008	0.008	0.096	0.008
1525	$23/2^-$	$\rightarrow$	$21/2^-$	215.23(3)	33.5(10)	M1	0.628	0.014	-0.176	0.005
1525	$23/2^-$	$\rightarrow$	$19/2^-$	517.10(3)	134(4)	E2	-	-	0.168	0.026
2110	$27/2^-$	$\rightarrow$	$25/2^-$	240.26(3)	10.2(4)	M1	-	-	-	-
2110	$27/2^-$	$\rightarrow$	$23/2^-$	583.73(3)	89(3)	E2	-	-	0.244	0.02
2738	$31/2^-$	$\rightarrow$	$29/2^-$	255.41(3)	10.9(4)	M1	-	-	-0.131	0.007
2738	$31/2^-$	$\rightarrow$	$27/2^-$	627.86(3)	46.9(14)	E2	-	-	0.057	0.005
3257	$35/2^-$	$\rightarrow$	$33/2^-$	204.53(3)	26.3(8)	M1	0.626	0.025	-0.303	0.003
3257	$35/2^-$	$\rightarrow$	$31/2^-$	517.10(4)	1.54(23)	E2	-	-	-	-
3741	$39/2^-$	$\rightarrow$	$37/2^-$	263.28(3)	14.4(5)	M1	0.616	0.034	-	-
3741	$39/2^-$	$\rightarrow$	$35/2^-$	484.73(3)	10.8(4)	E2	1.200	0.126	-	-
4333	$43/2^-$	$\rightarrow$	$41/2^-$	318.47(4)	9.3(3)	M1	-	-	-0.193	0.007
4333	$43/2^-$	$\rightarrow$	$39/2^-$	591.60(4)	11.0(4)	E2	-	-	-	-
5020	$47/2^-$	$\rightarrow$	$45/2^-$	362.05(6)	2.82(14)	M1	-	-	-0.416	0.005
5020	$47/2^-$	$\rightarrow$	$43/2^-$	686.76(5)	3.12(16)	E2	-	-	-	-
5791	$51/2^-$	$\rightarrow$	$49/2^-$	394.95(5)	4.27(18)	M1	-	-	-	-
5791	$51/2^-$	$\rightarrow$	$47/2^-$	771.48(6)	1.54(10)	E2	-	-	-	-
6635	$55/2^-$	$\rightarrow$	$51/2^-$	844.25(4)	4.49(17)	E2	-	-	-	-
7536	$59/2^-$	$\rightarrow$	$55/2^-$	900.48(9)	0.80(8)	E2	-	-	-	-
Band 2 $[523]7/2^-(-,+\frac{1}{2})$										

149	$9/2^- \rightarrow 7/2^-$	70.70(10)	294(11)	M1	0.400	0.038	-	-
417	$13/2^- \rightarrow 11/2^-$	162.68(3)	234(7)	M1	0.668	0.010	-0.398	0.488
417	$13/2^- \rightarrow 9/2^-$	268.29(3)	80(3)	E2	-	-	-	-
815	$17/2^- \rightarrow 15/2^-$	238.15(3)	118(4)	M1	0.699	0.012	-0.319	0.004
815	$17/2^- \rightarrow 13/2^-$	398.22(3)	100(3)	E2	-	-	0.161	0.425
1310	$21/2^- \rightarrow 19/2^-$	301.74(3)	65.3(20)	M1	0.632	0.020	-0.072	0.311
1310	$21/2^- \rightarrow 17/2^-$	494.67(3)	87(3)	E2	1.138	0.022	0.247	0.007
1873	$25/2^- \rightarrow 23/2^-$	348.58(3)	42.7(13)	M1	0.513	0.100	-	-
1873	$25/2^- \rightarrow 21/2^-$	564.07(3)	71.7(22)	E2	1.126	0.083	0.076	0.099
2482	$29/2^- \rightarrow 27/2^-$	372.08(3)	24.3(8)	M1	0.660	0.013	-	-
2482	$29/2^- \rightarrow 25/2^-$	607.23(3)	64.1(20)	E2	-	-	0.256	0.006
3052	$33/2^- \rightarrow 31/2^-$	314.47(3)	16.5(5)	M1	-	-	-0.381	0.007
3052	$33/2^- \rightarrow 29/2^-$	570.27(3)	30.1(9)	E2	1.043	0.039	-	-
3478	$37/2^- \rightarrow 35/2^-$	221.55(3)	20.3(6)	M1	0.566	0.033	-0.293	0.003
3478	$37/2^- \rightarrow 33/2^-$	426.01(3)	14.8(5)	E2	1.000	0.042	0.176	0.121
4014	$41/2^- \rightarrow 39/2^-$	273.07(3)	11.7(4)	M1	0.513	0.056	-	-
4014	$41/2^- \rightarrow 37/2^-$	536.39(4)	11.3(4)	E2	0.897	0.054	0.115	0.095
4658	$45/2^- \rightarrow 43/2^-$	324.99(4)	9.9(3)	M1	-	-	-	-
4658	$45/2^- \rightarrow 41/2^-$	642.91(5)	7.2(3)	E2	-	-	-	-
5396	$49/2^- \rightarrow 47/2^-$	376.47(6)	2.16(12)	M1	-	-	-	-
5396	$49/2^- \rightarrow 45/2^-$	738.91(5)	4.03(17)	E2	-	-	-	-
6219	$53/2^- \rightarrow 51/2^-$	428.79(8)	2.45(14)	M1	-	-	-	-
6219	$53/2^- \rightarrow 49/2^-$	822.16(8)	1.31(10)	E2	-	-	-	-
7115	$57/2^- \rightarrow 53/2^-$	895.52(7)	1.97(10)	E2	-	-	-	-
Band 3 [404]$7/2^+(+,-\frac{1}{2})$								
788	$15/2^+ \rightarrow 11/2^+$	440.71(3)	56.9(18)	E2	-	-	0.386	0.006
1305	$19/2^+ \rightarrow 17/2^+$	268.29(4)	9.8(3)	M1	0.428	0.558	-	-
1305	$19/2^+ \rightarrow 15/2^+$	516.51(3)	53.7(17)	E2	0.855	0.009	0.048	0.005
1877	$23/2^+ \rightarrow 21/2^+$	294.88(4)	5.88(22)	M1	0.632	0.072	-	-
1877	$23/2^+ \rightarrow 19/2^+$	571.74(3)	47.5(15)	E2	0.929	0.015	0.076	0.443
2478	$27/2^+ \rightarrow 25/2^+$	305.40(10)	5.62(22)	M1	0.588	0.104	-	-
2478	$27/2^+ \rightarrow 23/2^+$	601.50(10)	39.6(12)	E2	0.907	0.034	-	-
3049	$31/2^+ \rightarrow 29/2^+$	263.00(10)	1.01(10)	M1	0.431	0.283	-0.252	0.009
3049	$31/2^+ \rightarrow 27/2^+$	571.40(10)	1.79(17)	E2	-	-	-	-
3511	$35/2^+ \rightarrow 33/2^+$	240.50(10)	3.89(19)	M1	0.653	0.112	-0.143	0.007
3511	$35/2^+ \rightarrow 31/2^+$	462.40(10)	6.47(24)	E2	-	-	-	-
4069	$39/2^+ \rightarrow 37/2^+$	287.60(10)	1.32(11)	M1	0.330	0.124	-0.635	0.031
4069	$39/2^+ \rightarrow 35/2^+$	557.80(10)	3.40(17)	E2	-	-	-	-
4723	$43/2^+ \rightarrow 41/2^+$	335.40(10)	2.06(13)	M1	-	-	-	-
4723	$43/2^+ \rightarrow 39/2^+$	653.90(10)	4.22(17)	E2	1.248	0.111	0.179	0.003

5460	$47/2^+$	$\rightarrow$	$43/2^+$	737.30(10)	1.79(12)	E2	-	-	0.076	0.004
162	$9/2^+$	$\rightarrow$	$7/2^+$	161.67(3)	10.0(10)	M1	0.553	0.008	-	-
557	$13/2^+$	$\rightarrow$	$11/2^+$	208.99(3)	18.7(6)	M1	0.625	0.029	-	-
Band 4 [404]$7/2^+(+,+\frac{1}{2})$										
557	$13/2^+$	$\rightarrow$	$9/2^+$	395.69(3)	50.0(16)	E2	0.951	0.010	0.333	0.007
1037	$17/2^+$	$\rightarrow$	$15/2^+$	248.09(3)	10.5(4)	M1	0.544	0.048	-0.053	0.009
1037	$17/2^+$	$\rightarrow$	$13/2^+$	479.66(3)	50.5(16)	E2	-	-	0.065	0.005
1582	$21/2^+$	$\rightarrow$	$19/2^+$	276.86(4)	8.9(3)	M1	-	-	-	-
1582	$21/2^+$	$\rightarrow$	$17/2^+$	545.28(3)	48.6(15)	E2	0.941	0.011	0.026	0.007
2172	$25/2^+$	$\rightarrow$	$23/2^+$	295.60(4)	2.92(16)	M1	0.632	0.072	-	-
2172	$25/2^+$	$\rightarrow$	$21/2^+$	590.48(3)	30.8(10)	E2	0.938	0.021	0.024	0.005
2786	$29/2^+$	$\rightarrow$	$27/2^+$	308.40(10)	3.23(17)	M1	0.463	0.237	-	-
2786	$29/2^+$	$\rightarrow$	$25/2^+$	613.80(10)	16.9(5)	E2	0.967	0.038	0.187	0.005
3271	$33/2^+$	$\rightarrow$	$31/2^+$	221.90(10)	3.91(18)	M1	-	-	-	-
3271	$33/2^+$	$\rightarrow$	$29/2^+$	484.80(10)	3.80(17)	E2	-	-	0.076	0.003
3782	$37/2^+$	$\rightarrow$	$35/2^+$	270.20(10)	2.59(15)	M1	-	-	-	-
3782	$37/2^+$	$\rightarrow$	$33/2^+$	510.81(5)	13.1(4)	E2	0.956	0.078	-	-
4388	$41/2^+$	$\rightarrow$	$39/2^+$	318.50(10)	2.76(16)	M1	-	-	-	-
4388	$41/2^+$	$\rightarrow$	$37/2^+$	606.10(10)	6.8(3)	E2	-	-	-	-
Band 5 [402]$5/2^+$										
159	$7/2^+$	$\rightarrow$	$5/2^+$	140.07(4)	10.0(10)	M1	-	-	-	-
515	$11/2^+$	$\rightarrow$	$9/2^+$	188.59(4)	10.6(5)	M1	-	-	-	-
515	$11/2^+$	$\rightarrow$	$7/2^+$	356.50(5)	6.5(3)	E2	-	-	0.554	0.002
940	$15/2^+$	$\rightarrow$	$11/2^+$	424.43(4)	14.9(5)	E2	1.158	0.06	0.222	0.312
1442	$19/2^+$	$\rightarrow$	$15/2^+$	502.70(4)	12.6(4)	E2	1.139	0.20	0.069	0.003
2001	$23/2^+$	$\rightarrow$	$19/2^+$	558.84(4)	11.0(4)	E2	-	-	0.174	0.003
2592	$27/2^+$	$\rightarrow$	$23/2^+$	591.30(5)	5.63(21)	E2	1.269	0.09	-	-
Band 6 [541]$1/2^-$										
377	$5/2^-$	$\rightarrow$	$5/2^+$	357.26(7)	10.0(10)	E1	-	-	0.554	0.003
517	$9/2^-$	$\rightarrow$	$5/2^-$	138.95(15)	1.46(9)	E2	-	-	-	-
517	$9/2^-$	$\rightarrow$	$9/2^+$	189.56(5)	7.6(4)	E1	-	-	-	-
517	$9/2^-$	$\rightarrow$	$7/2^+$	304.97(6)	4.97(25)	E1	-	-	-	-
757	$13/2^-$	$\rightarrow$	$11/2^+$	224.84(4)	25.1(8)	E1	-	-	-	-
757	$13/2^-$	$\rightarrow$	$9/2^-$	239.52(4)	10.2(4)	E2	-	-	0.369	0.004
757	$13/2^-$	$\rightarrow$	$11/2^+$	240.70(6)	4.81(22)	E1	-	-	-	-
1080	$17/2^-$	$\rightarrow$	$13/2^-$	323.56(3)	40.2(13)	E2	-	-	0.095	0.022
1496	$21/2^-$	$\rightarrow$	$17/2^-$	416.27(3)	33.4(10)	E2	-	-	0.093	0.004
1496	$21/2^-$	$\rightarrow$	$15/2^+$	556.70(10)	10.0(10)	E3	-	-	-	-
1997	$25/2^-$	$\rightarrow$	$21/2^-$	500.32(3)	25.0(8)	E2	1.024	0.015	-	-
1997	$25/2^-$	$\rightarrow$	$19/2^+$	554.40(10)	10.0(10)	E3	-	-	0.592	0.119

2571	29/2$^-$	→	25/2$^-$	574.45(3)	16.4(5)	E2	1.333	0.081	0.099	0.006
3208	33/2$^-$	→	29/2$^-$	637.08(4)	10.0(3)	E2	0.996	0.056	-	-
3889	37/2$^-$	→	33/2$^-$	680.45(4)	5.28(18)	E2	1.114	0.054	-	-
4581	41/2$^-$	→	37/2$^-$	693.03(5)	4.73(17)	E2	1.242	0.411	0.724	0.006
5273	45/2$^-$	→	41/2$^-$	691.00(7)	2.36(10)	E2	-	-	-	-
5991	49/2$^-$	→	45/2$^-$	718.33(10)	0.64(6)	E2	-	-	-	-
Band 7 [411]1/2$^+$										
211	7/2$^+$	→	3/2$^+$	188.15(3)	10.0(10)	E2	-	-	-	-
531	11/2$^+$	→	9/2$^+$	204.13(5)	5.41(22)	M1	-	-	-	-
531	11/2$^+$	→	7/2$^+$	320.30(4)	26.0(8)	E2	1.025	0.015	-	-
531	11/2$^+$	→	7/2$^+$	371.70(5)	2.45(17)	E2	-	-	-	-
989	15/2$^+$	→	11/2$^+$	458.30(7)	0.63(21)	E2	-	-	-	-
Band 1a										
2846	31/2$^-$	→	27/2$^-$	735.60(10)	10.0(10)	E2	-	-	-	-
3382	35/2$^-$	→	31/2$^-$	535.60(10)	0.85(15)	E2	-	-	-	-
3382	35/2$^-$	→	31/2$^-$	643.90(10)	10.0(10)	E2	-	-	-	-
3383	35/2$^-$	→	33/2$^-$	264.20(10)	3.84(19)	M1	-	-	-	-
3383	35/2$^-$	→	33/2$^-$	330.53(5)	3.01(17)	M1	0.562	0.168	-	-
4010	39/2$^-$	→	37/2$^-$	286.50(10)	2.77(14)	M1	-	-	-	-
4010	39/2$^-$	→	35/2$^-$	627.50(10)	7.5(3)	E2	0.837	0.018	-	-
4641	43/2$^-$	→	41/2$^-$	311.10(10)	3.72(17)	M1	0.845	0.162	-	-
Band 2a										
4641	43/2$^-$	→	39/2$^-$	631.20(10)	7.9(3)	E2	1.237	0.070	-	-
3118	33/2$^-$	→	31/2$^-$	380.24(5)	8.0(3)	M1	-	-	-	-
3118	33/2$^-$	→	29/2$^-$	636.00(10)	12.0(4)	E2	-	-	-	-
3724	37/2$^-$	→	33/2$^-$	604.41(9)	15.5(5)	E2	-	-	-	-
4330	41/2$^-$	→	39/2$^-$	320.10(10)	6.20(24)	M1	-	-	-	-
4330	41/2$^-$	→	37/2$^-$	606.60(10)	7.9(3)	E2	-	-	-	-
5033	45/2$^-$	→	41/2$^-$	702.52(5)	5.96(22)	E2	-	-	-	-
Band 2b										
2308	27/2$^+$	→	25/2$^+$	534.60(10)	2.55(18)	M1	-	-	-	-
2308	27/2$^+$	→	23/2$^-$	782.20(10)	10.0(10)	M2	-	-	-	-
2718	31/2$^+$	→	27/2$^+$	195.70(10)	10.0(10)	E2	-	-	-	-
2718	31/2$^+$	→	27/2$^+$	410.30(10)	5.84(24)	E2	-	-	-	-
2718	31/2$^+$	→	25/2$^-$	844.60(10)	8.1(3)	E3	-	-	-	-
3157	35/2$^+$)	→	31/2$^+$	231.50(10)	10.0(10)	E2	0.878	0.066	-	-
3157	35/2$^+$	→	31/2$^+$	438.80(10)	7.4(3)	E2	-	-	-	-
3157	35/2$^+$	→	27/2$^-$	1046.20(10)	2.18(12)	M4	-	-	-	-
3672	39/2$^+$	→	35/2$^+$	275.60(10)	10.0(10)	E2	-	-	-	-
3672	39/2$^+$	→	35/2$^+$	515.20(10)	13.2(5)	E2	0.842	0.081	0.048	0.333

Band 3a								
2522	$27/2^+ \rightarrow 23/2^+$	645.40(10)	7.0(3)	E2	-	-	-	-
2925	$31/2^+ \rightarrow 31/2^+$	207.30(10)	10.0(10)	M1	0.732	0.443	-	-
2925	$31/2^+ \rightarrow 27/2^+$	403.00(10)	3.40(14)	E2	1.215	0.118	-	-
2925	$31/2^+ \rightarrow 27/2^+$	448.00(10)	4.48(18)	E2	-	-	-	-
3396	$35/2^+ \rightarrow 35/2^+$	239.60(10)	10.0(10)	M1	-	-	-	-
3396	$35/2^+ \rightarrow 31/2^+$	471.10(10)	6.39(23)	E2	1.241	0.196	0.043	0.004
3949	$39/2^+ \rightarrow 39/2^+$	277.00(10)	10.0(10)	M1	-	-	-	-
3949	$39/2^+ \rightarrow 35/2^+$	552.60(10)	4.95(19)	E2	-	-	-	-
4565	$43/2^+ \rightarrow 39/2^+$	615.90(10)	5.52(22)	E2	-	-	-	-
5220	$47/2^+ \rightarrow 43/2^+$	655.60(10)	3.60(15)	E2	-	-	-	-
5909	$51/2^+ \rightarrow 47/2^+$	689.10(10)	1.23(11)	E2	-	-	-	-
Band 2c								
2160	$23/2^- \rightarrow 21/2^-$	850.50(4)	10.6(4)	M1	-	-	-	
3106	$27/2^- \rightarrow 23/2^-$	946.00(7)	3.37(16)	E2	-	-	-	-
4055	$31/2^- \rightarrow 27/2^-$	949.30(10)	3.24(13)	E2	-	-	-	-
Gamma rays Feeding Intrinsic states								
2060	$25/2^- \rightarrow 25/2^+$	287.40(10)	0.89(14)	E1			-	-
2060	$25/2^- \rightarrow 21/2^-$	750.60(10)	10.0(10)	E2			-	-
2523	$29/2^- \rightarrow 25/2^-$	462.80(10)	10.0(10)	E2	1.089	0.256	-	-
1431	$23/2^- \rightarrow 19/2^-$	486.78(4)	6.8(3)	E2	-	-	-	-
1981	$27/2^- \rightarrow 23/2^-$	550.65(5)	4.60(20)	E2	-	-	-	-
1773	$25/2^+ \rightarrow 19/2^-$	764.80(10)	3.4(3)	E3	-	-	-	-
1522	$21/2^- \rightarrow 17/2^-$	706.53(5)	14.2(6)	E2	-	-	-	-
1122	$19/2^+ \rightarrow 15/2^+$	333.80(10)	7.6(3)	E2	-	-	-	-
2522	$27/2^+ \rightarrow 27/2^+$	214.60(10)	10.0(10)	M1	-	-	-	-
2053	$25/2^+ \rightarrow 21/2^+$	490.50(10)	4.19(22)	E2	0.818	0.182	-	-
2467	$29/2^+ \rightarrow 25/2^+$	414.20(10)	10.0(10)	E2	0.999	0.354	-	-
3023	$33/2^+ \rightarrow 29/2^+$	555.40(10)	10.0(10)	E2	-	-	-	-
1970	$21/2^- \rightarrow 19/2^-$	962.57(5)	8.0(3)	M1	-	-	-	-
2616	$25/2^- \rightarrow 21/2^-$	645.20(5)	5.9(3)	E2	-	-	-	-
2520	$27/2^- \rightarrow 25/2^-$	647.30(10)	10.0(10)	M1	-	-	-	-
2108	$29/2^- \rightarrow 25/2^-$	234.990(3)	18.7(6)	E2	-	-	-	-

The terms used in Table B.2 are explained as follows:

- $E_\gamma(I \to I-1)$ represents a gamma-ray that carries away one unit of angular momentum, and in this case a M1 transition
- $E_\gamma(I \to I-2)$represents a gamma-ray that carries away two units of angular momentum, and in this case an E2 transition
- λ refers to the experimental branching ratio obtained for this work
- $\pm Error$ is the error in λ
- $B(M1)/B(E2)$ is the ratio of the reduced transition probabilities for the respective transition

Table B.2: List of branching ratios (λ) and experimental B(M1)/B(E2) values

I^π	$E_\gamma(I \to I-1)$	$E_\gamma(I \to I-2)$	λ	$\pm Error$	$[B(M1)/B(E2)](\frac{\mu_n^2}{e^2b^2})$	$\pm Error$
			$[523]7/2^-$			
$11/2^-$	105.5	176.3	0.093	0.005	1.08	0.057
$13/2^-$	162.7	268.3	0.34	0.015	0.657	0.029
$15/2^-$	159.9	322.6	0.926	0.04	0.64	0.028
$17/2^-$	238.1	398.2	0.847	0.037	0.606	0.026
$19/2^-$	192.8	431.2	2.205	0.095	0.654	0.028
$21/2^-$	301.7	494.7	1.338	0.058	0.558	0.024
$23/2^-$	215.2	517.1	3.997	0.173	0.643	0.028
$25/2^-$	215.2	517.1	3.997	0.173	0.643	0.028
$27/2^-$	240.3	583.7	8.743	0.419	0.387	0.019
$29/2^-$	372.1	607.2	2.639	0.115	0.421	0.018
$31/2^-$	255.4	627.9	4.319	0.201	0.94	0.044
$33/2^-$	314.5	570.3	1.827	0.081	0.736	0.033
$35/2^-$	204.5	517.1	-	-	-	-
$37/2^-$	221.6	426	0.726	0.033	1.232	0.056
$39/2^-$	263.3	484.7	0.749	0.035	1.356	0.063
$41/2^-$	273.1	536.4	0.96	0.045	1.574	0.074
$43/2^-$	318.5	591.6	1.183	0.059	1.314	0.065
$45/2^-$	325	642.9	0.722	0.036	3.071	0.155
$47/2^-$	362	686.8	1.107	0.08	2.015	0.145

$49/2^-$	376.5	738.9	1.866	0.13	1.533	0.106
$51/2^-$	395	771.5	0.361	0.028	8.51	0.66
$53/2^-$	428.8	822.2	0.536	0.05	-	-
Band3 $[404]7/2^+$						
$11/2^+$	186.2	347.8	1.634	0.093	0.334	0.019
$13/2^+$	209	395.7	2.672	0.123	0.276	0.013
$15/2^+$	230.9	440.7	3.596	0.161	0.26	0.012
$17/2^+$	248.1	479.7	4.785	0.217	0.241	0.011
$19/2^+$	268.3	516.5	5.474	0.254	0.241	0.011
$21/2^+$	276.9	545.3	5.464	0.254	0.288	0.013
$23/2^+$	294.9	571.7	8.077	0.39	0.204	0.01
$25/2^+$	295.6	590.5	10.566	0.665	0.182	0.011
$27/2^+$	305.4	601.5	-	-	-	-
$29/2^+$	308.4	613.8	5.216	0.32	0.39	0.024
$31/2^+$	263	571.4	1.773	1.773	1.309	0.181
$33/2^+$	221.9	484.8	0.973	0.063	1.747	0.113
$35/2^+$	240.5	462.4	1.664	0.103	0.633	0.039
$37/2^+$	270.2	510.8	5.062	0.342	0.241	0.016
$39/2^+$	287.6	557.8	2.571	0.241	0.612	0.057
$41/2^+$	263	571.4	-	-	1.309	0.181
$43/2^+$	335.4	653.9	2.051	0.156	1.071	0.081
Band 1a and 2a						
$41/2^-$	320.1	606.6	1.273	0.072	1.363	0.077
$39/2^-$	286.5	627.5	2.714	0.178	1.056	0.069
$43/2^-$	311.1	631.2	2.123	0.123	1.086	0.063
Band 2b and 3a						
$27/2^+$	214.6	645.4	0.703	0.076	11.177	1.205
$31/2^+$	207.3	448.0	0.448	0.048	3.132	0.337
$31/2^+$	207.3	403.0	0.340	0.037	2.434	0.264
$35/2^+$	239.6	471.1	0.639	0.068	1.830	0.194
$39/2^+$	277.0	552.6	0.495	0.053	3.396	0.363

Bibliography

[1] J. F. Sharpey-Schafer *et al.*, Nucl. Phys. News. **14**, 5, (2004)

[2] A. G. Smith *et al.*, Nuclear Phys. A **587**, 150-180, (1995)

[3] Å. Bohr, B.R. Mottleson *Nuclear structure Vol II*, Singapore: World Scientific pp363, (1998)

[4] J. F. Sharpey-Schafer *et al.*, Eur. Phys. J. A **47**, 5, (2011)

[5] J. F. Sharpey-Schafer *in Proc. First Int. African Symp. On Exotic Nuclei* IASEN, (2013)

[6] P. E. Garret *et al.*, J. Phys. **G27**, R1, (2001)

[7] M. A. Riley, S.J. Gate *et al.*, Phys Lett B. **327**, 187-194, (1994)

[8] E. S. Paul *et al.*, Phys. Rev. Lett.,**98**, 012501, (2007)

[9] R. D. Evans *The Atomic Nucleus*, Mcgraw Hill Inc T.H. Edition, (1995)

[10] Å. Bohr *Nobel Prize lecture* https://www.nobelprize.org, (1975)

[11] A. Bickley, *Chapter 5-6: Strong force and nuclear structure University of Colorado* http://slideplayer.com/slide/9367144/

[12] R. F. Casten *Nuclear Structure From A Simple Perspective* , Oxford University Press Inc, (1990)

[13] S. G. Nilsson Mat. Fys. Medd. Dan. Vid. Selsk. **29** no 16, (1995)

[14] P. A. Pipidis PhD Thesis The Florida State University College of Arts and Sciences, (2006)

[15] L. I. Rusinov *et al.*, Usp. Fiz. Nauk **73**, 615(1961) and Soviet Phys.**4**, 282, (1961)

[16] E. Lawrie *Introduction to Nuclear Physics notes*, (2015) (unpublished)

[17] J. F. Sharpey-Schafer *Introduction to Nuclear Physics Lecture notes*, (2011) (unpublished)

[18] J. D. Garret *Shape and Pair Correlations in Rotating Nuclei* Proceedings of the second course of the International School of Heavy Ion Physics, (1986)

[19] http://lise.nscl.msu.edu/pace4.html

[20] C. H. Popenoe *et al.*, Nat. Bur. Stand. (U.S.), Tech. Note **790** 49, (1973)

[21] D. Radford *et al.*, NIM A361, 297 (1995)

[22] T. Szcus *et al.*, Eur.Phys.J **A44**, arXiv:1003.6072, 513-519, (2010)

[23] P. Regan *Post Graduate Nuclear Experimental Techniques (4NET) Course Notes*, (2003)

[24] R. Bengston and S. Frauendorf *et al.*, Nuclear Phys.A **327**, 139, (1979)

[25] *2RD Radiation Detection and Measurement –Section 4 figures* http://web.ph.surrey.ac.uk/2rdm/section2figures.pdf

[26] http://www.toequest.com/forum/physics-articles/7164-compton-scattering.html

[27] http://physics.tutorcircle.com/modern-physics/compton-scattering.html

[28] D. Leadly University of Warwick, *Physics department notes, Electronic band structure* https://www.2.warwick.ac.uk/fac/sci/physics/current/postgraduate/regs/mpags/ex5/bandstructure (2010)

[29] http://www.gitam.edu/eresource/Engg-Phys/semester-2/semicon/int-ext.html

[30] M. Lipoglavsek *et al.*, Nuclear Phys.A **557**, 523-527, 5, (2004)

[31] A. H. Botha, H.N. Jungwirth *Proc- 10th Int-Conf and their Applications.* East Lansing, 263, (1984)

[32] J. L. Conradie, *Cyclotrons and Their Applications* Eighteenth International Conference, (2007)

[33] T. T. Hlatshwayo MSc thesis University of Zululand, (2005)

[34] J. H. Lee, J.*et al.*, Kor. Phys. Soc.**40**, 793, (2002)

[35] F. Cappellaro *Studies of excited nuclear states* Uppsala University, (2005)

[36] C. Teal Jr, PhD thesis, The Florida State University, (2009)

[37] C. Foin *et al.*, Nuclear Phys.A **417**, 511 -533, (1984)

[38] I. Adam *et al.*, Nuclear Phys.A **356**, 129-145, (2005)

[39] M. S. Maliage, MSc thesis, University of the Western Cape, (2006)

[40] J. P. Davidson *Collective Models of The Nucleus* Pure and Applied Physics, Academic Press Inc, Volume 29, (1968)

[41] S. Frauendorf *et al.*, Phys. Lett., **100b**, 219, (1981)

[42] D. C. Radford *et al.*, Nucl.Phys.A **545**, 665, (1992)

[43] ftp://radware.phy.ornl.gov/pub/nd/161/161Tm_ensdf_A.ags

[44] H. Carlsson*et al.*, Nucl.Phys. A **551**, 295, (1993)

[45] H. J. Jensen*et al.*, Z.Phys. A **340**, 351, (1991)

[46] J. M. Rees *et al.*, Phys. Rev.C **83**, 044314, (2011)

[47] C. H. Yu *et al.*, Nuclear Physics A. **489**, 477-507, (1988)

[48] W. Schmitz *et al.*, Nuclear Physics A. **539**, 112-136, (1992)

[49] G. SchonwaBer *et al.*, Nuclear Physics A. **735** , 393-424, (2004)

[50] H. J. Jensen *et al.*, Z. Phys.A Hadrons and Nuclei **340**, 351-362, (1991)

[51] H. J. Jensen *et al.*, Nuclear Physics A. **695**, 3-50, (2001)

[52] A. Bohr and B. R. Mottelson. *Nuclear Structure, volume II.*, Benjamin, New York, **2.4.3, 2.4.6, 3.7.4, 3.7.4**, (1975)

[53] L. L. Riedinger *et al.*, Physical Review Letters44(9): 568–571, **3.7.10, 3.21, 3.2, 4.5, 4.9, 4.10, 4.11, 4.12, 5.6, 5.29, 5.6, 5.1, 5.6, 5.30**, (1980)

[54] G. Gervais, D. C. Radford *et al.*, Nucl.Phys.A **264**, 257, (1997)